PolyPublie
Polytechnique Montréal

POLYTECHNIQUE MONTRÉAL
UNIVERSITÉ D'INGÉNIERIE

Titre: Title:	Novel Method for Attenuation of Inlet Distorsion Effects on Turbofan Engines for Future Commercial Aircraft
Auteur: Author:	Lina Liu
Date:	2021
Type:	Mémoire ou thèse / Dissertation or Thesis
Référence: Citation:	Liu, L. (2021). Novel Method for Attenuation of Inlet Distorsion Effects on Turbofan Engines for Future Commercial Aircraft [Ph.D. thesis, Polytechnique Montréal]. PolyPublie. https://publications.polymtl.ca/9997/

Document en libre accès dans PolyPublie
Open Access document in PolyPublie

URL de PolyPublie: PolyPublie URL:	https://publications.polymtl.ca/9997/
Directeurs de recherche: Advisors:	Huu Duc Vo
Programme: Program:	PhD.

Ce fichier a été téléchargé à partir de PolyPublie, le dépôt institutionnel de Polytechnique Montréal
This file has been downloaded from PolyPublie, the institutional repository of Polytechnique Montréal

https://publications.polymtl.ca

POLYTECHNIQUE MONTRÉAL

affiliée à l'Université de Montréal

Novel method for attenuation of inlet distortion effects on turbofan engines for future commercial aircraft

LINA LIU

Département de génie mécanique

Thèse présentée en vue de l'obtention du diplôme de *Philosophiæ Doctor*

Génie mécanique

Décembre 2021

© Lina Liu, 2021.

POLYTECHNIQUE MONTRÉAL

affiliée à l'Université de Montréal

Cette thèse intitulée:

Novel method for attenuation of inlet distortion effects on turbofan engines for future commercial aircraft

présentée par **Lina LIU**

en vue de l'obtention du diplôme de *Philosophiæ Doctor*

a été dûment acceptée par le jury d'examen constitué de :

Marcelo REGGIO, président
Huu Duc VO, membre et directeur de recherche
Njuki W. MUREITHI, membre
William D.E. ALLAN, membre externe

ACKNOWLEDGEMENTS

I would like to express my appreciation to those who made it possible for me to carry out this work at Polytechnique Montréal. Without their support and contributions, this work cannot be completed.

First I would like to thank all members of my thesis committee for their time and effort in reading and evaluating my work. I am also grateful for the financial support and theoretical guidance of my supervisor Dr. Huu Duc Vo. His expertise in the field of turbomachinery, dedication to each of his students, and his passion for exploring novel subjects has deeply influenced me.

In addition, I would like to thank Mr. Toni Chakour for his guidance and help with learning ANSYS CFX when I first started this project. I would also like to thank Mr. Louis Duranleau-Hendrickx for his support in the 3D geometry generation of inlet guide vanes. I am very thankful to Mr. Antoine Poirier-Boulet and Mr. Roberto Ojeil for their help in carrying out experiments on the low-speed fan test rig.

Moreover, the other people in Dr. Vo's research group, namely Marc Belleau, Xin Gu, Javad Hosseini, Farzad Ashrafi, Mahsa Ebrahimi, Mohsen Boroumand, have been an important part of my experience at Polytechnique Montréal. Their friendship and mutual support have fortified me and I will forever be thankful.

I am also thankful for the computational resources provided by Compute Canada and Calcul Québec along with the technical support from Mr. Richard Lefebvre and Mr. Daniel Stubbs, which made the completion of this project possible.

Finally, I thank my parents and grandparents, for their continued encouragement and financial support during my doctoral studies, especially, my grandfather who has given me the tremendous love and everything. Wishing you peace in heaven.

.

RÉSUMÉ

La mise en œuvre du concept d'avion à ingestion de couche limite pour une réduction significative de la consommation de carburant et du bruit dépend de l'atténuation de l'impact négatif de la distorsion aérodynamique (flux entrant non-uniforme) sur l'intégrité structurelle et la performance des turbosoufflantes. Cette recherche propose et analyse un nouveau concept pour résoudre ces problèmes en plaçant un dispositif juste en amont du rotor de la soufflante pour diminuer la fluctuation de la force aérodynamique qui peut briser les pales de la soufflante, ainsi qu'atténuer la non-uniformité de l'écoulement à la sortie du rotor qui affecte la performance aérodynamique de la soufflante et par extension, du moteur d'avion. L'objectif de ce projet est de faire une première évaluation de l'efficacité de ce dispositif d'atténuation sur des soufflantes à basse et à haute vitesse.

Une étude numérique est réalisée sur trois géométries de soufflante: un rotor de soufflante à basse vitesse, un rotor de soufflante à haute vitesse (transsonique) plus réaliste (NASA Rotor 67) et un étage de soufflante à basse vitesse provenant d'un banc d'essai de distorsion à Polytechnique Montréal (pour une éventuelle validation du concept). Les simulations CFD 3D instationnaires de la soufflante (sur 360º) sont effectuées avec ANSYS CFX, en mode non-visqueux sans jeu d'aube (à l'exception de la dernière géométrie, car elle est destinée à être testée sur un banc d'essai) pour garder les ressources et le temps de calcul raisonnables. Le dispositif d'atténuation est conçu manuellement et des simulations CFD sont faites afin d'évaluer sa performance.

Pour les deux premières géométries de soufflante (basse vitesse et haute vitesse), la redistribution locale de l'écoulement d'entrée aux bords de la région de distorsion résulte à une variation circonférentielle continue de la force aérodynamique des pales de rotor. Dans les deux cas, la conception du dispositif d'atténuation, bien que non optimisée, a réduit l'amplitude de variation de la force aérodynamique d'environ deux tiers. Le dispositif d'atténuation permet également de récupérer la moitié ou plus de la perte d'augmentation de pression due à la distorsion aérodynamique. Il a également pu réduire la non-uniformité de pression totale à la sortie du rotor pour la soufflante à grande vitesse, mais n'a pas réussi à le faire pour la soufflante à basse vitesse. Cependant, une analyse plus détaillée indique que l'efficacité du dispositif d'atténuation peut être améliorée sur les trois métriques par une meilleure optimisation de son design.

Dans le cas de l'étage de soufflante du banc d'essai, la redistribution locale l'écoulement d'entrée aux bords de la zone de distorsion est réduite par la position de l'écran de distorsion et la présence d'une rangée d'aubes directrices d'entrée axiales dans le banc d'essai, entraînant des changements brusques (distribution non uniforme) dans la force aérodynamique des pales de rotor près des bords de la région de distorsion. Ces changements brusques de force aérodynamique rendent le dispositif d'atténuation difficile à concevoir et inefficace. Cependant, cette situation n'est pas représentative des vraies soufflantes et ces résultats suggèrent que la validation expérimentale du dispositif d'atténuation devrait se faire sur un banc d'essai de soufflante avec une configuration plus réaliste.

ABSTRACT

The implementation of the concept of boundary layer ingestion aircraft for significant reduction in fuel consumption and noise is dependent on mitigating the negative impact of inlet distortion (non-uniform inflow) on the structural integrity and performance of turbofan engines. This research proposes and analyzes a novel concept to solve these problems in the form of a device placed just upstream of the fan to decrease the fluctuation in aerodynamic force on the fan blades under large inlet distortion that can lead to blade failure, as well as to attenuate the flow non-uniformity at the fan rotor that affect fan/engine aerodynamic performance. The objective of this project is to provide a first assessment of the effectiveness of this device on low and high-speed fans.

A computational study is carried out on three fan geometries: a low-speed fan rotor, a more realistic high-speed (transonic) fan rotor (NASA Rotor 67) and a low-speed test fan stage from a distortion test rig at Polytechnique Montréal (for possible validation of the concept). Full-annulus unsteady, 3D CFD simulations are carried out in ANSYS CFX, in inviscid mode without tip clearance (except for the last geometry since it was intended to be rig tested) to keep computational resources and time reasonable. The attenuation device is designed manually and CFD simulations are carried out to evaluate its performance.

For the low-speed and high-speed fan rotors, local flow redistribution at the edges of the distortion region leads to relatively smooth circumferential variation of rotor blade aerodynamic force. In both cases, the attenuation device design, though not optimized, reduces the aerodynamic force variation amplitude by around two-thirds. The attenuation device design also recovers half or more of the loss in pressure rise due to inlet distortion. It is also able to reduce the total pressure distortion at the fan rotor exit for the high-speed fan but is unsuccessful for the low-speed fan. However, a more detailed analysis indicates that the effectiveness of the attenuation device can be improved in all three metrics if a more optimized design is performed.

In the case of the test fan stage, the local flow redistribution at the edges of the distortion region is reduced due to the location of the distortion screen and the presence of the straight inlet guide vanes in the test rig, leading to sudden changes (non-smooth distribution) in rotor blade aerodynamic force near the edges of the distortion region. The local jump in aerodynamic force makes the attenuation device difficult to design and ineffective. However, this situation is not

representative of real fans and these results suggest that experimental validation of the attenuation device should be done on a more realistic fan distortion test rig.

TABLE OF CONTENTS

LIST OF TABLES

LIST OF FIGURES

LIST OF SYMBOLS AND ABBREVIATIONS

Symbols	Description
A	area
DC	distortion parameter based on the degree sector
$\dot{m}$	mass flow rate
P	pressure
R, r	radius
V	velocity magnitude
$\mathbf{V}$	velocity vector
U	wheel speed (Ωr)
x, y, z	Cartesian coordinate axes
u, v, w	Cartesian coordinate axes
α	absolute swirl angle
β	gas angle into blade
ρ	density
Ω	rotor angular velocity

Subscripts	
hub	blade hub
in	Domain inlet
mid	blade midspan
ref	reference value
s	static
tip	blade tip
t	total

Abbreviations	
BLI	boundary layer ingestion
CPU	central processing unit

IGV	inlet guide vane
NACA	National Advisory Committee for Aeronautics
LE	leading edge
RANS	Reynolds-Averaged Navier-Stokes
RAM	random access memory
SAI	Silent Aircraft Initiative
TE	trailing edge
UTRC	United Technologies Research Center

LIST OF APPENDICES

CHAPTER 1 INTRODUCTION

1.1 Background

Airline operations produced 705 million metric tons of CO_2 in 2013, an amount that increases at an annual rate of 4.5% with the vigorous development of the air transport industry [1, 2], contributing to global warming. In addition, fuel account for about 35% of airline operating costs. Therefore, increasing fuel efficiency has become a long-term strategy for airlines to both meet environmental requirements and to improve their economic performance.

One of the most promising future aircraft concepts for further decrease in fuel consumption is the boundary layer ingestion (BLI) aircraft, illustrated in Figure 1.1. Current aircraft engines are located away from the aircraft's fuselage to avoid ingesting the highly non-uniform and slower boundary layer flow. The wake formed by the merging of these boundary layers downstream of the aircraft is the source of drag, which must be compensated by the thrust of the aero-engines. As illustrated by the upper illustration of Figure 1.1, this thrust is currently generated by accelerating the flow entering at aircraft flight velocity to higher velocities at the engine exit. In contrast, the concept of boundary layer ingestion (BLI) involves embedding the engines in the aircraft body at the back of the fuselage to ingest the low-momentum boundary layer fluid and accelerate it to approximately aircraft velocity to effectively cancel the fuselage wake to eliminate drag, as depicted in the lower illustration of Figure 1.1. Since it takes less power from the engines to accelerate the flow from a low (boundary layer) velocity to aircraft velocity (BLI configuration) than from aircraft velocity to higher velocity (conventional configuration), the fuel consumption is reduced, as shown by several studies [3-8].

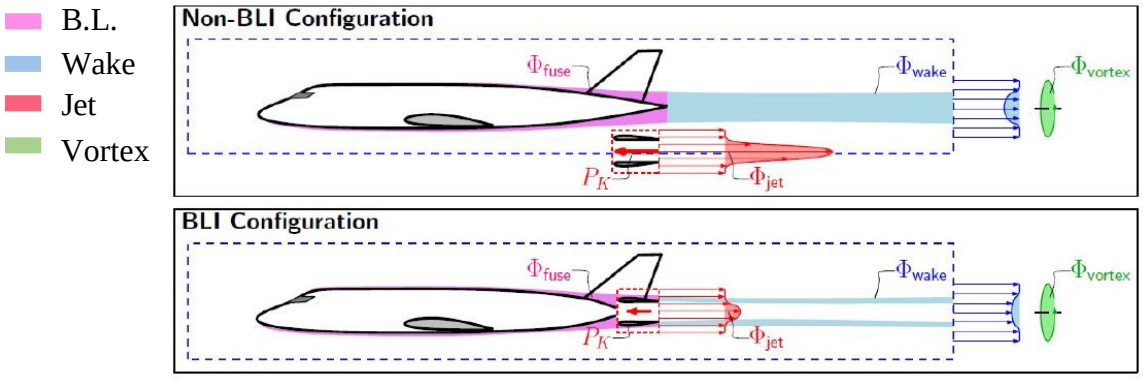

Figure 1.1 Conventional propulsion (top) versus BLI propulsion (bottom) [7]

A few aircraft designs involving the BLI concept have been proposed and studied. One of the first is the hybrid wing aircraft for low noise and high fuel efficiency designed under the Silent Aircraft Initiative (SAI) [9-11], as illustrated in Figure 1.2. This research looked into different engine integration configurations, as illustrated in Figure 1.3, namely the podded engines (additional support structure required), the embedded engines with boundary layer diversion (boundary layer not ingested) and the BLI engines. Depending on the number of engines (4 and 16), the initial study [9] showed that the BLI propulsion for this aircraft configuration can decrease fuel consumption by 11%, thrust requirement by 20%, and noise by 13 dB, compared to a conventional propulsion configuration.

Figure 1.2 A concept of hybrid wing aircraft [11]

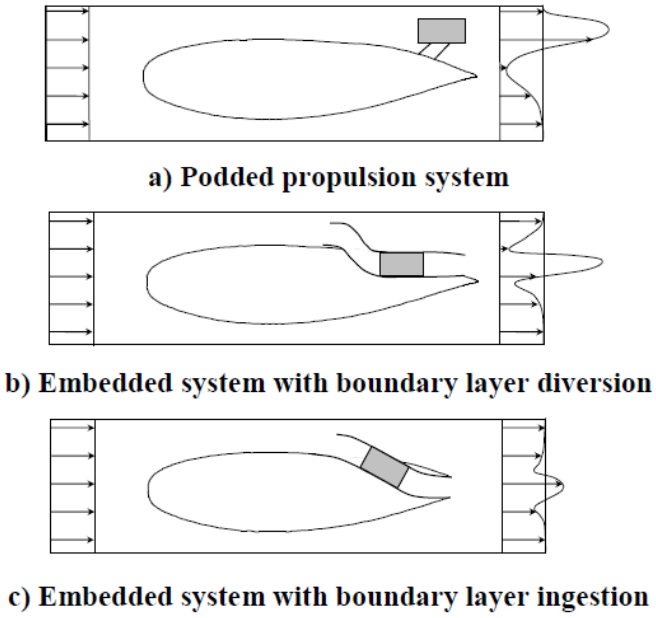

Figure 1.3 Options for power plant integration [9]

Other proposed BLI aircraft designs include the proposed generation-after-next aircraft studied by United Technologies Research Center (UTRC) and NASA Glenn Research Center [12] (Figure 1.4) which is claimed to have a fuel burn benefit of about 3-5%, a baseline high-performance, pylon-mounted, Ultra-High-Bypass propulsion system, and the NASA-sponsored D8 transport aircraft concept [13], with a wind tunnel test model shown in Figure 1.5, for which the BLI propulsors would require 6% less electrical power at cruise than a standard configuration needs.

BLI aircraft have the following advantages:

- Lower power requirement leading to lower fuel consumption, greenhouse gas emissions and weight
- Reduced incidence of bird strikes due to rear engine placement
- Integrated configuration with less structural requirement than a podded engine configuration, reducing weight and, by extension, fuel consumption [14].

Figure 1.4 Generation-after-next aircraft [12]

Figure 1.5 D8 transport aircraft concept [13]

1.2 Problem

The concept of BLI aircraft dates back to 1946, when Smith [15] presented the concept of using the boundary layer in aircraft propulsion. However, one of the key reasons it has not yet been implemented in civil aircraft is the effect of BLI on the turbofan engine. As illustrated in Figure 1.6, the ingestion of the boundary layer results in flow non-uniformity at the engine face, as shown by the contours of total (stagnation) pressure at the engine face, where the boundary layer fluid leads to a region of low total pressure and low axial flow velocity and higher axial velocity elsewhere due to the flow redistribution for the same mass flow. The shape and total pressure deficiency of the distorted flow region depends on the upstream airframe contour as well as inlet duct offset/length, wall curvature/shape, aspect ratio, lip contour and thickness [16]. This non-uniformity in inlet flow leads to a drop in fan aerodynamic performance and in fan stall margin. Indeed, much of the fan would operate outside of the optimum (peak efficiency) inlet axial velocity resulting in lower pressure ratio and efficiency (*i.e.* higher engine fuel consumption), with the distorted region operating closer to stall (higher tendency for fan to stall) and the undistorted region closer to choke. Moreover, the fan blades experience an undesirable aerodynamic force variation. The source of this variation is explained in Figure 1.7, which shows a comparison of velocity triangles at the inlet of the fan rotor between the undistorted and distorted flow regions, where *Vx, U* and *W* represent the rotor inlet axial velocity component, circumferential blade velocity and relative velocity, respectively. One can see that in the distorted region, the low axial/meridional velocity leads to higher flow incidence and thus blade force

relative to nominal case. Moreover, the presence of inlet distortion leads to a flow redistribution upstream of the fan, which increases the axial velocity (decrease in incidence) on the undistorted flow region, reducing the blade force. Therefore, each fan rotor blade experiences a variation in force as it rotates around the circumference.

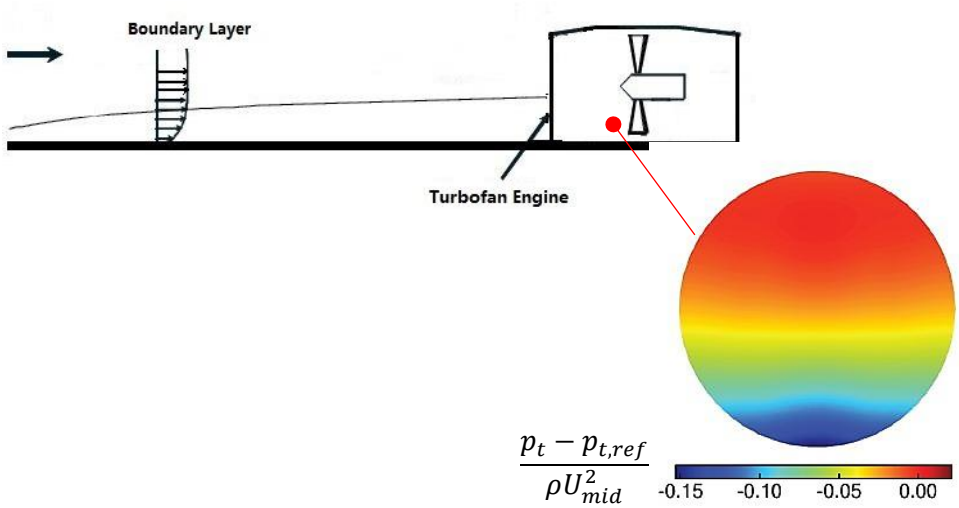

Figure 1.6 Inlet distortion associated with BLI [17]

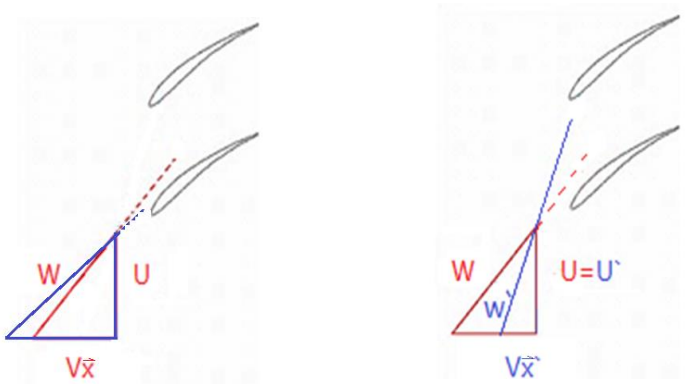

(a) Undistorted region (b) Distorted region

Figure 1.7 Fan rotor inlet velocity triangle in (a) undistorted region and (b) distorted region

Current turbofan engines are designed for uniform inlet flow and cannot perform adequately aerodynamically nor survive structurally the level of inlet distortion associated with BLI applications. While research has been carried on simulating and characterizing turbofan engines performance for BLI [18, 19], few solutions have yet been proposed to solve the inlet distortion problem on turbofan engines to implement BLI on real aircraft. One approach consists of using vortex generators and air jets placed in the inlet duct to moderately reduce the inlet distortion amplitude by inducing flow mixing between the low and high momentum regions [20]. However,

high-pressure air extraction from the engine for the air jets will incur performance penalty and the presence of many recirculation pipes and injection ports will increase manufacturing and maintenance costs. The other approach is to enhance the structural strength of the fan [21, 22], which usually involves an aerodynamic performance trade-off (since fan blades become thicker) and does not necessarily address the aerodynamic performance penalty associated with inlet distortion.

1.3 New Concept of Non-axisymmetric Inlet Guide Vanes

The current research proposes a novel approach for attenuation of inlet distortion effects on turbofan engines for BLI aircraft. This approach consists of inducing a spatially varying swirl distribution just upstream of the fan to reduce flow incidence angle in the distorted flow region and increase it in the undistorted flow region to attenuate the effects of the inlet distortion on both the force fluctuation of the fan blade as well as the fan aerodynamic performance. The approach is implemented passively by placing a row of asymmetric (non-axisymmetric) IGVs just upstream of the fan rotor to locally change the local velocity triangle, as illustrated in Figure 1.8.

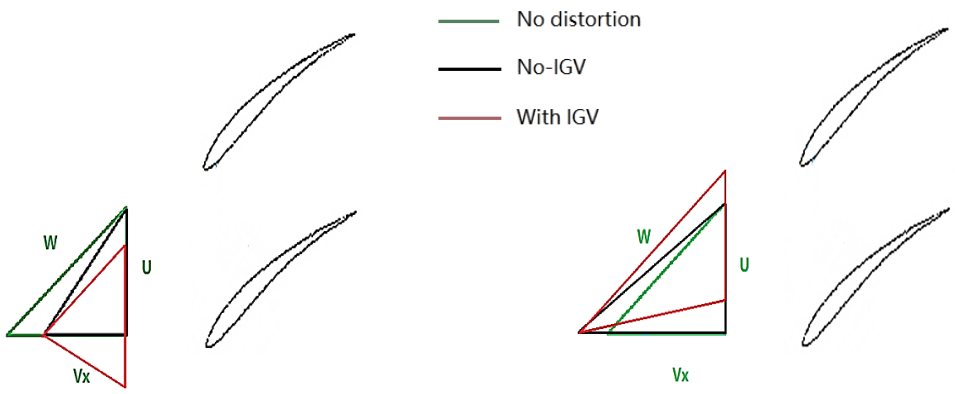

Figure 1.8 New asymmetric IGV concept

In the distorted flow region where fan blade loading (aerodynamic force) is high, the IGVs would induce swirl in the direction of rotation to reduce incidence angle and fan blade loading (Figure 1.8a). Conversely, the IGVs would induce swirl in the opposite direction in the undistorted region to increase incidence angle (or rather annul the drop in incidence angle due to flow redistribution)

and blade loading. As such, one can, in principle, use the asymmetric IGVs to tailor the local incidence angle to remove any blade force variation. The proposed concept can take advantage of additive manufacturing technology to create an IGV blade row with spatially irregular blades, tailored to an inlet distortion pattern of any complexity.

1.4 Objectives

The main objective of this research is provide a preliminary assessment on effectiveness of the asymmetric inlet guide vanes concept for attenuation of inlet distortion effects on low and high-speed fans. The specific objectives are:

- Assessment the effectiveness of the asymmetric inlet guide vanes concept in attenuation of inlet distortion effects on fan rotor blade force variation;
- Assessment the effectiveness of the asymmetric inlet guide vanes concept in attenuation of inlet distortion amplitude at the fan rotor exit; and,
- Assessment the effectiveness of the asymmetric inlet guide vanes concept in attenuation of inlet distortion effect on fan performance.

1.5 Thesis Outline

Following the introduction in Chapter 1, Chapter 2 provides a literature review on the state-of-the-art in inlet distortion research, in terms of experimental measurements, modeling/simulations and attenuation strategies. Chapter 3 presents the methodology to achieve the proposed objectives, including three fan geometries for study. Chapter 4 presents the assessment results for asymmetric IGVs concept on a low-speed fan rotor. Chapter 5 shows the results for a more realistic transonic fan rotor. Chapter 6 presents the assessment for a low-speed fan stage in a distortion fan test rig. Finally, Chapter 7 summarizes the conclusions and provides recommendations for future work.

CHAPTER 2 LITERATURE REVIEW

2.1 Experimental Analysis of Inlet Distortion Effects

Experimental studies focusing on the engine performance with inlet distortion have been carried out for several decades, prior to any formal BLI research. In 1950, Conrad and Sobolewski [23] conducted an investigation in the NACA Lewis altitude wind tunnel to determine the effect of inlet distortion on the performance of a full-scale axial flow turbojet engine. As shown in Figure 2.1, two similar engines were tested with the main difference being in the intake duct on for in which different obstructions were placed to generate inlet flow velocity gradients in the radial and the circumferential directions. The hub-to-tip diameter ratio of the rotor stage was 0.65, the rotor inlet tip Mach number was 0.894 and the nominal flight Mach number was 0.21 with an equivalent test altitude of 30,000 ft (9153 meters). They found that the ratio of fuel consumption values varied by a maximum 4% and concluded that at low inlet Mach number, inlet distortion did not affect engine performance significantly. While this work proposed the use of screens to simulate inlet distortions, neither the distortion pattern nor the engine type were likely representative of BLI applications in turbofan engines.

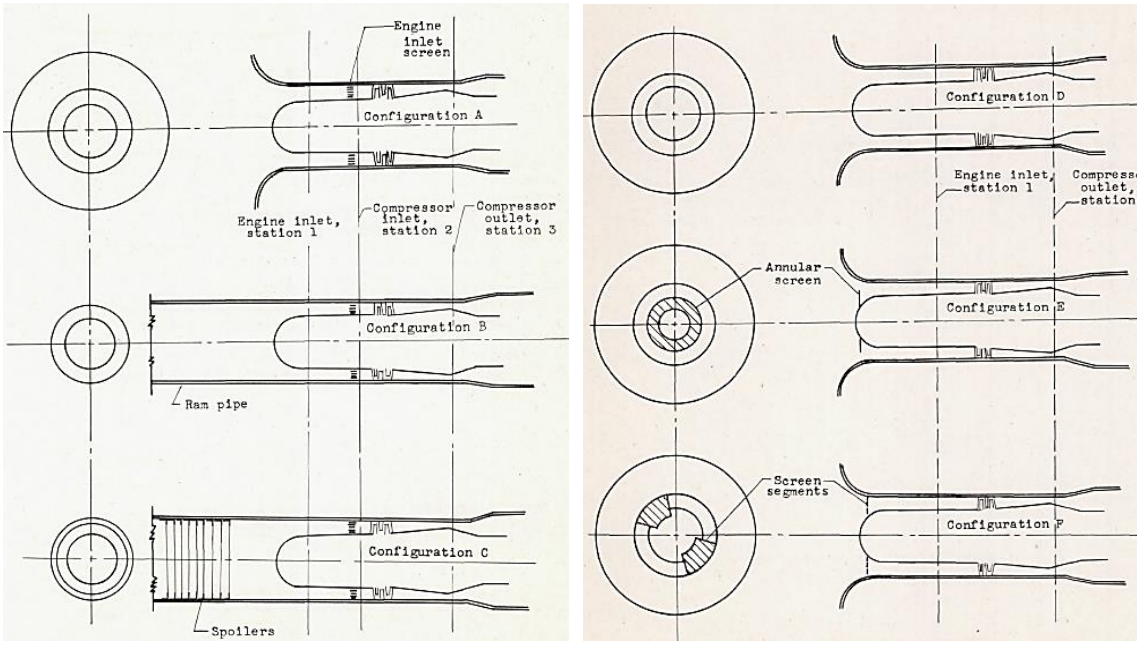

Figure 2.1 Inlet configurations for engine inlet distortion testing [23]

Subsequently, Conrad *et al.* [24] inserted multiple circumferential, radial and combined circumferential and radial distortion screens into the entrance of another axial turbojet engine (in Figure 2.2) to study, in more detail, the effect of non-uniform inlet flow on engine fuel consumption in transonic flow conditions. The setup was tested in the altitude test chamber at the equivalent altitude of 35,000 feet altitude (10,679 meters) and simulated flight Mach number at 0.8 for a range of distortion configurations formed by changing the various combinations of screens installed about one engine diameter upstream of the engine face. However, at the time, there was no general target distortion shape or pattern to simulate actual inlet distortion in aircraft or expectations based on model tests. The inlet pressure distribution was shown in Figure 2.3. The authors found that the distortion decreased compressor performance, caused by a lower value of peak pressure rise. Moreover, the presence of the distortion increased the maximum measured value of vibratory stress in the transonic first-stage compressor rotor blades by about 80% , which indicated that the structural consequences of inlet distortion on the blades were a serious problem.

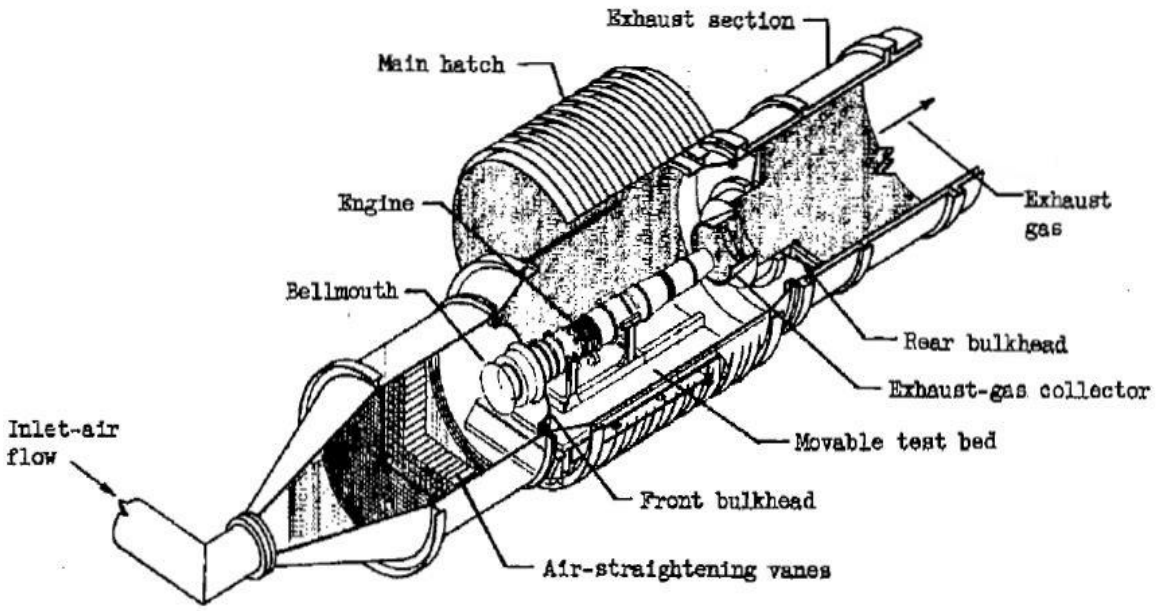

Figure 2.2 NACA Altitude chamber used by Conrad *et al.* [24]

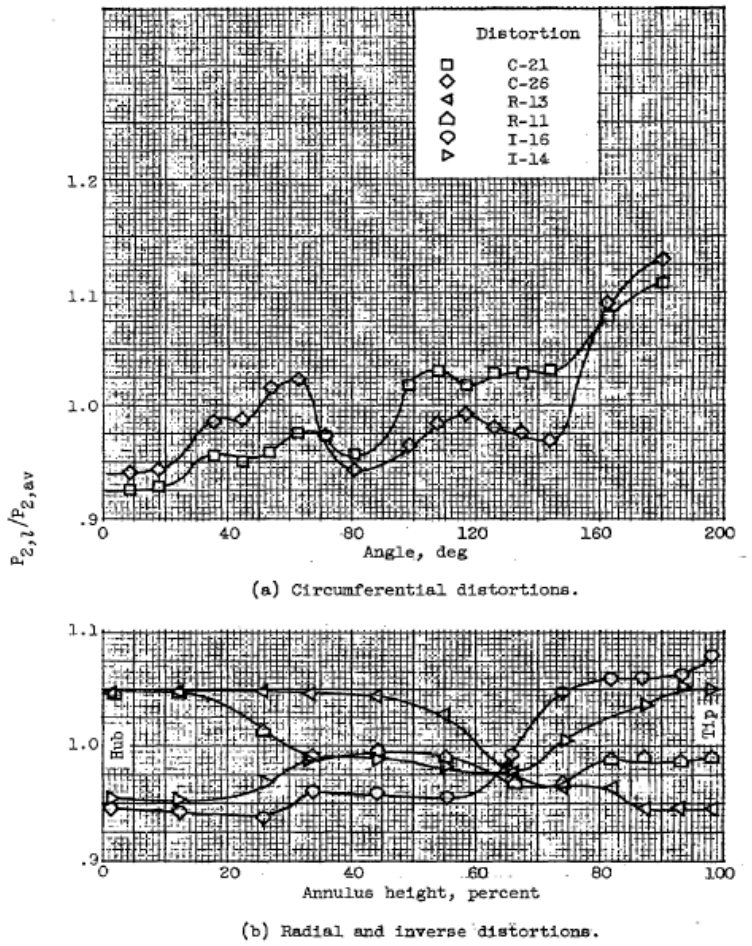

Figure 2.3 Pressure profiles at compressor inlet at 35,000 feet [24]

More recently, Atinault *et al*. [25] presented a clever way to experimentally investigate the effects of BLI on fans. The low-speed tests were carried out on a BLI test rig placed in the ONERA L1 wind tunnel in Lille (France) and tested at low flow velocity. As illustrated in Figure 2.4, the test setup consisted of placing a blunt body in the wind tunnel to generated a boundary layer that could then be ingested by a downstream propulsor (fan) whose power and thrust could be measured. The axial and vertical position of the propulsor relative to the blunt body could be changed in order to change the amplitude extent and symmetry of the distortion pattern. The collected test data were used to validate a CFD-based actuator disk approach to model inlet distortion, as will be described later in Section 2.2.

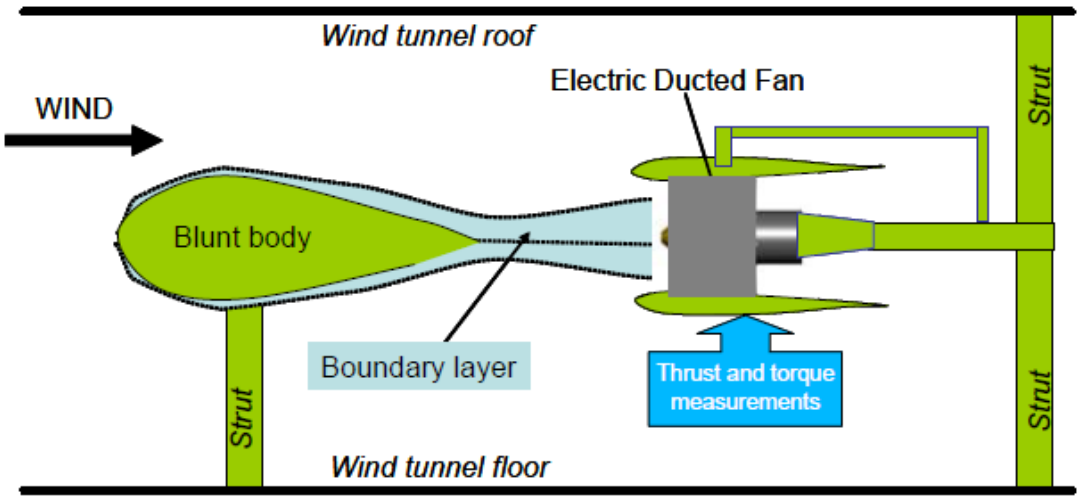

Figure 2.4 Sketch of principle of the RAPRO2 test set-up [25]

2.2 Simulation of Inlet Distortion Effects

As the capability of parallel computing and processor speed has increased steadily, computational fluid dynamics (CFD) simulations play an increasingly important role in studying flow physics in turbomachinery, such as blade row interactions, tip and hub clearance flows, hot streak migration in turbines, and end wall contouring. The standard CFD simulation setup up for turbomachinery consists of one blade passage per blade row with periodic boundary conditions imposed on the lateral surfaces based on an assumption passage-to-passage flow symmetry. Furthermore, these simulations are often carried out in steady mode with a mixing plane interface (circumferential averaging of flow parameters) between adjacent blade rows. This setup reduces the computational requirements to acceptable level. However, this passage-to-passage flow symmetry assumption breaks down in the presence of non-axisymmetric inlet distortion patterns associated with most applications, such as non-axial intake and BLI, for which full-annulus unsteady (time-accurate) simulations are required. Such simulations are known to be very expensive in terms of computational resources and time, even with current computational technology. Therefore, researchers have proposed different modeling approach to numerically study the effect of inlet distortions on compressors and fans.

The first and most rudimentary model is the Parallel Compressor Model by Pearson and Mckenzie [26]. As illustrated in Figure 2.5, it essentially consists of separating the compressor/fan under inlet distortion into separate sectors, each of which operates with uniform

inlet conditions. The sections have different inlet total pressure and/or temperature and their weighted sum will approximate the behavior of the entire compressor. In terms of stability, the model predicts stall to occur when the most distorted compressor section stalls. This model requires knowledge of the characteristics of the compressor with uniform inflow, *i.e.* pressure rise and efficiency versus mass flow, and is based on several assumptions, namely that there is no fluid migration through the compressor between the distorted and undistorted region. A uniform inlet static pressure is used to calculate the inlet local flow velocity and local compressor performance. Davis and Cousins [27] compared the pressure ratio of six different sets of inlet distortion obtained with the Parallel Compressor Model with test data. Their results indicated that the parallel model is suitable for total pressure distortion with neither radial pressure nor temperature distortion. However, for most inlet distortion patterns, including those from BLI configuration, the total pressure varies greatly in the radial direction, negating the usefulness of this model.

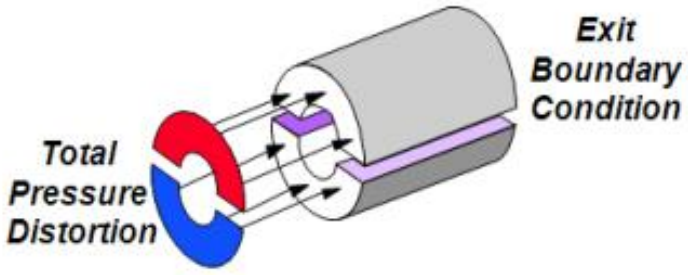

Figure 2.5 Parallel Compressor Model [24]

Another modelling approach is to consider the compressor as an annular actuator disk, *i.e.* a thin disk through which the pressure changes instantaneously. The local total pressure rise across the disk is calculated from the spanwise distribution of total pressure rise across the compressor at different mass flows obtained either through CFD or experiments. Atinault *et al*. [25] used Reynolds-Averaged Navier-Stokes (RANS) CFD to obtain this distribution for the actuator disk model of their fan and compared the performance of their model to test data for the test setup previously shown in Figure 2.4. Figure 2.6 plots the measured and predicted power imparted to the flow by the fan (power coefficient) versus net thrust coefficient (CT-CD) without and with BLI (inlet distortion). These results indicate that the model reproduces the experimentally

observed trend, namely that the reduction in power coefficient from BLI increases with net thrust. While the actuator disk model can accommodate both circumferential and radial distortion, like the parallel compressor model, it cannot capture the flow redistribution that occurs within the compressor between the distorted and undistorted regions. In addition, the actuator disk model relies excessively on detailed CFD or test data for each compressor geometry, which can be expensive in time and computational resources to obtain.

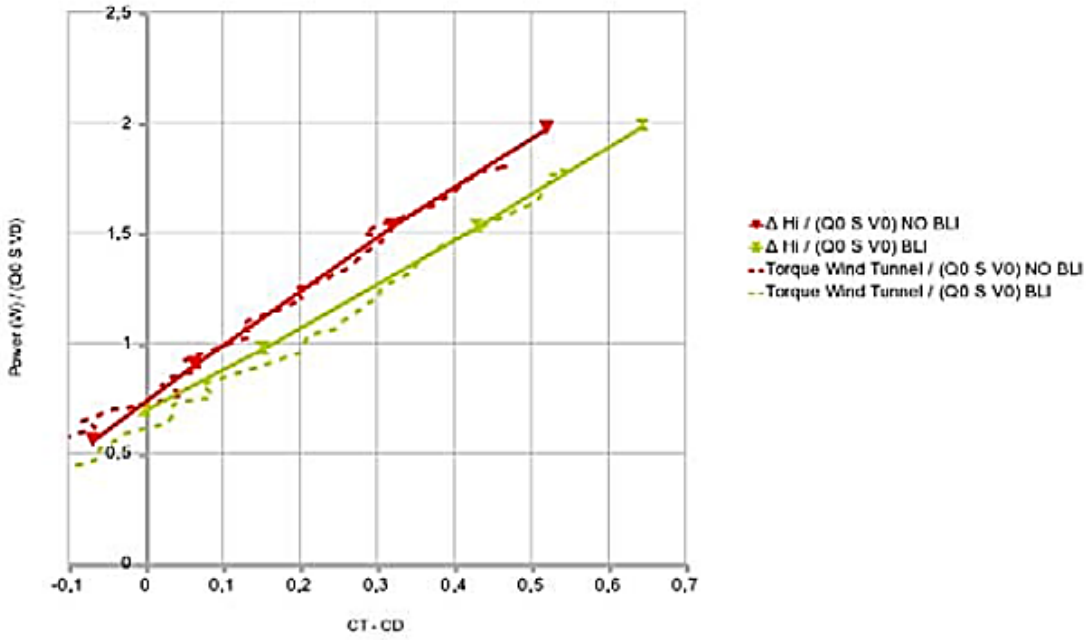

Figure 2.6 Effect of BLI on the Power coefficient as a function of the global axial force.

CFD and experimental raw data [25]

Using a different approach that can capture flow redistribution within the compressor, Gong *et al*. [29] presented a computational model to describe the response of multi-stage compressors to three-dimensional, non-linear flow perturbations, such as those associated with short wavelength rotating stall inception, part-span stall cells and inlet distortion. As illustrated in Figure 2.7, this model consists of replacing each blade row by axi-symmetrically distributed body forces that respond to local flow conditions to turn the flow in the same manner as the blades. The body forces are derived from (uniform inflow) integral compressor characteristics of each blade row with the assumption that these characteristics are constant along the span from hub to shroud. The body forces are placed as source terms in CFD simulations. Without discrete blades, the computational domain representing the gas path can use a simple, coarse, axisymmetric,

cylindrical, mesh with the body force terms placed over the nodes in the meridional region associated with the blade rows. The reduced computational cost of this setup allows for the full-annulus multi-stage compressor to be simulated with CFD with reasonable time and resources. Figure 2.8 presents the computed and measured axial flow coefficient profile in front of the first rotor for a low-speed three-stage axial compressor with inlet disturbance generated by screens places in the upstream duct. These results showed that Gong's computational model reproduced very well the circumferential flow redistribution near the compressor. However, the replacement of discrete blades with axi-symmetrically distributed body forces relies on the assumption of an infinite number of blades, which would be applicable if the characteristic circumferential length-scale of the non-uniformity were much larger than the blade pitch. Furthermore, the assumption of constant blade performance from hub-to-tip is only valid for blade rows with high hub-to-tip ratio. As such, this model may not be adequate for fans with low blade count and low hub-to-tip ratio (large flow property variations along the span). Finally, while the characteristics of the entire full-stage compressor may be easily obtained, those of individual blade rows are usually not readily available.

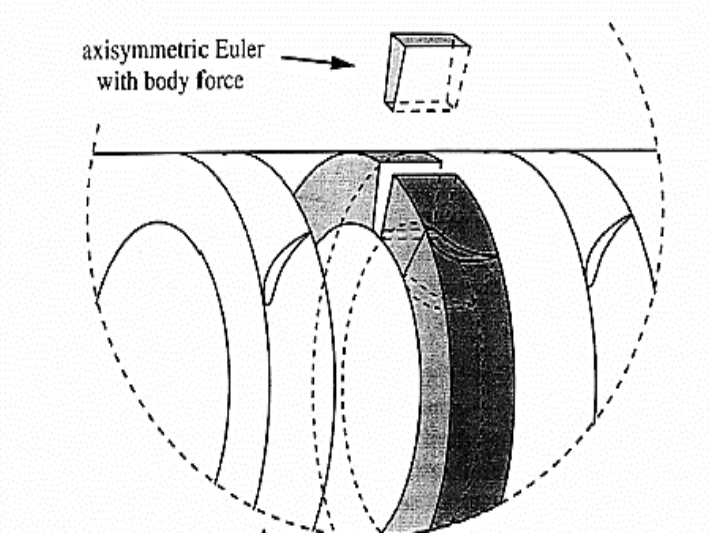

Figure 2.7 Gong *et al*`s blade row model [28]

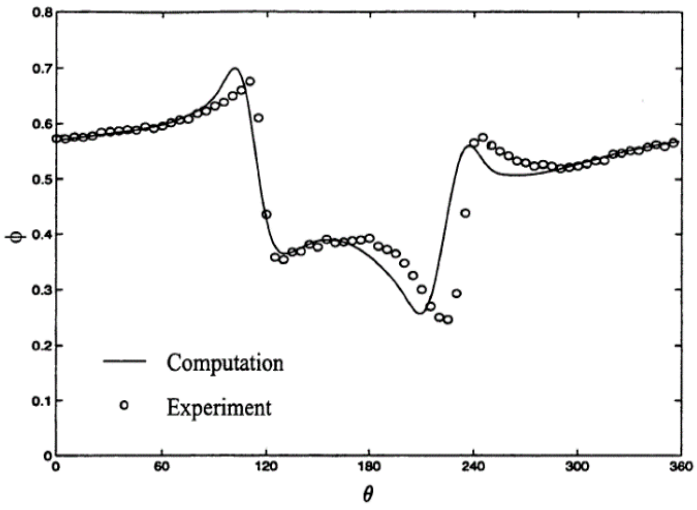

Figure 2.8 The computed and measured axial flow coefficient profile from the MIT three-stage compressor at low Mach number [28]

For simulation of inlet distortion in low hub-to-tip ratio compressor and fans, Hall *et al.* [17] developed an alternative body force approach to study the fan stage attributes that mitigate the effects of inlet distortion on performance. In this case, the body force source term was defined based on the local flow conditions and specified local blade camber surface geometry. The local body force at each node was computed to keep the flow tangent to the local blade camber surface. The flow was assumed to be inviscid since the authors mentioned that the flow mechanisms associated with distortion response were essentially inviscid. Therefore, this body force method can be implemented in CFD with the same type of simple cylindrical mesh as the method by Gong but only requires the 3D camber line geometry of the blades as input (rather the blade rows' performance characteristics) and as such, can account for blade performance variation along the span. As illustrated in Figure 2.9, Hall *et al*. [17] implemented their model in ANSYS CFX, a commercial RANS CFD solver, on a low-speed fan stage whose rotor had 20 blades and was subjected to the pattern of total pressure inlet distortion previously shown in Figure 1.6. The computational domain extended approximately two diameters both upstream of the spinner tip and downstream of the stator trailing edge. A quasi-steady assumption was made such that simulations were performed in steady mode. The results from the model were compared with test (measured) data for this fan, as shown in Figure 2.10, in terms of circumferential distributions at 25% and 75% span of axial velocity and absolute swirl angle at the rotor inlet and outlet (Stations

2 and 4, respectively, in Figure 2.9). The comparison showed that the model captures the effect of inlet distortion quite well. Through the use of this model, the authors also found that changes in stator design and rotor-stator spacing had an effect of the distortion evolution across the rotor and stage. Another paper from this research group [19], involving calculations of incompressible versus transonic flow (with shocks), found that the overall feature of flow redistribution under the effect of distortion was not sensitive to Mach number. While the results indicate that the model by Hall *et al.* [17] is quite versatile, it is still subjected to the limiting assumption of having the characteristic circumferential length-scale of the non-uniformity being much larger than the blade pitch, which may not apply to fans with relatively small number of blades.

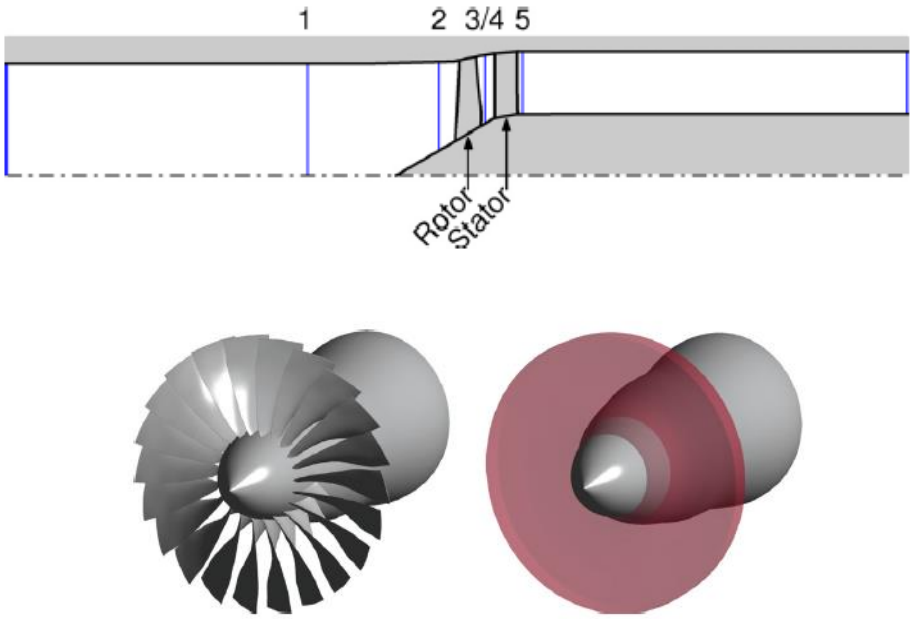

Figure 2.9 Three-dimensional modulization of fan stage, Hall *et al.* [17]

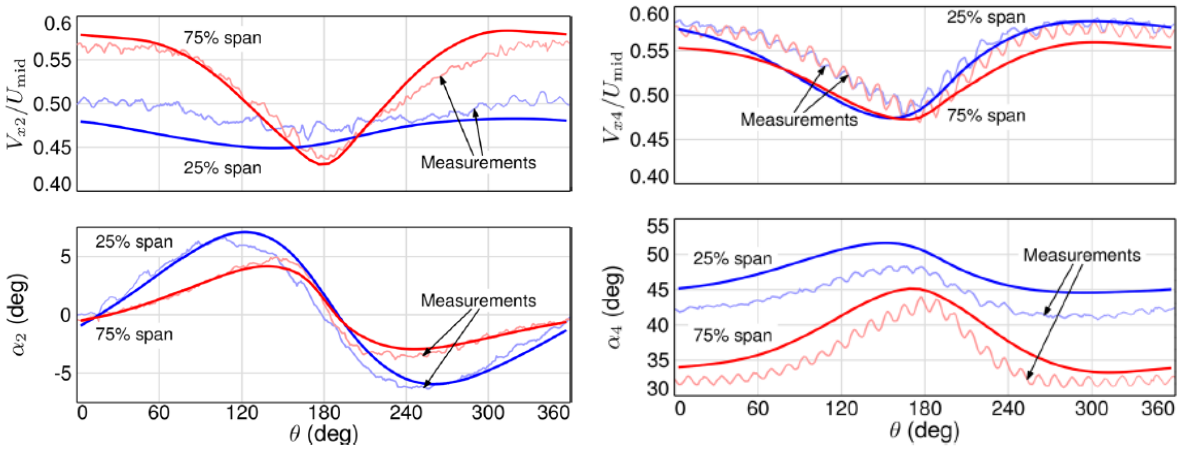

(a) Rotor inlet (plane 2) (b) rotor exit (plane 4)

Figure 2.10 Comparison of predicted and measured circumferential distributions of axial velocity and absolute swirl angle at (a) rotor inlet and (b) rotor exit [17]

Despite the computational cost, a few researchers have attempted to simulate the inlet distortion with full-annulus unsteady RANS CFD simulations. This type of simulations have the advantage of capturing blade-to-blade features, such as boundary layers, wakes, secondary flows, endwall losses and tip clearance flow structures that were not resolved in any of the models mentioned previously. Yao *et al.* [30] used high-performance computers and unsteady RANS calculations from an in-house CFD code with a k-epsilon turbulence model to perform full-annulus simulation on three multi-stage fans for which detailed data from distortion tests are were measured. The numerical simulations were carried out at the Aeronautical Systems Center running on an SGI *Origin* 3900 with 2048 processors. Figure 2.11 presents the full-annulus computational domain for the higher speed fan for a total of 313 million grid cells. Figure 2.12 shows the applied inlet and exit boundary conditions, namely the total pressure contours based on the distortion screen used in the corresponding tests and the exit static pressure contours re-created from pressure measurements coupled with through-flow calculations. Figure 2.13 compares the predicted and measured circumferential distribution of total pressure and temperature at different axial locations from the compressor inlet to exit at 50% span. These results indicate that the CFD simulation captures the evolution of the distortion through the compressor very well. Moreover, one can observe that the distortion is being amplified as it moves downstream through the compressor, but attenuates as it reaches the exit of the stage, likely due to the more uniform pressure distribution at the exit.

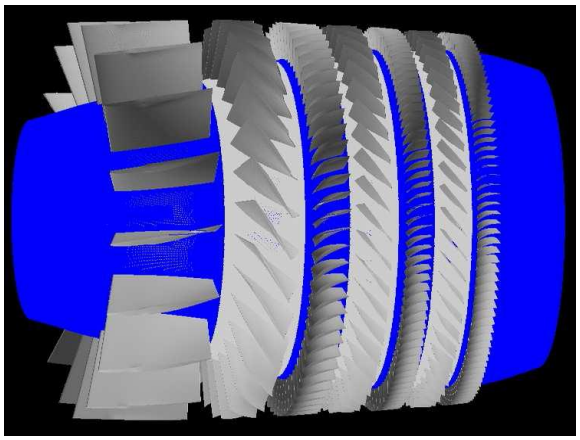

Figure 2.11 Computational domain for inlet distortion simulation of high-speed multi-stage fan [30]

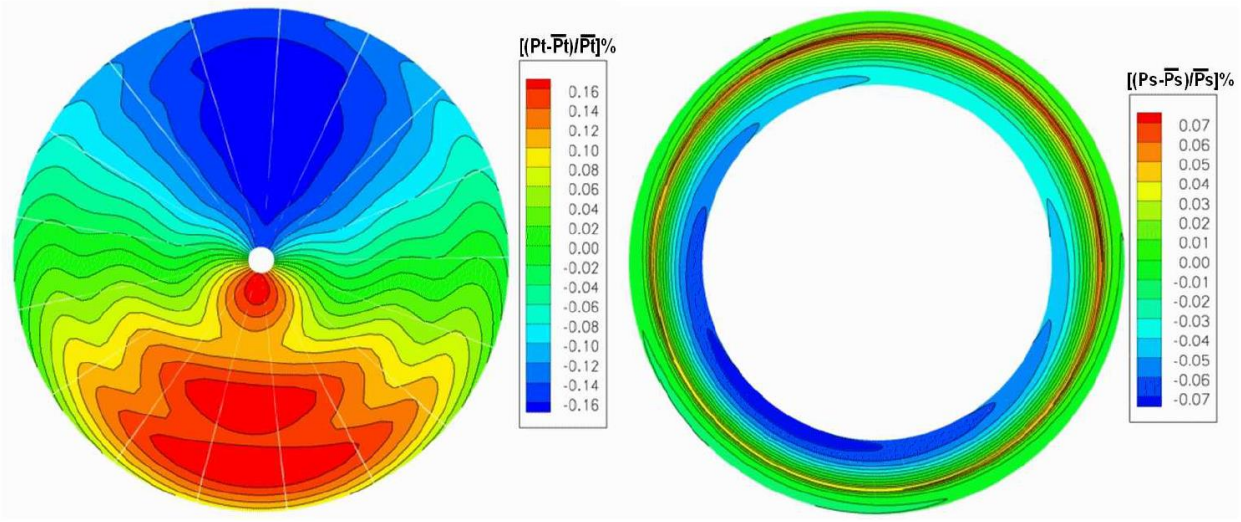

(a) Inlet total pressure (b) Exit static pressure

Figure 2.12 Inlet and exit boundary conditions used for inlet distortion simulation of high-speed multi-stage fan [30]

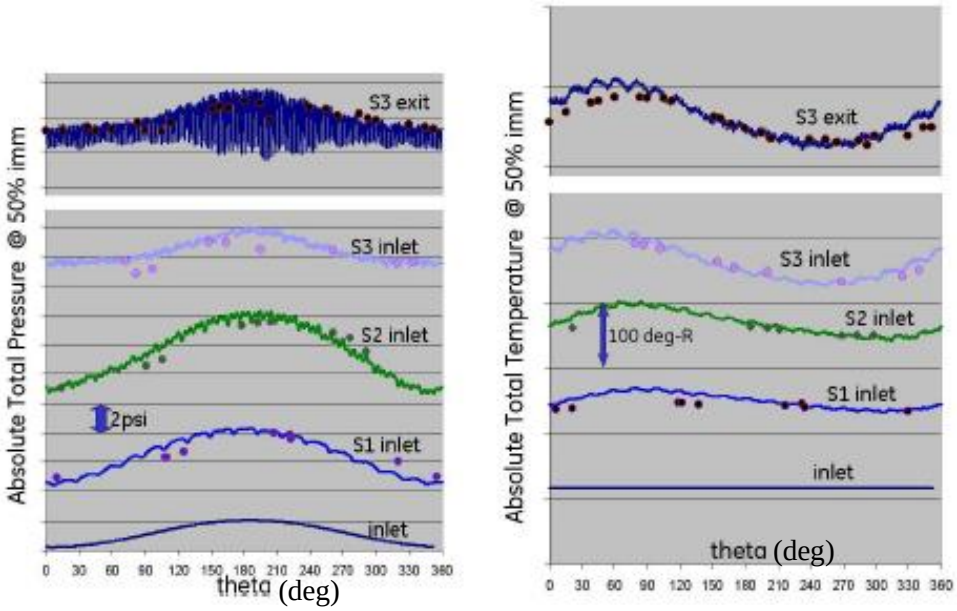

Figure 2.13 Predicted (line) versus measured (points) circumferential distributions of total pressure and temperature at different axial locations across high-speed multi-stage fan [30]

Jerez-Fidalgo *et al*. [31] carried out full-annulus, unsteady RANS CFD simulations of a transonic fan stage (NASA Stage 67) subject to an inlet total pressure distortion covering a third of the annulus, as shown in Figure 2.14. The comparison of the CFD predictions with test data, as reported in Figure 2.15, indicated that the CFD simulation captured the evolution of the distortion pattern through the rotor very well.

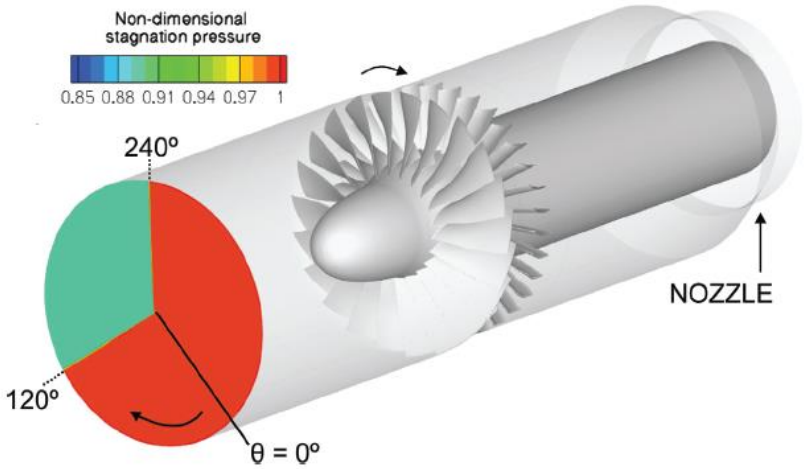

Figure 2.14 Total pressure distortion applied to NASA Stage 67 transonic fan stage [31]

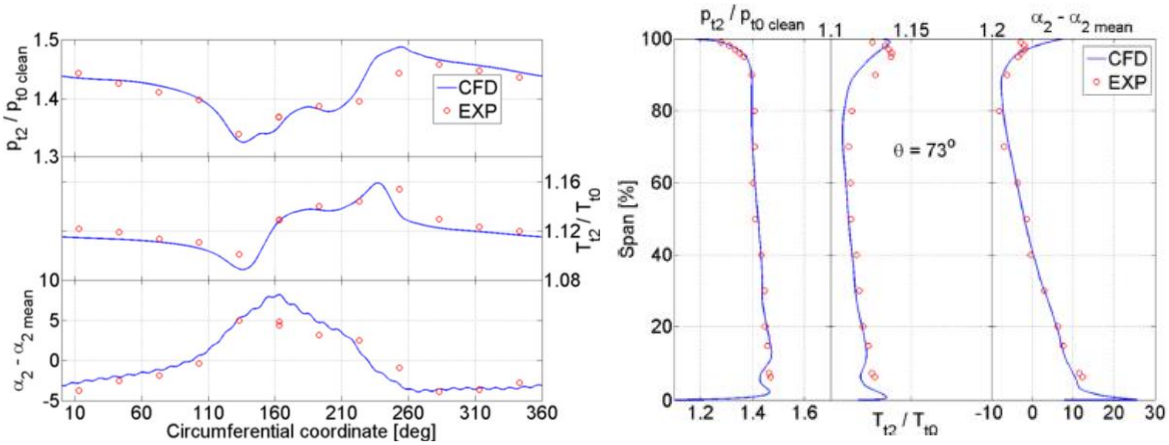

(a) Circumferential distribution at 50% span (b) Radial distribution at the 73 deg. point

Figure 2.15 Predicted (line) versus measured (points) distributions of total pressure, total temperature and swirl angle downstream of the NASA Stage 67 rotor [31]

Bakhle *et al*. [21] at NASA Glenn Research Center and United Technologies Research Center (UTRC) performed high-fidelity CFD simulations to investigate the dynamic stresses on blades from forced response of the fan to distorted inflows. They used full-annulus unsteady RANS CFD simulations to provide the blade surface pressure distributions used as input into a high-fidelity aero-elastic analysis code, which computed the fan blade vibration mode shapes and frequencies at design speed using commercial finite element analysis software. A structural model was also created to analyze the structural dynamics characteristics of the fan. Later, they examined the forced response at other rotational speeds where the engine order excitation frequency coincided with a blade natural frequency (resonance conditions). This tool was used to understand the effects of blade root fixity modeling on blade natural frequencies and mode shapes to produce distortion-resistant fan blades, to be discussed in section 2.3.

2.3 Management of Boundary Layer Ingestion Effect of Fan

While several studies have modeled and measured the effect of inlet distortion on compressors and fans, only a few published works exists on how to mitigate these effects. The mitigation approaches in these studies can be classified into two strategies.

The first strategy attempts to reduce the inlet distortion in the inlet duct before it reaches the engine face through flow mixing. Owens *et al*. [20] used a 0.3-meter Transonic Cryogenic Tunnel at NASA Langley Research Center to evaluate the effect of vortex generators and jet injection installed in a BLI inlet duct to induce flow mixing. Figure 2.16 shows their intake and measured total pressure distortion at the fan face location from the ingestion of a large boundary layer with a boundary-layer-to-inlet height ratio of 35%. The tunnel operated with total pressure ranging from 1 to 5.988 atm and Mach numbers ranging from 0.1 to 0.9. Figure 2.17 illustrates the positions and nature of the two flow control devices. A a set of vortex generators with height between 6.5% and 7.4% of fan diameter was positioned at the inlet and 176 1-mm-diameter high-speed jets orifices were placed perpendicular to the incoming flow. The corresponding operational range associated with the engine for this inlet corresponded to mass flow ratio values between 0.46 and 0.65. Figures 2.18 and 2.19 show the test results for flow control cases with jet injections and vortex generators at Mach 0.85. Figure 2.18 indicates that jet injection alone requires on the order of 2.5% of engine flow recirculation to bring the circumferential distortion below the distortion goal. The results in Figure 2.19 show that the vortex generators alone can bring the circumferential distortion below the acceptable level for higher inlet mass flow, but requires the addition of 0.4% jet injection for the lower mass flows. While these two flow control strategies may be effective, one disadvantage is that the associated mixing losses increased total pressure loss of the inlet by about 1%, reducing total pressure recovery of the duct to about 0.94, well below the value of about 0.98 for non-BLI intake ducts. The other drawback is the need to recirculate air from the engine compression system, which not only penalizes engine performance but also adds mechanical complexity leading to increased manufacturing and maintenance costs.

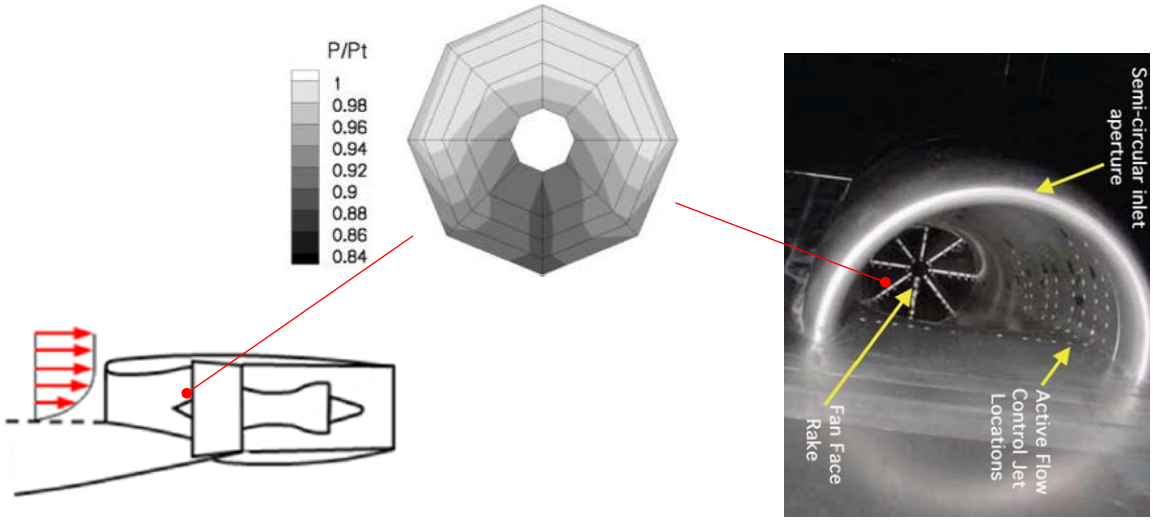

Figure 2.16 BLI test inlet with inlet total pressure distortion measured at fan face location [20]

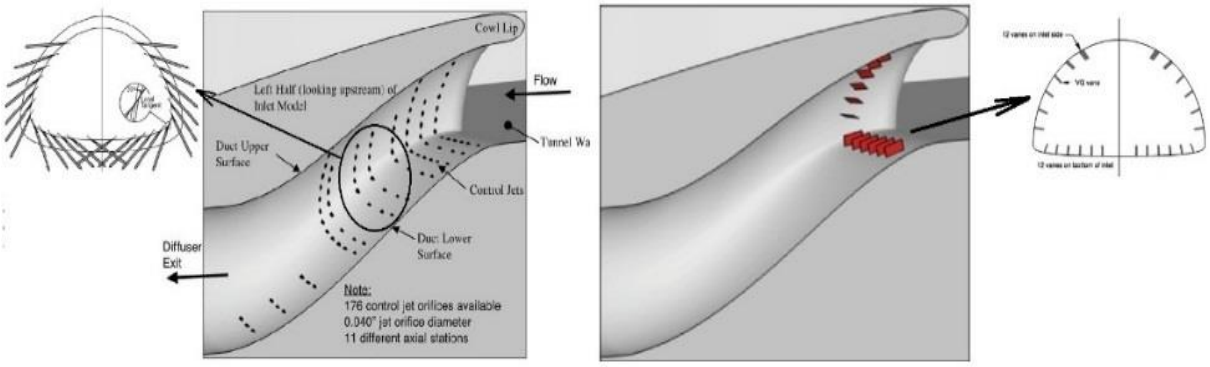

Figure 2.17 BLI test inlet cross section with location of available jet injectors (left) locations and vortex generators when installed (right) [20]

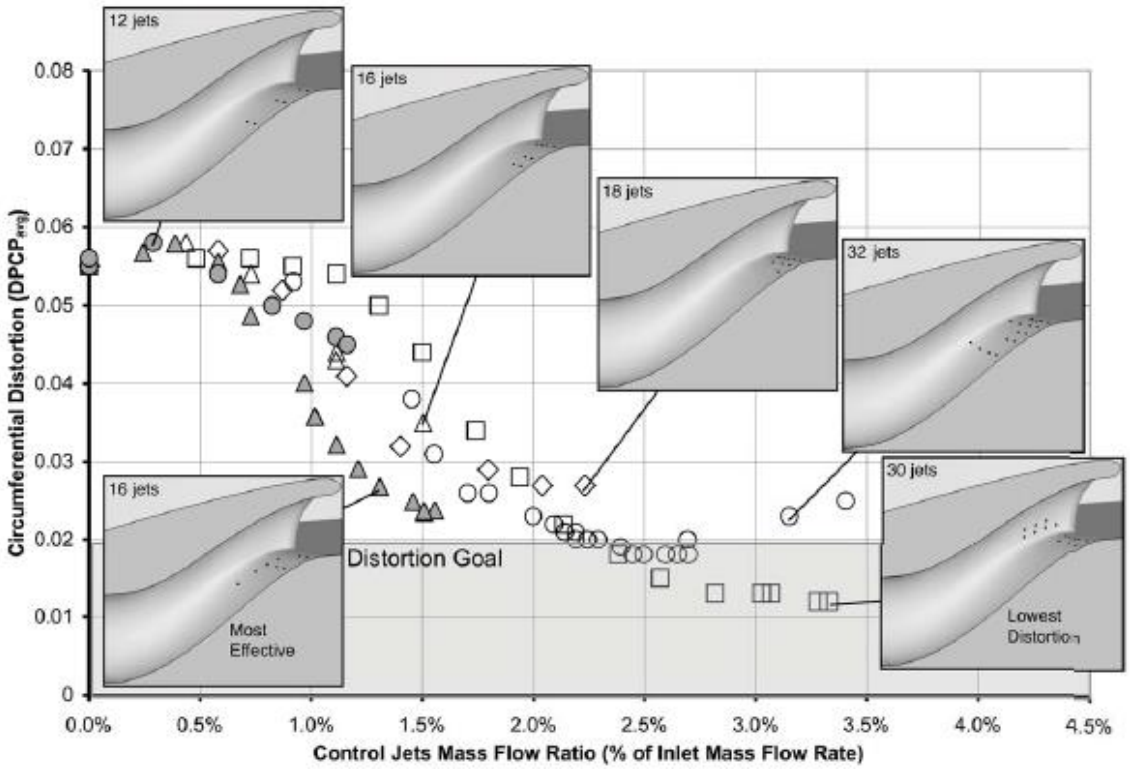

Figure 2.18 Effectiveness of jet injection in reducing circumferential inlet distortion [20]

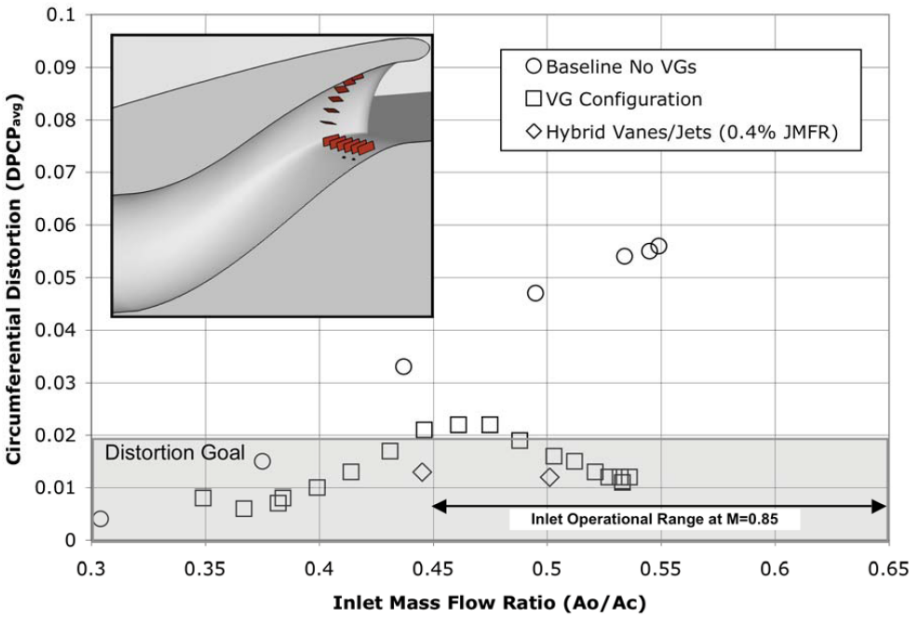

Figure 2.19 Effectiveness if vortex generators alone and combined with jet injection for reducing circumferential inlet distortion [20]

A common second strategy to address the negative effect of distortion is to design fan blades that can survive the stresses associated with inlet distortion. As previously mentioned in Section 2.2, NASA Glenn Research Center and United Technologies Research Center (UTRC) developed a high-fidelity simulation method combining aerodynamic and structural analysis to investigate the dynamic stresses on fan blades caused by inlet distortion [21]. They have since used this knowledge and tools to develop a distortion-tolerant fan by enhancing the structural-strength of the blade. Figure 2.20 shows this fan in its test environment [22]. Although no fan design details were given, a structurally reinforced blade design likely involved some compromises in terms of aerodynamic performance. Moreover, this strategy does not address the impact of the inlet distortion itself on the fan performance and operating envelope.

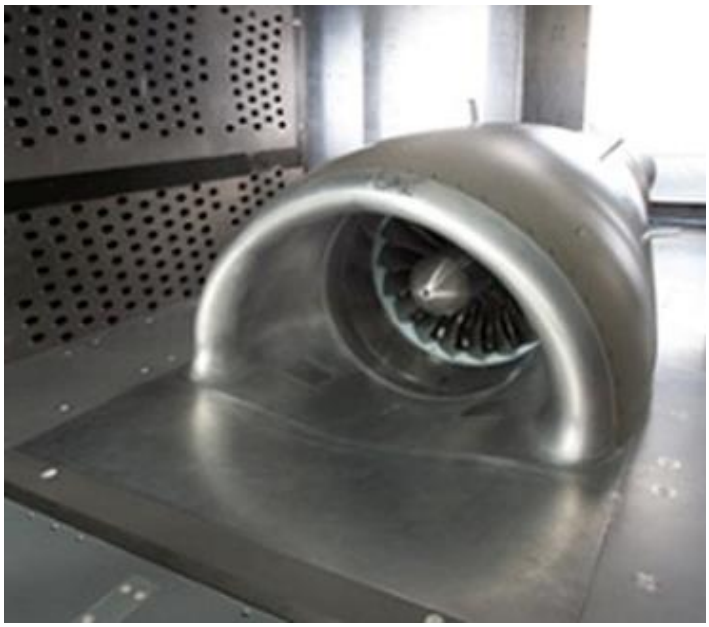

Figure 2.20 Boundary layer ingesting fan tested by UTRC and NASA [22]

2.4 Summary

Past experimental studies have indicated that inlet distortion is a serious issue at high (cruise) flight speeds, while did not affect engine performance significantly at low intake velocity. Various modelling approaches have been proposed to simulate the effect of inlet distortion on fans and compressors, range from the low-fidelity parallel compressor and actuator disks models

to full 3D unsteady RANS CFD. However, only the body force models and CFD can capture flow redistribution. While promising, the body force model by Hall *et al.* [17] required high-blade-count and cannot capture viscous effects, individual blade force and tip clearance effects. A full-annulus CFD simulation approach solved these issues, although it required excessive computational resources and time. However, a compromise between these two approaches could be found if one considers that the flow mechanisms associated with fan/compressor inlet distortion response may be essentially inviscid, which can be inferred from the results of Hall *et al.* [17]. In terms of managing BLI effect on fan, the two existing approaches have important drawbacks that may prevent them from being implemented commercially. Vortex generators and air jets can reduce the inlet distortion itself but incur mixing losses in inlet duct, which must be compensated by the engine, as well as increase integration and maintenance costs. On the other hand, fan blades with higher strength can involve aerodynamic performance trade-off and does resolve the performance penalty from inlet distortion.

CHAPTER 3 METHODOLOGY

The current study takes a numerical approach to assess the proposed asymmetric inlet guide vanes concept for three different fans. This approach provides the means to easily iterate upon the IGVs design as well as investigate its effect on the flow field. This chapter starts with a presentation of the fan geometries used in the assessment of the concept (Section 3.1) followed by a description of the IGVs design procedure (Section 3.2). Section 3.3 introduces the numerical setup for the three fans, while Section 3.4 describes the analysis procedure.

3.1 Fan Geometries

The preliminary assessment of the asymmetric IGVs concept is first performed on a low-speed fan rotor and subsequently on a high-speed (transonic) fan rotor to see how effective it would be at realistic high-speed conditions. Finally, the computational assessment is carried out on a low-speed fan stage of a distortion test rig that was designed and built in the middle of the current research to see if the concept could be experimentally validated on this rig. This section describes each geometry and the distortion pattern used to assess the asymmetric IGVs concept.

3.1.1 Low-Speed Fan Rotor

The first geometry is a preliminary evaluation of the asymmetric IGVs concept on a low-speed fan rotor aimed at developing a design process for such an IGV. While the rotor used by Hall *et al*. [17] would be a good candidate, its geometry is not available. Therefore, a low-speed fan rotor, the geometry and operating conditions given by ANSYS as a CFD tutorial is chosen, with tip Mach number and distortion pattern taken from Hall *et al*. [17]. This fan geometry is shown in Figure 3.1 and its operational characteristics are given in Table 3.1. The rotating speed is scaled to match the blade tip circumferential Mach number of the low-speed fan rotor analyzed by Hall *et al*. [17], while the inlet distortion pattern is obtained through Equation 3.1, with the inlet axial velocity scaling coefficient obtained from the distortion pattern in Hall *et al*. [17]. The resulting inlet total pressure distribution (distortion pattern) is shown in Figure 3.2.

$$P_{t\,in} = \left(P_{t\,in,undistorted} - \frac{1}{2}\rho w^2\right) + \frac{1}{2}\rho(coefficient \times w)^2 \tag{3.1}$$

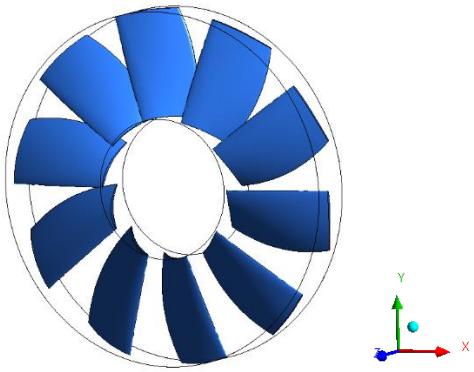

Figure 3.1 Geometry of the low-speed fan rotor

Table 3.1 Design parameters of the low-speed fan rotor

Parameter	Value
Fan tip radius	1.32 m
Fan hub radius	0.522 m
Number of fan blades	10
Tip clearance	0 mm
Fan tip stagger angle	75°
Rotor inlet tip Mach number	0.13
Mass flow rate	66 kg/s

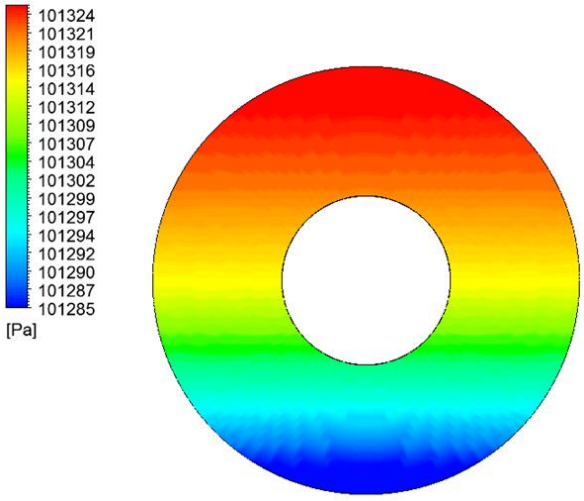

Figure 3.2 Inlet total pressure distribution for low-speed fan

Two parameters often used in inlet distortion studies are total pressure recovery and the distortion descriptor (DC_{60}). The former is defined as the ratio of the (mass-averaged) average total pressure at the exit of the inlet to the free stream total pressure. The distortion descriptor (DC_{60}) is a parameter often used to quantify the flow distortion at the engine face. Defined by Equation 3.2, this parameter compares the minimum averaged total pressure over any 60 degree wedge, $P_{\min 60.ave}$, to the averaged total pressure over the entire engine face plane, $P_{t.ave}$, normalized by the area-averaged dynamic pressure at the engine face, $q_{ef.ave}$[33].

$$DC_{60} = \frac{P_{t.ave} - P_{\min 60.ave}}{q_{ef.ave}} \times 100\% \tag{3.2}$$

Based on the above definitions, severe inlet distortion are associated with low the values for total pressure recovery and the distortion descriptor. For the studied distortion pattern of the low speed fan rotor, the total pressure recovery is 0.99985, and DC_{60} =93%, which indicates that this distortion is not severe.

3.1.2 High-Speed Fan Rotor

For more realistic aero-engine operating conditions, the concept needs to be evaluated on a transonic fan. The NASA Rotor 67 transonic fan is a well-known test case for CFD simulation of turbomachinery and both the (fan rotor) geometry [34] and measurements of the inlet distortion evolution [31] are available. The same rotor geometry and inlet total pressure (distortion) pattern [31], as previously shown in Figure 2.14 are used, with the latter rotated 120º counter-clockwise. For this distortion pattern, total pressure recovery is 0.9737 and DC_{60}= 66%, which is more severe than the low-speed fan. Given the high number of rotor blades, only the fan rotor was simulated to save computational time and resources. Figure 3.3 shows the simulated domain with the fan rotor and inlet distortion pattern, while Table 3.2 provides the high-speed fan design attributes.

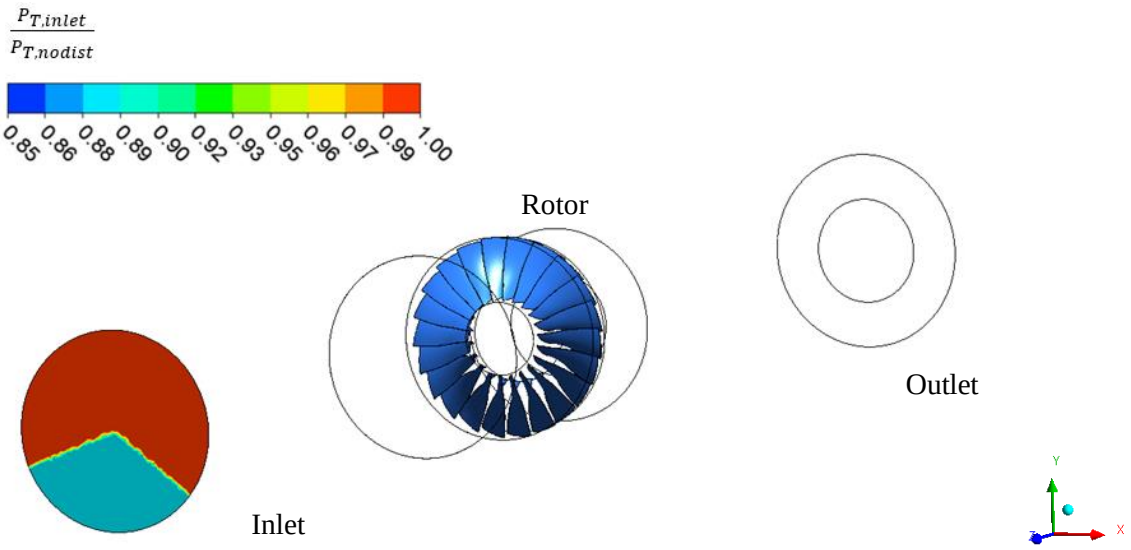

Figure 3.3 Simulated high-speed fan rotor geometry

Table 3.2 Design parameters of the high-speed fan rotor

Parameter	Value
Fan LE tip radius [cm]	25.70
Fan TE tip radius [cm]	24.25
LE hub-to-tip radius ratio	0.375
TE hub-to-tip radius ratio	0.478
Number of fan blades	22
Tip clearance [mm]	0
Rotor inlet tip Mach number	1.38
Mass flow rate [kg/s]	33.25

3.1.3 Test Fan Stage

Finally, in order to prepare for the experimental validation of asymmetrical IGVs concept, the last geometry chosen for study is a low-subsonic fan stage from a distortion test rig at Polytechnique Montréal, pictured in Figure 3.4 and designed in a 2018-2019 capstone project [32]. The test section and main instrumentation layout are illustrated in Figure 3.5. The test

section incorporates a single-stage fan preceded by a row of straight IGVs, with constant hub and tip radii throughout. The rotor and stator both have a tip clearance. This setup allows for two rotating casings on which are three Kiel probes placed on radial traverses located just upstream of the IGVs, between the rotor and stator and just downstream of the stator to measure the full-annulus total pressure distribution at these three axial locations. Mass flow is obtained from inlet total pressure (ambient air pressure) and Bellmouth exit, while static pressure ports are placed around the shroud at the exit of the stator to obtain the total-to-static pressure rise of the fan. An annular throttle valve on the plenum periphery allows for control of mass flow. The horizontal inlet distortion was generated by a screen placed on a honeycomb support converting the entire inlet cross-section upstream of the fan.

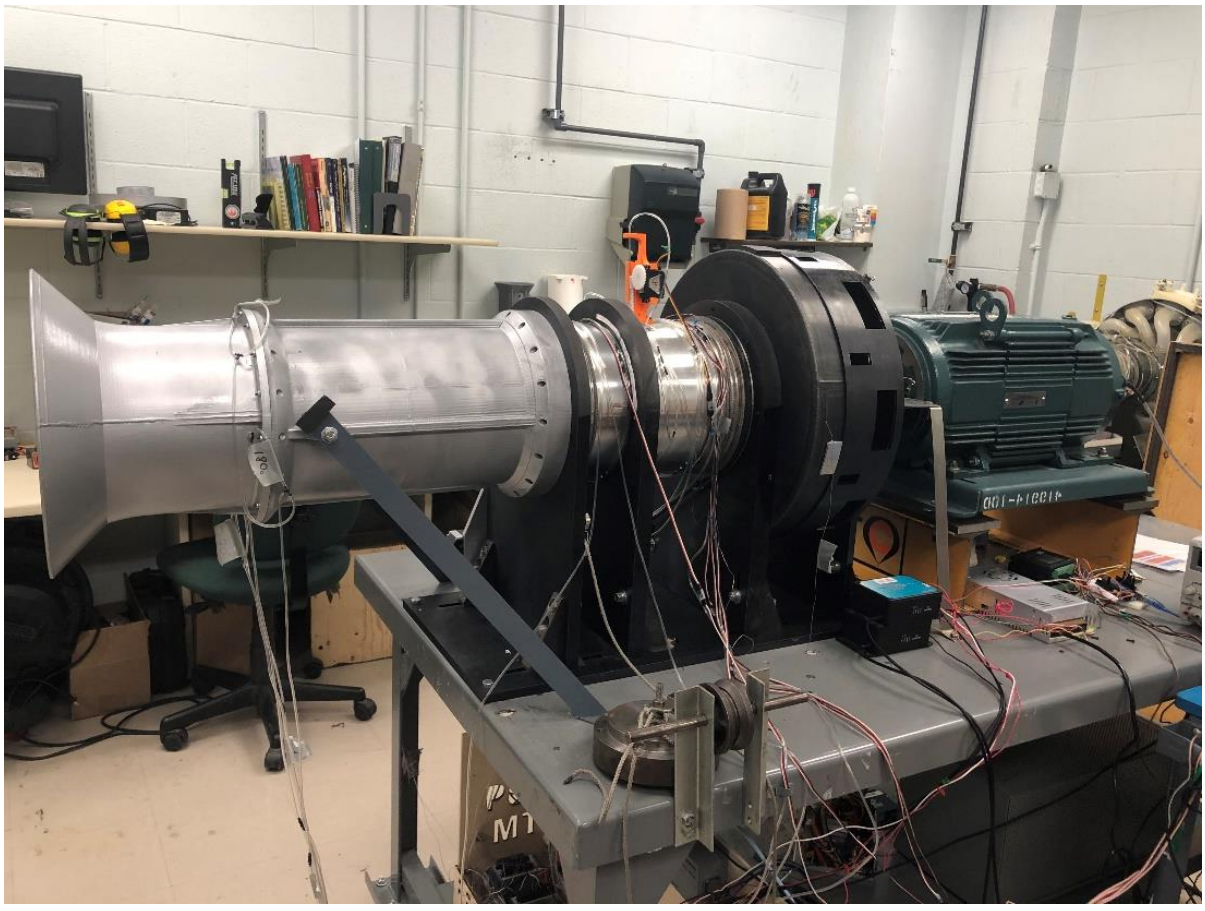

Figure 3.4 Low-speed fan distortion test rig [32]

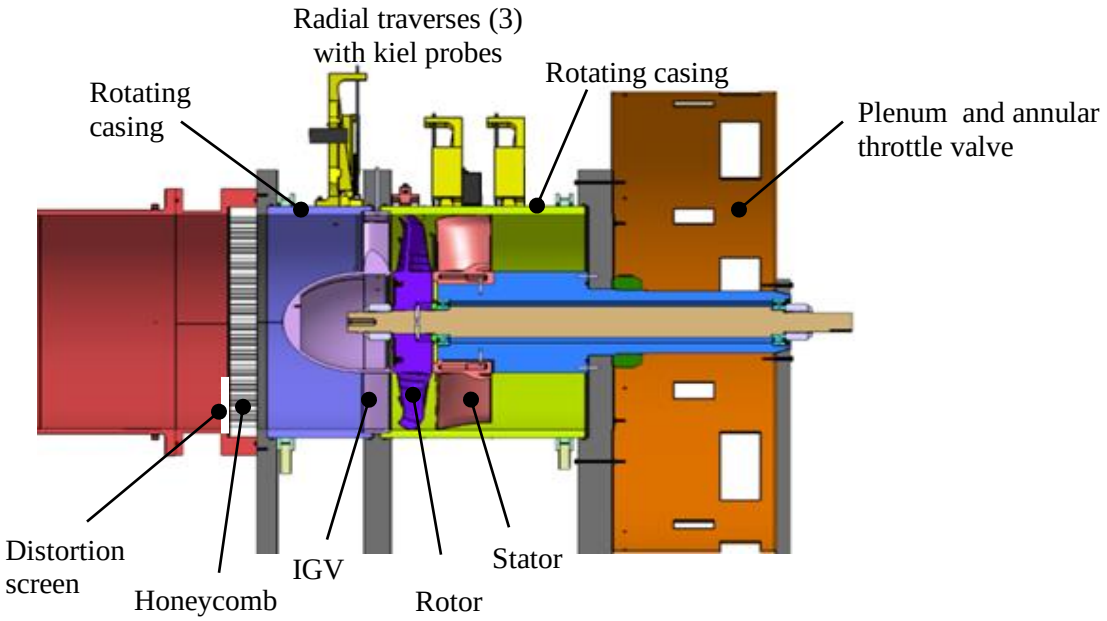

Figure 3.5 Low-speed fan distortion rig test section [32]

Figure 3.6 shows the simulated domain with the test fan stage and inlet total pressure distribution, that is obtained through iteration to match the distortion pattern measured just upstream of the IGVs in the test rig. For this distortion pattern, total pressure recovery is 0.9942 and DC_{60}= 70%, indicating that the distortion is more severe than that of low-speed fan but less than that of the high-speed fan. Moreover, given that the distortion is generated from screen placed far downstream of the computational domain inlet, an artificial inviscid horizontal surface (flow separator) is placed along the distortion boundary between the domain inlet and the axial location of the distortion screen to prevent a premature start of flow redistribution between the distorted and undistorted regions. This better simulates the flow in the test rig. Table 3.3 lists the design parameters of the test fan stage.

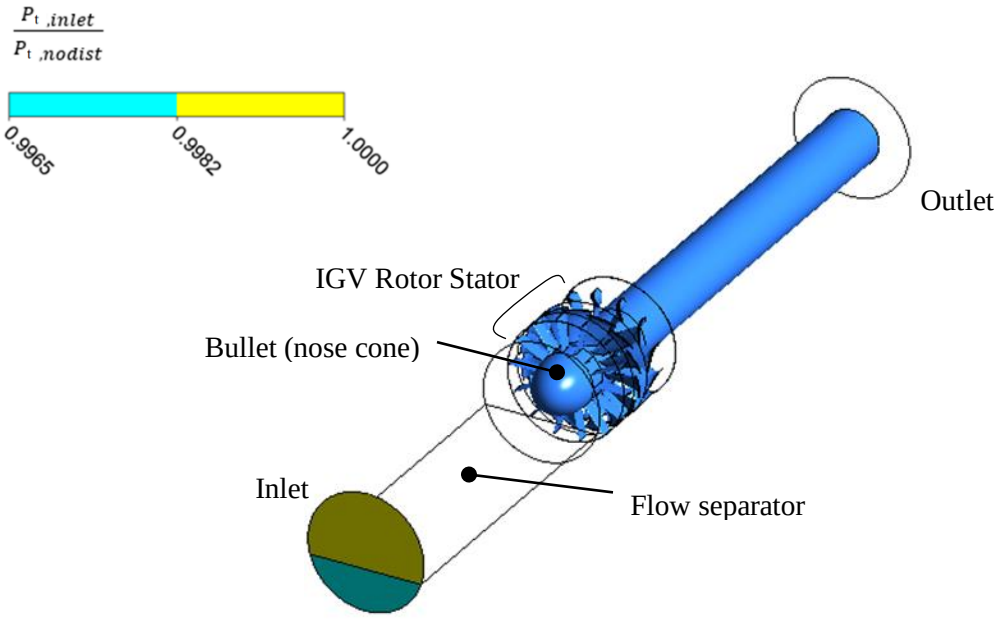

Figure 3.6 Simulated test fan stage geometry

Table 3.3 Design parameters of the test fan stage [32]

Parameter	Value
Fan tip radius [m]	0.1075
Fan hub radius [m]	0.0508
Number of IGV blades	14
Number of rotor blades	15
Number of stator blades	14
Tip clearance [mm] (rotor and stator)	0.254
Rotor inlet tip Mach number	0.024
Mass flow rate [kg/s]	0.9

3.2 Numerical Setup

Based on the statement by Hall *et al.* [17] that the flow mechanisms associated with a fan response to inlet distortion are essentially inviscid and backed up by the success of their model, a slightly different simulation approach is proposed for the current study. It consists of full-annulus CFD simulations but in inviscid mode without tip clearance. These two features allow for a much coarser mesh since the higher mesh density near surfaces and in the tip region for capturing boundary layers and tip clearance flow are not required. The coarser mesh coupled with the absence of calculations associated with a turbulence model, render the simulation much faster and less resource intensive than traditional full-annulus RANS CFD simulations. To avoid the need for programming a new 3D Euler CFD code along with processing tools, the commercial RANS ANSYS CFX code is selected since the CFD tool given its option to be run in inviscid mode (zero viscosity, free slip wall boundary conditions and no tip clearance). While this approach is suitable for the low-speed fan rotor and high-speed fan rotors, the selection of ANSYS CFX provides the option to carry out full-annulus viscous simulations with tip clearance for the low-speed test fan stage in preparation for implementing the asymmetric IGVs concept on the fan test rig to experimentally validate it.

As illustrated in Figures 3.3 and 3.6, the computational domain typically incorporates a rotating subdomain for the fan rotor, and adjacent stationary subdomains for neighboring blade rows (IGV and stator) if present, sandwiched between stationary upstream and downstream duct subdomains whose lengths are about one fan tip circumference in length. The chosen duct lengths allows for potential perturbations at the fan with wavelengths on the order of the circumference to attenuate to zero amplitude at the inlet and exit. The subdomains for the fan blade rows and inlet/exit duct have structured meshes created with ANSYS *TurboGrid*. The subdomains for the bullet (nose cone), when present, and asymmetric IGVs use unstructured meshes created with ANSYS *Mesh*. A general connection interface is applied between adjacent stationary subdomains across which the flow properties are simply interpolated. At the boundaries between adjacent subdomains with relative motion, such as IGV-Rotor or Rotor-Stator, a *frozen rotor* interface is used for steady-state simulations. This interface option in ANSYS CFX supposes that the rotor relative angular position to the stationary domain (inlet distortion pattern and IGV blades) is fixed even though the relative position actually changes in time. While not entirely physical, this

interface option is the only one that allows for the transfer of circumferential flow non-uniformity between adjacent subdomains in relative motion in a steady simulation. For unsteady simulations, the *frozen rotor* interfaces are replaced by standard sliding plane interfaces where the flow non-uniformity is passed from one domain to another by interpolation at every time step. The inlet boundary conditions consist of specified total pressure, total temperature and axial flow, while the exit condition is a specified mass flow. When inlet distortion is present, the associated spatial distribution of total pressure over the inlet surface is input via a *Profile.csv* file in ANSYS CFX. Each simulation starts out in steady-state mode, the solution is then used as the initial guess for the unsteady simulation in order to accelerate convergence. The time step size is chosen to provide 20 time steps per rotor blade passing, which is in the range of what is typically used. However, a study on the number of time steps per blade passing is done, the results from which are provided in Appendices B though D (sections B.2, C.2 and D.2) for the three studied geometries. The main convergence criteria are mass flow rate (inlet/outlet balance – usually within 0.1%) and momentum residuals (generally set to 10^{-6}). In unsteady simulations, the number of time steps required can be estimated by the time required for a fluid particle (whose averaged velocity is taken conservatively as the inlet axial velocity in the distorted flow region) to travel the length of the computational domain. All simulations and analysis are carried out at the design mass flow.

More information on the numerical setup specific to each studied fan geometry is provided in the following subsections.

3.2.1 Low-speed fan rotor

Figure 3.7 shows the computational domain and mesh for the simulations of the low-speed fan rotor. The bullet is not simulated such that the fan hub extends upstream to the inlet domain and the inlet plane is annular rather than circular in shape. The simulation is purely inviscid with no tip clearance. The structured mesh is that recommended by ANSYS *TurboGrid* for this fan rotor (whose geometry is provided as an example in ANSYS) with the total domain mesh size of 1.23 million nodes (1.76 million nodes with IGV). The computational domain consists of the inlet duct, rotor and exit duct subdomains. When the IGVs are present, the inviscid IGV subdomain is meshed and imported from ANSYS Mesh and inserted between the inlet duct and the rotor subdomains. Table 3.4 summarizes the settings used for the simulations in CFX.

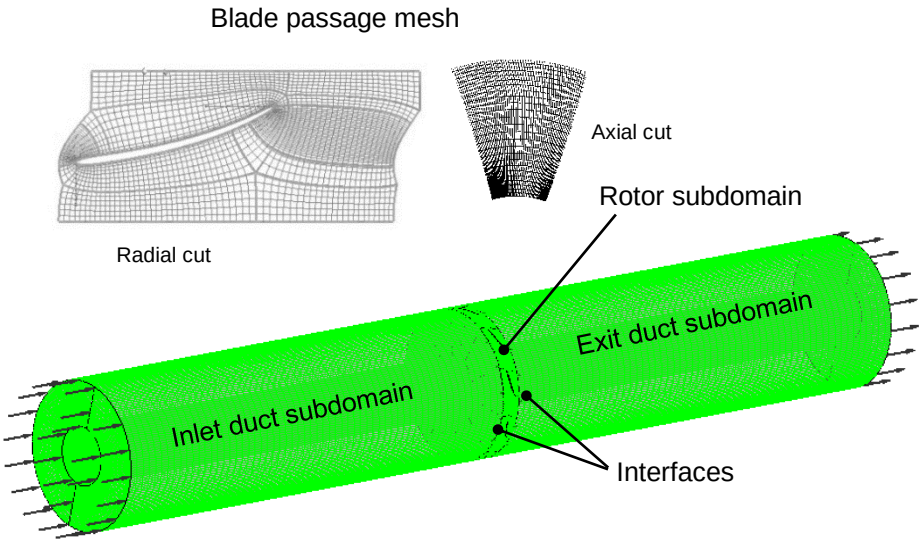

Figure 3.7 Computational domain and mesh for low-speed fan rotor

Table 3.4 Simulation parameters for low-speed fan rotor

Option settings	Selection	Justification
Analysis Type	Steady / unsteady	
Material	Air ideal gas	Compressible gas
Heat transfer	Total Energy	Define the temperature at inlet
Inlet boundary condition	Total pressure, total temperature, axial flow	
Inlet total temperature	273 K	
Mass and momentum of all blades	Free slip wall	No friction
Hub and shroud	Free slip wall	No friction
Angular velocity of fan	33.77 rad/s	$U_{tip} = \Omega \times R_{tip}$
Interface (steady)	Frozen rotor	Required
Interface (unsteady)	Transient rotor stator	Required
Outlet boundary condition	Mass flow rate 66 kg/s	Estimate
Interface between fan inlet and outlet	Frozen rotor Specified pitch angle	Rotate 360° together
Advection scheme	High resolution	High precision
Time-step (unsteady)	9.305×10^{-4} s	The pitch is divided into 20 segments
Simulated time (unsteady)	2.25 s	Approximate convection of slowest fluid particle
Residual	10^{-6}	Experience
Platform MPI local parallel	8	I7 4790 CPU
Typical convergence time	~2 weeks	

3.2.2 High-Speed Fan

The computational domain for the high-speed fan (NASA Rotor 67) is illustrated in Figure 3.8, consisting of four main subdomains: the inlet duct, bullet (nose cone), rotor and outlet duct subdomains. The rotor geometry is obtained from [34]. As shown in the zoomed central section in Figure 3.8, the parts of the bullet/exit duct subdomains adjacent to the rotor subdomain are made up of transition sections. These sections link the blade passage structure of the rotor subdomain to the cylindrical structure of the bullet/exit duct subdomains. When present, an IGV subdomain is placed just upstream of the rotor subdomain. The simulation is purely inviscid with no tip clearance.

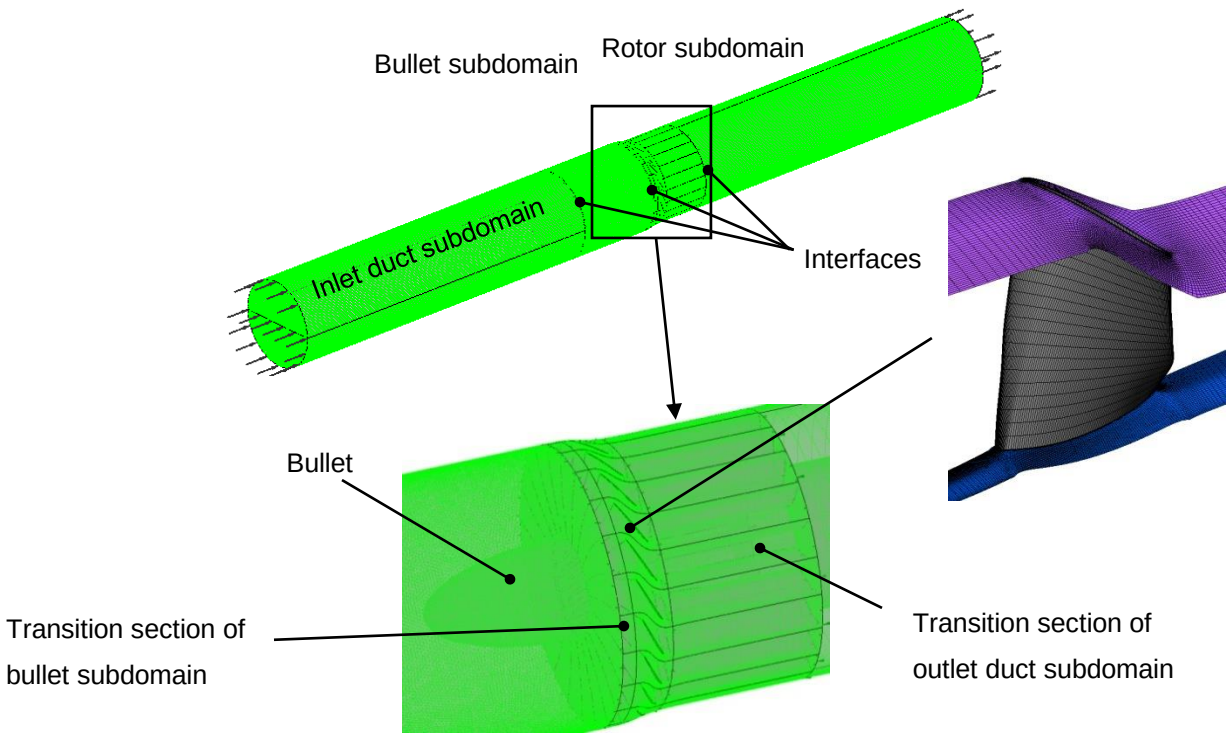

Figure 3.8 Computational domain for high-speed fan

However, given the transonic nature of the flow and consequent presence of shocks, more care was needed for the selection of the mesh. A mesh study is carried out on the rotor using single blade passage simulations with the domain shown in Figure 3.9a. Figure 3.9b shows the three mesh sizes used in the mesh study: coarse (107,294 nodes), medium (185,460 nodes) and dense (360,712 nodes). The high-quality structured mesh is created with ANSYS *TurboGrid*. The mesh

topology set is made with the Automatic Topology and Meshing (ATM Optimized) feature. Figure 3.10 plots the total pressure ratio of rotor 67 at 100% rated speed versus number of nodes. The results show that the medium grid is adequate. Figures 3.11 and 3.12 indicates that the predicted Mach number contours with the medium grid match well with corresponding test data taken at 30% span and 90% spans from [35]. As such, the medium grid is chosen for the rotor subdomain in Figure 3.8.

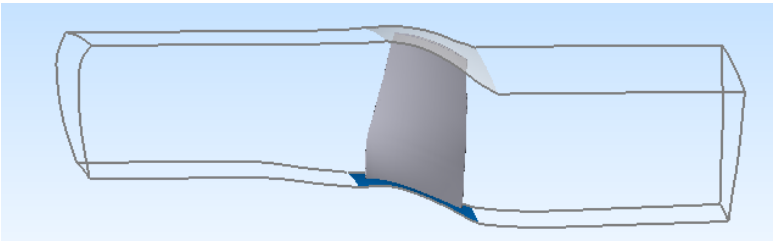

(a) Single-passage computational domain

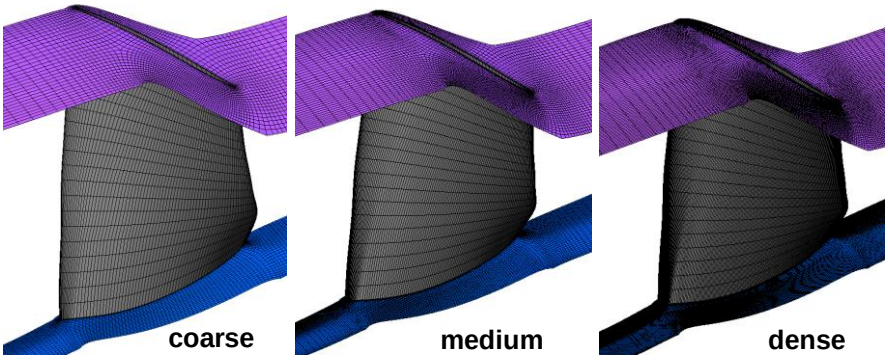

(b) Mesh sizes used in mesh study

Figure 3.9 Domain setup for mesh study

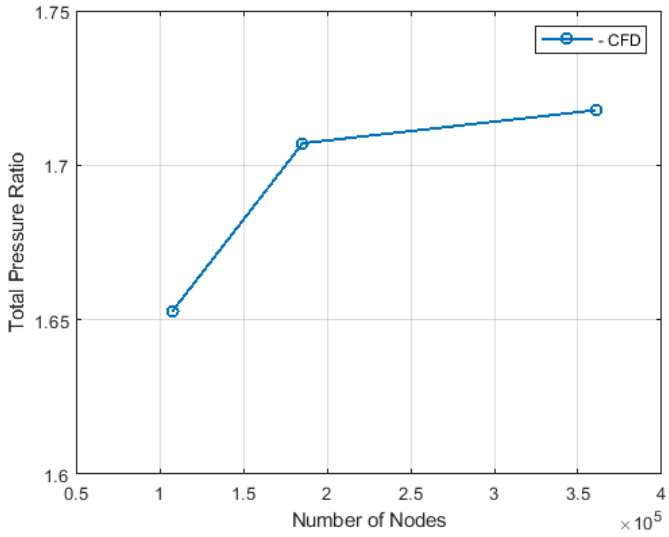

Figure 3.10 Rotor 67 total pressure ratio at 100% rated speed versus number of nodes

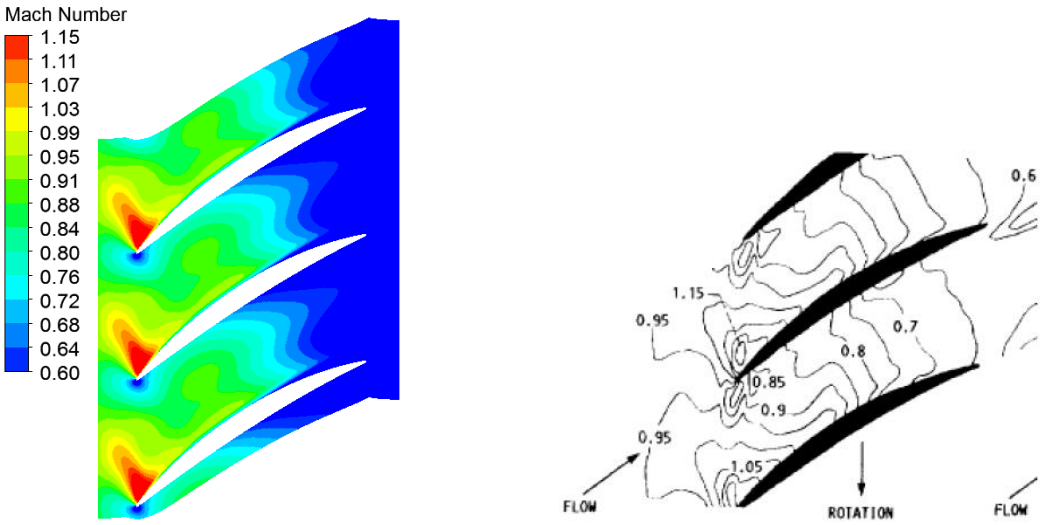

(a) CFD Mach number contour for medium mesh (b) Exp. Mach number contour [35]

Figure 3.11 Mach number contours comparison between CFD results and experimental data at 30% span

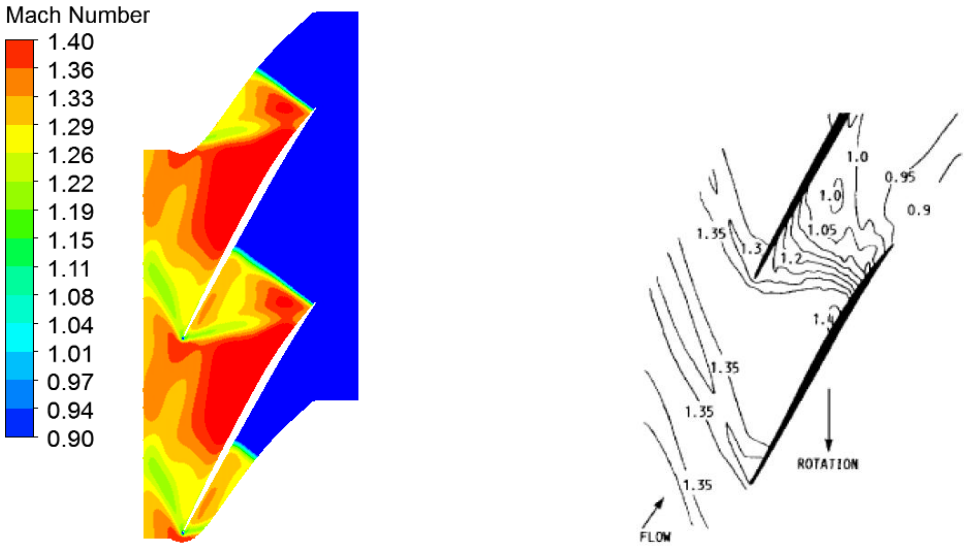

(a) CFD Mach number contours for medium mesh (b) Exp. Mach number contours [35]

Figure 3.12 Mach number contours comparison between CFD results and experimental data at 90% span

The mesh density of the other subdomains in Figure 3.8 is set to the value of the rotor subdomain at their interfaces. As such, the inlet duct, bullet, rotor and outlet duct subdomains domain have about 199,000, 2,484,000, 733,000 and 600,000 elements, respectively. The settings used for the simulations in CFX are listed in Table 3.5. While a specified total temperature would be a standard inlet boundary condition, it resulted in convergence problems in full-annulus simulations characterized by oscillating mass flows even in the absence of inlet distortion. This problem may be due to the high-resolution advection scheme, which is more accuracy on unstructured mesh for the bullet subdomain, however, has low stability. In particular, the complex fluid of the high-speed rotor and the outlet condition is the specified mass flow. This issue was resolved by using a specified static temperature inlet condition. A comparison between the total versus static temperature inlet boundary conditions carried out for the low-speed rotor shows that blade force and total pressure at the exit of the fan change very little, as shown in Appendix B (Section B.4).

The final numerical setup is validated by comparing the full-annulus simulations with published CFD and test data [31]. Figure 3.13 presents the total pressure ratio characteristics for the rotor 67 alone operating with uniform, clean inflow at 90% rotational speed against the test data and 3D (viscous) RANS CFD prediction from [31]. In these early simulations, an outlet static

pressure is used to move up the speed line. The results show that the current numerical setup captures the trend well with a slight over estimation of the pressure rise due to the lack of viscosity. Next, a comparison of the simulated flow field under inlet distortion is compared to corresponding 3D (viscous) RANS CFD predictions from [31] in Figures 3.14 through 3.16. Despite its inviscid nature, the proposed CFD setup captures the right trend as indicated by the matching locations of the regions of maximum and minimum values of the mass flux, whirl angle and total pressure ratio as indicated by circles in Figures 3.14, 3.15 and 3.16.

Table 3.5 Simulation parameters for high-speed fan rotor

Option settings	Selection	Justification
Analysis type	Steady / unsteady	
Material	Air ideal gas	Compressible gas
Heat transfer	Total energy	Define the temperature at inlet
Inlet boundary condition	Total pressure, static temperature, axial flow	
Inlet static temperature	288.15 K	
Mass and momentum of all blades	Free slip wall	Inviscid surfaces
Hub and shroud	Free slip wall	Inviscid surfaces
Angular velocity of fan	1511 rad/s (90% rated speed)	$V_{tip} = \Omega \times R_{tip}$
Interface rotating/stationary (steady)	Frozen rotor	Required
Interface rotating/stationary (unsteady)	Transient rotor stator	Required
Outlet boundary condition	30.76 kg/s	Estimated value
Specified pitch angle	Rotate 360°	
Time-step (unsteady)	8.5×10^{-6}s	20 time steps per blade passage
Simulated time (unsteady)	0.056 s	Approximate convection of slowest particle
Residual	10^{-6}	Experience
Platform MPI local parallel	8	I7 4790 CPU and 128G RAM
Intel MPI distributed parallel in Compute Canada server	32	2 x Intel E5-2683 v4 Broadwell @ 2.1GHz and 125G RAM
Typical convergence time	~ 5 weeks	

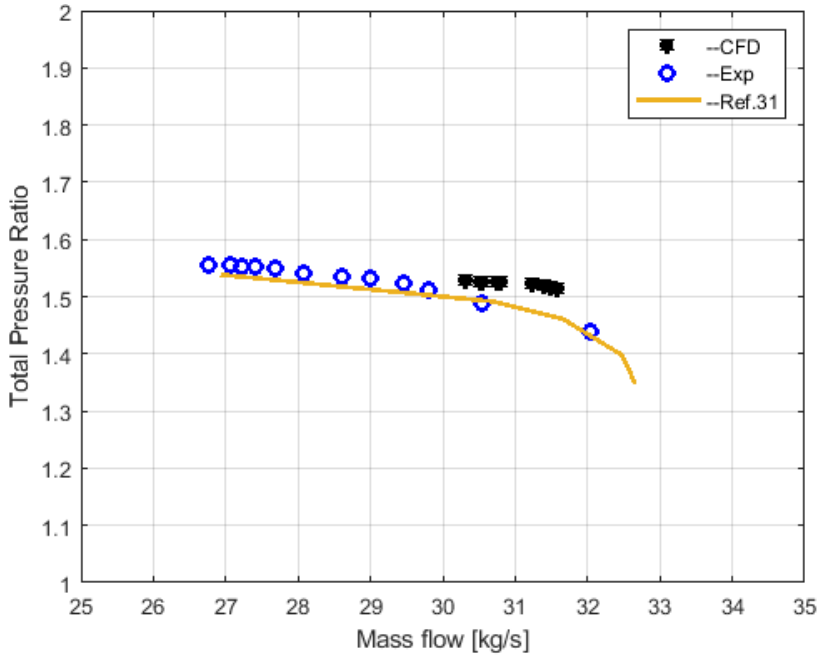

Figure 3.13 Total pressure ratio for Rotor 67 at 90% rated rotational speed [31]

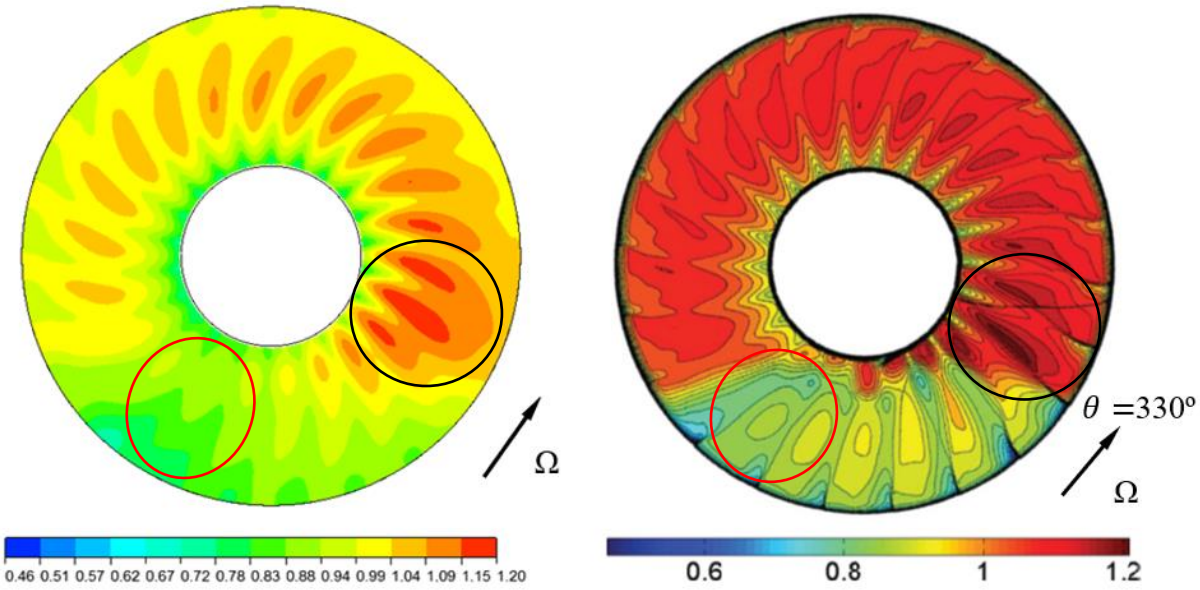

(a) CFD (b) Jerez Fidalgo *et al*. [31]

$$\frac{(\rho V_x)_{LE}}{(\rho V_x)_{inlet\ clean}}$$

Figure 3.14 Mass flux contours at rotor LE

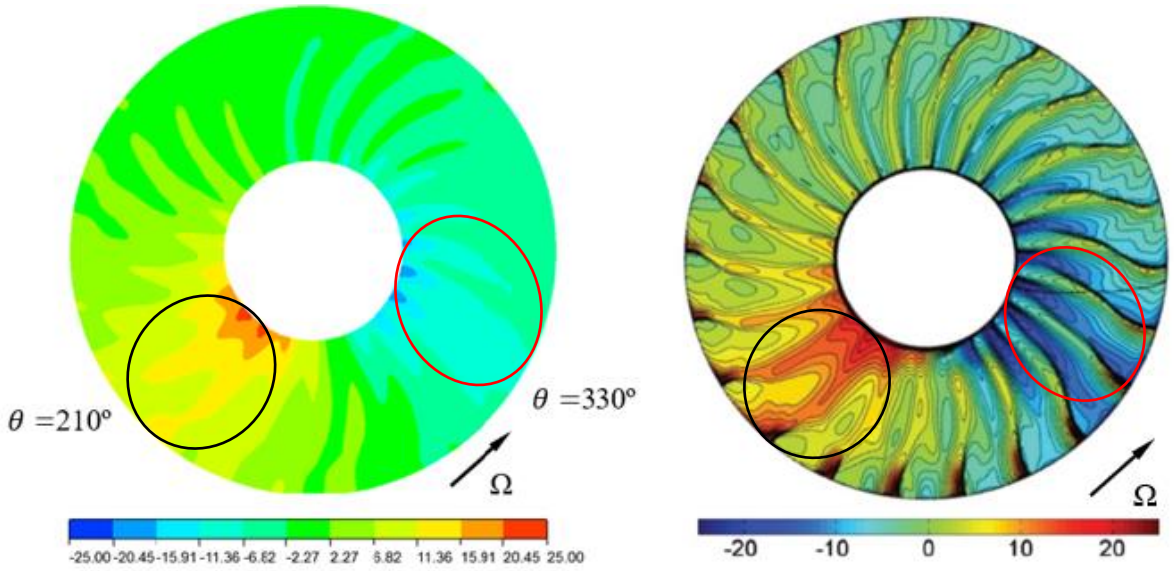

(a) CFD (b) Jerez Fidalgo *et al*. [31]

Figure 3.15 Absolute whirl angle at rotor LE

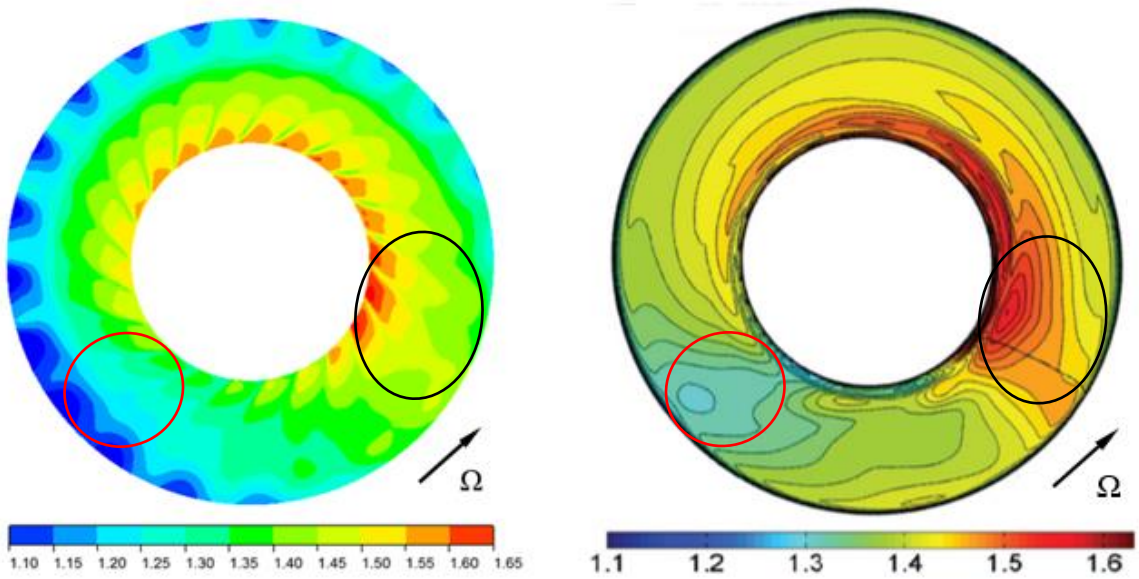

$$\frac{P_{t,TE}}{P_{t,inlet\ nodist}}$$

(a) CFD (b) Jerez Fidalgo *et al*. [31]

Figure 3.16 Total pressure ratio contours at rotor TE [31]

3.2.3 Test Fan Stage

As illustrated in Figure 3.17, the computational domain for the test fan stage consists of six subdomains: the inlet duct, bullet, IGV, rotor, stator and outlet duct subdomains. Given that the goal of designing the asymmetrical IGVs to experimentally validate the concept on the corresponding fan test rig, the simulations for this fan geometry was carried out to replicate, as closely as possible, the actual test rig, by incorporating viscosity on all solid surfaces and tip clearances on the rotor and stator. The chosen mesh for the rotor and stator, as shown in Figure 3.18, is based on the results of a mesh study in the design report of the fan test rig [32]. The mesh for the IGV subdomain (not shown) as well as the regions of the inlet/exit duct subdomains near the IGV and stator have a similar mesh density to that of the rotor and stator. The resulting number of the nodes for the inlet duct, bullet, IGV, rotor, stator and outlet duct subdomains are, respectively, 223,000, 105,000, 2,017,000, 3,106,000, 3,275,000 and 226,000. Table 3.6 lists the settings used for the simulations in CFX.

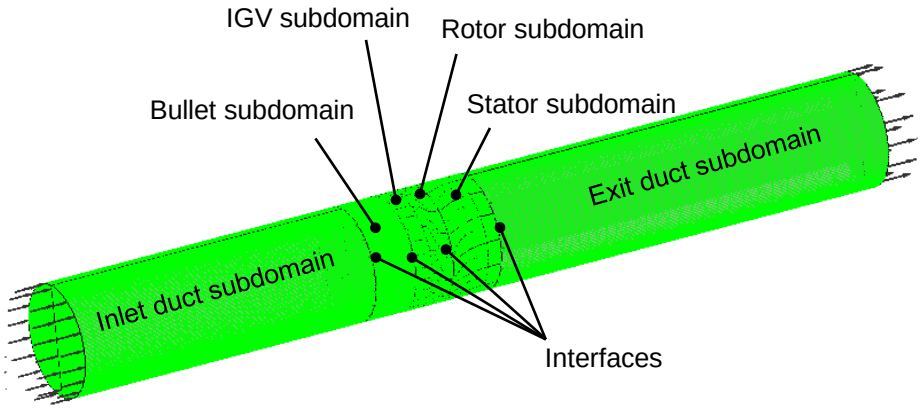

Figure 3.17 Computational domain for test fan stage

To save simulation time for the no-distortion of the test fan, the computation domain in Figure 3.17 is split in two parts. The first just includes the inlet duct subdomain, while the second part includes the bullet, IGV, rotor, stator and outlet duct subdomains. A steady simulation was carried out on the inlet duct subdomain alone at the design mass flow to obtain the total pressure distribution associated with the inlet shroud boundary layer. This total pressure distribution is

then applied as the inlet total pressure boundary condition at the entrance of the bullet subdomain, as illustrated in Figure 3.19, to simulate the rest of the fan domain. It was noted that due to the unstructured mesh in the bullet subdomains, the applied inlet total pressure contours is not perfectly axisymmetric.

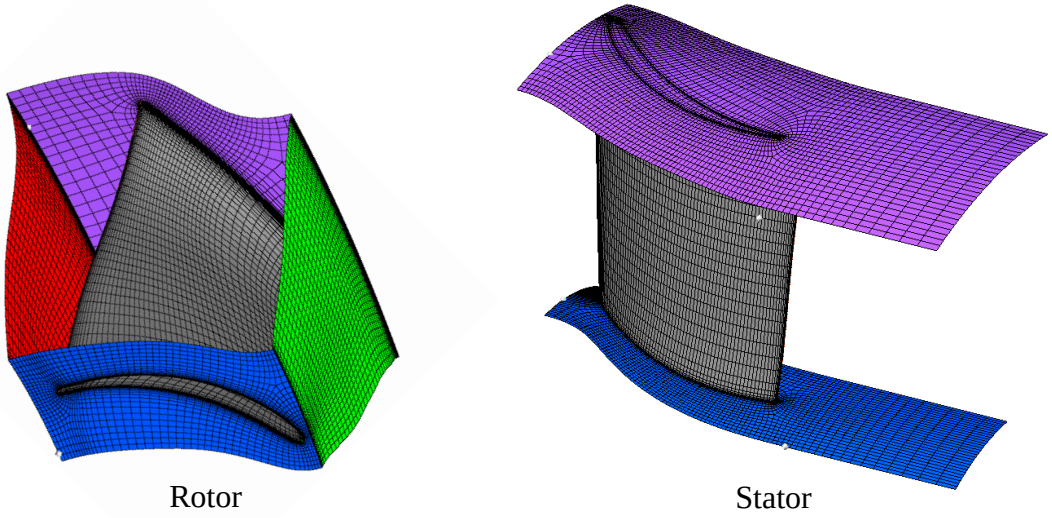

Figure 3.18 Mesh for rotor and stator blade passages

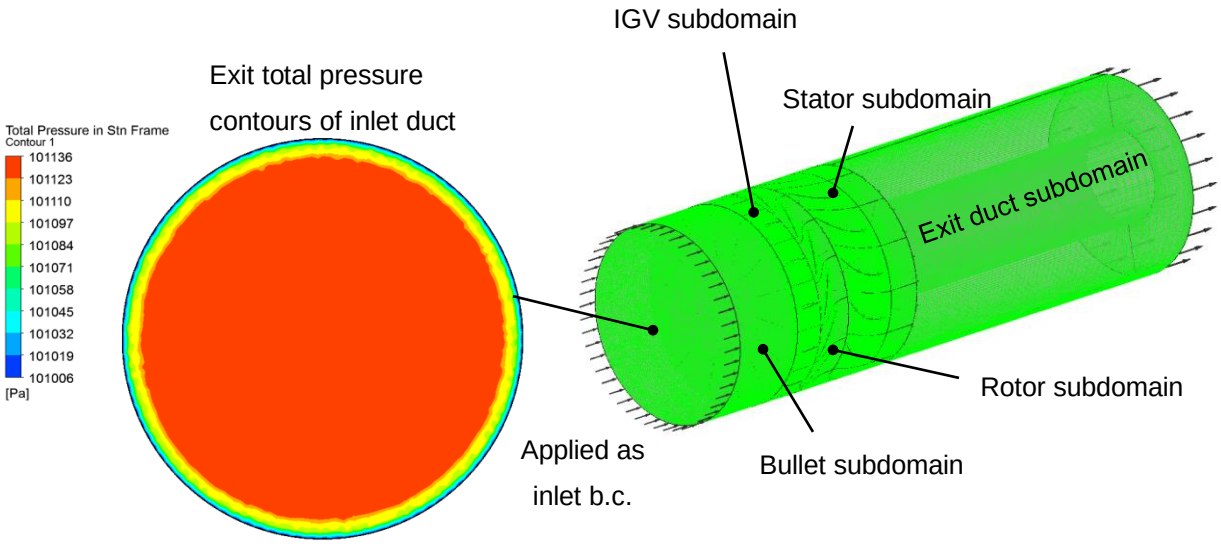

Figure 3.19 Simulation setup for no-distortion case of the test fan

Table 3.6 Simulation parameters for test fan stage

Option settings	Selection	Justification
Analysis type	Steady / unsteady	
Material	Air ideal gas	Compressible gas
Heat transfer	Total energy	Define the temperature at inlet
Inlet boundary condition	Total pressure, static temperature, axial flow	
Inlet total temperature	288.15 K	
Mass and momentum of all blades	No slip wall	Viscous surface
Hub and shroud	No slip wall	Viscous surface
Angular velocity of fan	753.98 rad/s	$V_{tip} = \Omega \times R_{tip}$
Interface between fan inlet and outlet (steady)	Frozen rotor	Required
Interface between fan inlet and outlet (unsteady)	Transient rotor stator	Required
Outlet boundary condition	0.90 kg/s	Fan design parameter
Specified pitch angle	Rotate 360°	
Time-step (unsteady)	2.78×10^{-5} s	The pitch is divided into 20 segments
Simulated time (unsteady)	0.08 s	Approximate convection of slowest particle
Residual	10^{-6}	Experience
Platform MPI local parallel	8	I7 4790 CPU and 128G RAM
Intel MPI distributed parallel in Compute Canada server	32	2 x Intel E5-2683 v4 Broadwell @ 2.1GHz and 125G RAM
Typical convergence time	~ 9 weeks	

To validate the proposed numerical setup, Figure 3.20 through 3.22 compare its predicted total pressure distribution under inlet distortion against corresponding test data in the rig, just upstream of the straight IGVs, at the rotor exit and at the stator exit. The match in total pressure contours just upstream of the IGV in Figure 3.20 indicates that evolution of the inlet distortion pattern through inlet duct well captured by the numerical setup. Figures 3.21 and 3.22 show that the locations of the regions with maximum and minimum total pressure (indicated by circles) are relatively well predicted by the proposed numerical setup.

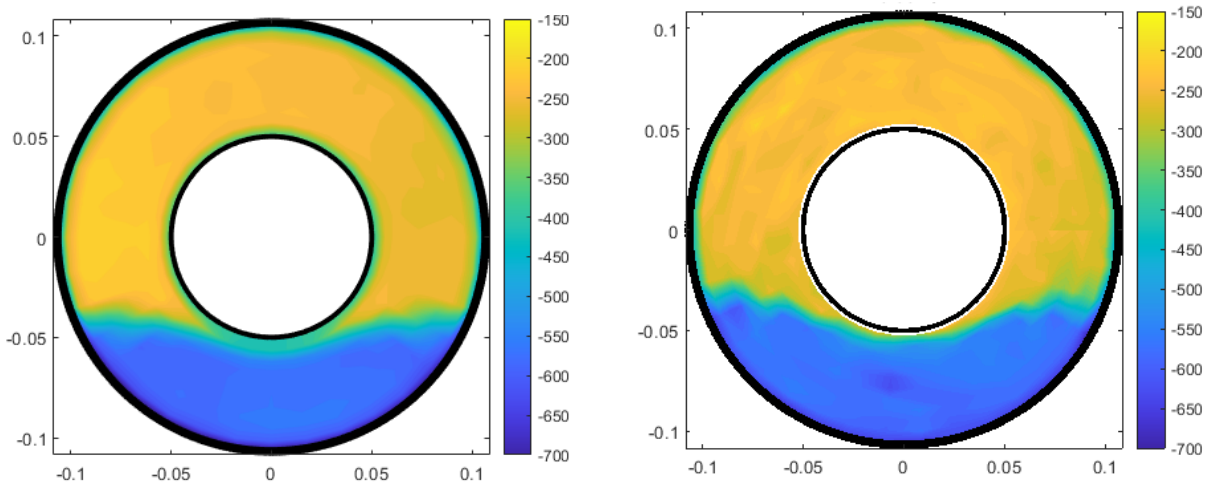

Figure 3.20 Computed (left) and measured (right) total pressure contours just upstream of IGVs

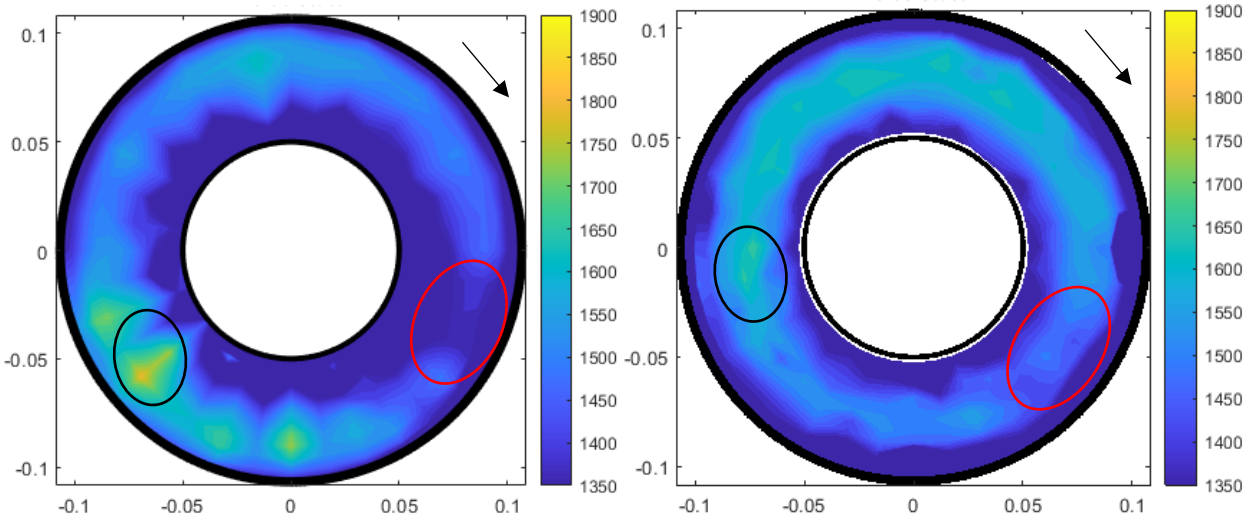

Figure 3.21 Total pressure distribution at rotor exit ($p_{t2} - p_{amb}$) from CFD (left) and measurements (right)

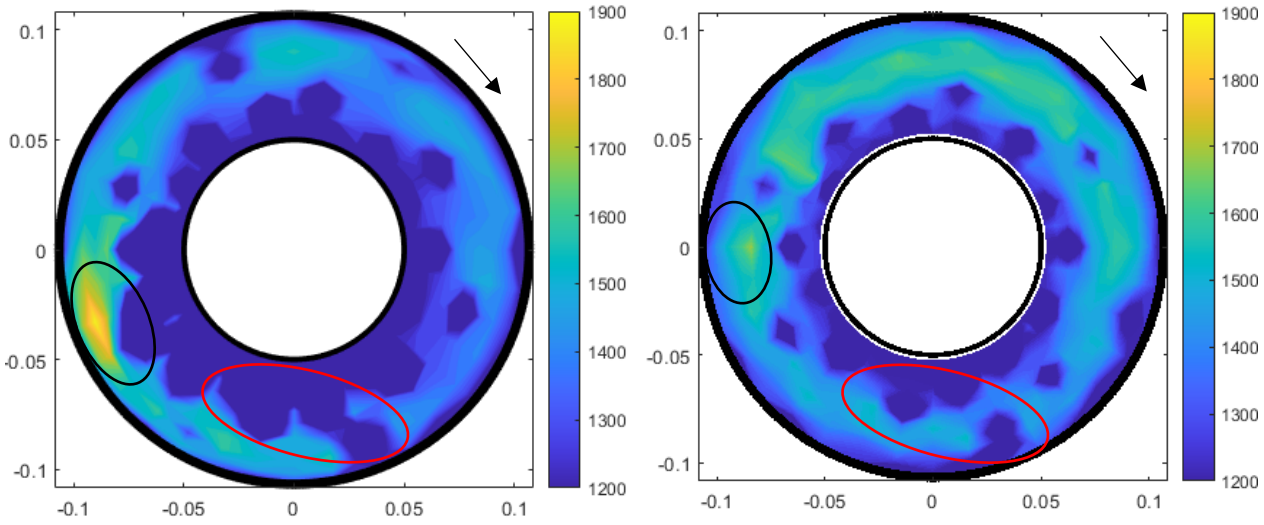

Figure 3.22 Total pressure distribution at stator outlet ($p_{t3} - p_{amb}$) from CFD (left) and measurements (right)

3.3 IGVs Design Procedure

Given the flow redistribution over the fan face in presence of non-uniform inlet flow blockage the design procedure for the asymmetric IGVs are based on CFD simulations to capture the flow redistribution and is iterative in nature. It consists of the following steps:

1) Unsteady CFD simulation of the fan rotor without inlet distortion to calculate the force on the fan blades. This solution represents the reference in terms of blade force, flow field and performance target for the asymmetric IGVs design.

2) Unsteady simulation of fan with inlet distortion to obtain the blade force and axial velocity distribution at rotor LE, from which the asymmetric IGV can be designed.

3) IGVs design based on blade force distribution change due to inlet distortion. The axial velocity contours from Step 2 are input into a *MATLAB* program that uses velocity triangles to set the IGV exit flow angle for each IGV blade such as to bring the local incidence back to the no-distortion value. The IGV is assumed to be an infinitely thin inviscid circular arc with an axial leading edge and a local trailing edge set at the desired local exit flow angle. Only in the case of the test fan stage, the IGVs have viscous surfaces with a NACA65 profile, so as to be later implemented in the rig for test

validation. This exercise is repeated for five span sections (100%, 75%, 50%, 25% and 0% span), with the results imported into CATIA to generate the IGV blades, which are transferred to ANSYD *Mesh* for meshing and incorporation into the fan computational domain. Considering the long simulation times associated with the high-speed fan rotor and the test fan stage, the IGVs design is only carried out at one span (50% span) resulting in 2D IGV blades and a purely circumferential variation in inlet swirl. Moreover, the number of IGV blades should be as low as possible in practice to minimize viscous losses and blockage. In this preliminary assessment, the number of IGV is chosen to be about 20 to ensure adequate flow turning.

4) Perform unsteady simulations with asymmetric IGVs and compare the variation in blade aerodynamic forces with the no-distortion and distortion cases.

5) Since the flow redistribution may have changed in the presence of the IGVs, readjust the design exit angle of IGVs in the same direction with rotor rotation to decrease the blade force and in the opposite to increase the blade force. Repeat steps 4 and 5 until the variation in blade aerodynamic force is acceptably small.

3.4 Analysis

For each of the fan geometries studied, the analysis is carried out in three stages, and Chapters 4 through 6 will present the results in this order. ANSYS CFX-*Post* is used to calculate blade aerodynamic forces and to produce contours of flow properties while their circumferential variations at three different spans (20%, 50% and 80%) are plotted with *MATLAB*. The main axial planes used for flow analysis are the *rotor LE* plane, located just upstream of the actual rotor leading edge, and the *rotor TE* plane located just downstream of the actual rotor trailing edge. In both cases, these planes lie inside the rotor subdomain. For the low-speed test fan stage, an additional analysis plane is considered for stage performance calculation, namely the *stator TE* plane located downstream of the stator trailing edge. Figures 3.23 through 3.25 show the locations of these analysis planes relative to the blade rows and interfaces in the meridional view of the computational turbomachinery subdomains for each of the three geometries studied.

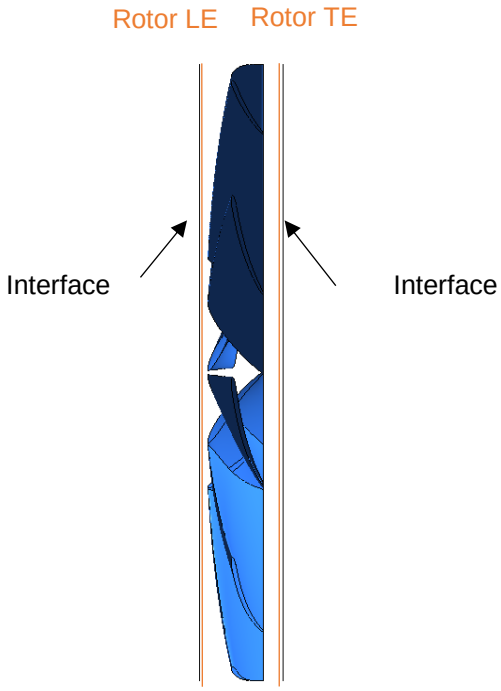

Figure 3.23 Analysis planes for low-speed fan rotor

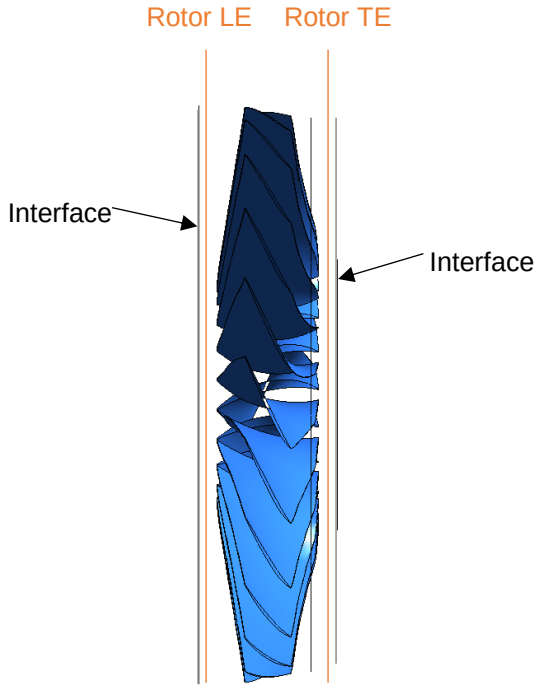

Figure 3.24 Analysis planes for high-speed fan rotor

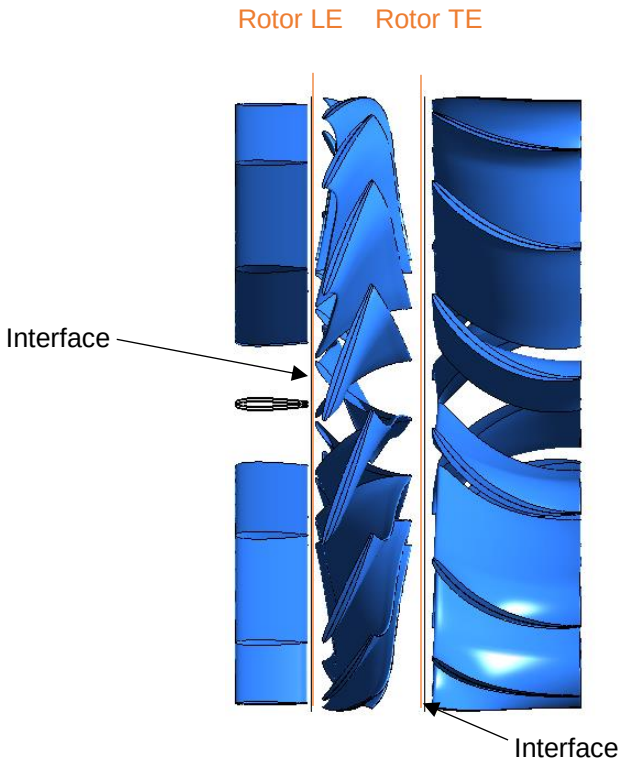

Figure 3.25 Analysis planes for low-speed test fan stage

The first stage of the analysis looks at the effect on inlet distortion on the fan at the rotor inlet, rotor exit and on the blade force through a comparison of the no-distortion versus with-distortion cases. First, plots of the distributions at the rotor LE plane of total pressure, static pressure, axial velocity, circumferential velocity, swirl angle and rotor relative inlet velocity and flow angle are produced to assess the change in rotor inlet flow properties and flow redistribution due to inlet distortion. Thereafter, a plot of the blade aerodynamic force distribution for the two cases is produced to see the loading non-uniformity caused by the inlet distortion in preparation for the asymmetric IGVs design. Lastly, the distributions of total pressure at the rotor LE and TE planes are compared between the two cases to evaluate the amplification of the total pressure distortion pattern across the rotor.

The second stage of the analysis shows the most recent IGVs design iteration and assesses its effect on blade force distribution through a plot of the blade aerodynamic force distribution along the circumference for the three cases: no distortion, with distortion and with IGVs. This is

followed by a plot of the circumferential variation of blade loading at the three spans studied (20%, 50% and 80%) to see the effectiveness (or lack thereof) of the asymmetric IGVs near the hub, at mid-span and near the tip. This can provide clues for improvement in the IGVs design. It is noted that the blade loading is *not* the force on a blade. Rather, it is a *local* force per unit area obtained from a control volume analysis using the inlet and exit flow conditions from the CFD data taken at one particular span and circumferential location. The details and equations for the control volume analysis are provided in Appendix A (Section A.2).

The third stage of the analysis considers the effect of the asymmetric IGVs on the flow field under inlet distortion. It starts with comparison of the circumferential variation at different spans of relative inlet flow angle (a change in this parameter represents a change in incidence) and relative velocity for the cases with and without IGVs. The distributions of the total pressure at the rotor exit are then compared for the two cases to evaluate the effectiveness of the IGVs in attenuating the total pressure distortion.

The last analysis evaluates the effect of the asymmetric IGVs on integral fan performance in comparison to the no-distortion and with distortion case. Only total pressure ratio is considered since efficiency is not relevant given the inviscid simulations for two of the three fan geometries. Since the total pressure distribution at the rotor leading edge changes with flow redistribution in the presence of distortion and asymmetric IGVs, the total pressure ratio is defined as the mass-averaged total pressure at rotor TE plane over undistorted inlet total pressure for a fair comparison between all different cases. The viscosity of the IGVs are also not considered in this study, except for the low-speed test fan stage. The definitions used to calculate some of the output parameters are defined in Appendix A (Section A.1).

CHAPTER 4 LOW-SPEED FAN ROTOR RESULTS

This chapter presents the results for the low-speed fan rotor. It will start with an assessment of the effect of inlet distortion on the fan rotor. A description of the latest/best asymmetric IGVs design iteration is then given, followed by an assessment of its effects on aerodynamic blade force, fan rotor inlet/exit flow fields and fan performance. The contour plots are shown for an observer looking downstream with the rotor turning in the clockwise direction.

4.1 Effect of Inlet Distortion

4.1.1 Rotor Inlet Conditions

Figure 4.1 shows the total pressure distribution (relative to the uniform inlet pressure with no distortion) at the computational domain inlet for the low-speed fan rotor. The deepest distortion, the lowest total pressure, is in the outer spans in the annular sector between 220º and 320º. The left edge of the distortion annular sector (220º) where the rotor enters the distortion region is henceforth referred to as the *distortion region LE*, while its right edge (where the rotor leaves the distortion region) is called the *distortion region TE*. Figure 4.2 shows the same contours at the rotor LE plane, while Figure 4.3 plots the contours of axial velocity (non-dimensionalized by rotor tip circumferential velocity) at this plane. One can immediately notice the circumferential ondulations in the total pressure and axial velocity at the rotor LE plane. This is due to the potential effect of the fan rotor blades already being felt and inducing flow turning (hence work and total pressure change) just upstream of the actual rotor leading edge. The background trend behind the ondulations on Figures 4.2 and 4.3 show a reduction in the (mean) total pressure and axial velocity in the distortion region and an increase in axial velocity in the opposite (undistorted) region. This observation can better be seen on Figure 4.4, which compares the circumferential variation of axial velocity at three spans between the no-distortion and with distortion cases to show the largest axial velocity deficiency occurring at the outer span in the middle of the distortion annular sector, as well as higher axial velocity over the opposite half-annulus at all spans. This is a clear illustration of (global) flow redistribution from the distorted (blockage) region to the undistorted region.

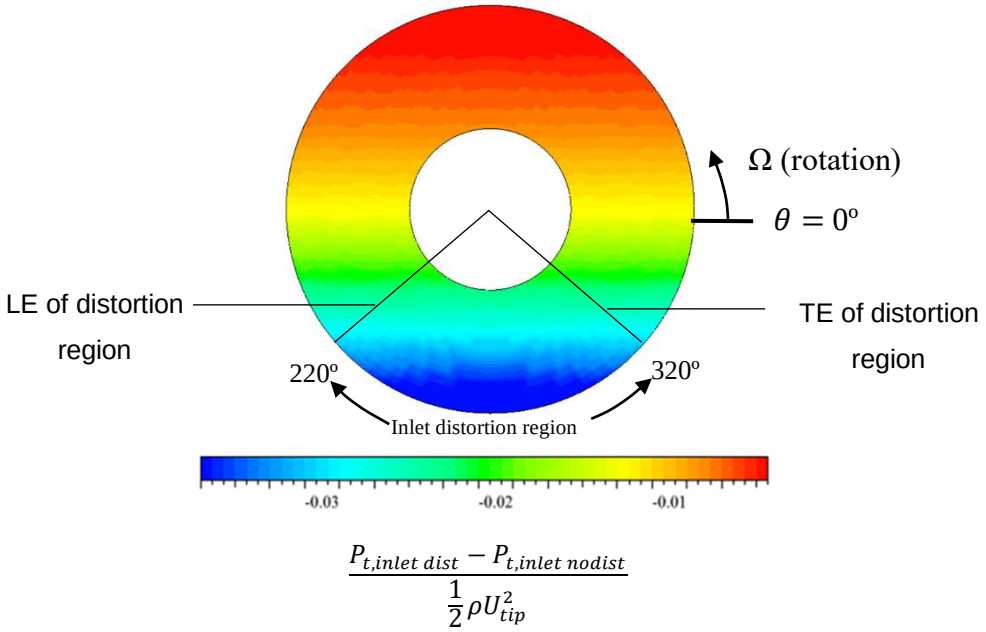

Figure 4.1 Total pressure distribution at low-speed fan domain inlet plane

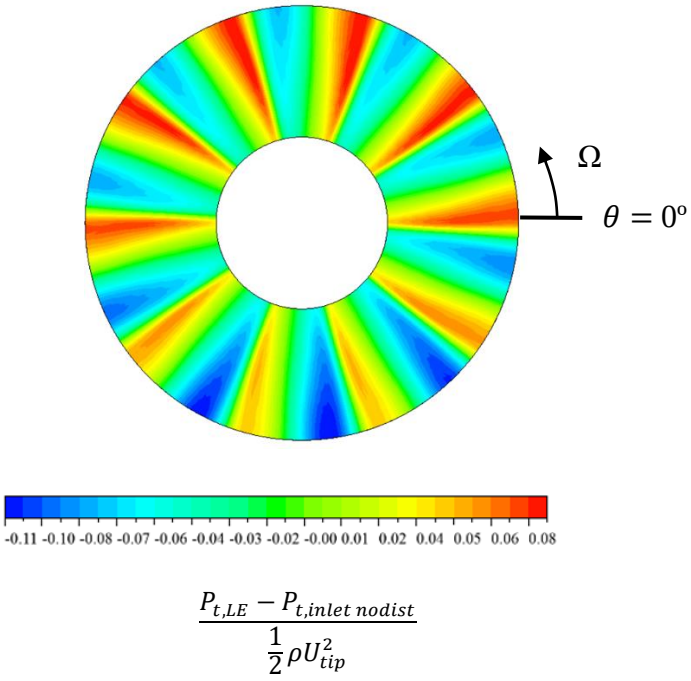

Figure 4.2 Total pressure distribution at low-speed fan rotor LE plane

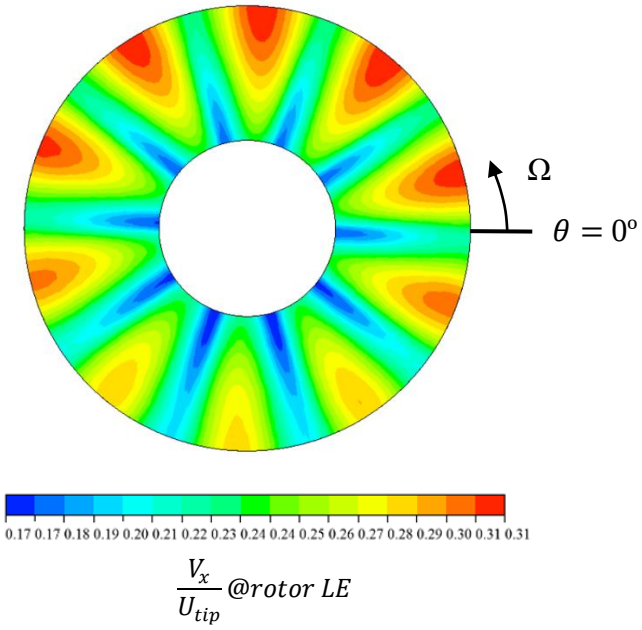

Figure 4.3 Effect of inlet distortion on axial velocity at low-speed fan rotor LE plane

In addition, there is also a local flow distribution in the reversed direction at the edge of the distortion sector that circumferentially shifts the blade aerodynamic force distribution from those of the inlet total pressure and axial velocity. This phenomenon is driven by the static pressure being lower in the distortion region that causes the flow on either side of the distortion annular sector to flow into the sector, as illustrated in Figure 4.5. The result is an induced positive swirl (in direction of rotor rotation, or *co-swirl*) on the distortion region LE and a negative swirl (in opposite rotor rotation, or *counter-swirl*) on the distortion region TE, as shown in Figure 4.6. The corresponding velocity triangles in Figure 4.7 shows that this local flow redistribution translates to lower rotor incidence and inlet relative velocity on the distortion region LE and the opposite effects on the distortion region TE. This is confirmed by the distributions of relative flow angle and relative velocity at the rotor LE plane in Figures 4.8 and 4.9, respectively, which show that the circumferential location of maximum relative inlet flow incidence angle and relative velocity is not at the center of the distortion region (270°) but shifted toward the distortion region TE. It is noted that an increase in incidence and relative inlet velocity increases blade (aerodynamic) force, while a decrease in these parameters leads to the opposite effect. Therefore, this circumferential shift is expected to affect the blade force distribution as well as the flow field downstream of the rotor and will be verified in Sections 4.1.2 and 4.1.3.

$\frac{V_x}{U_{tip}}@rotor\ LE$

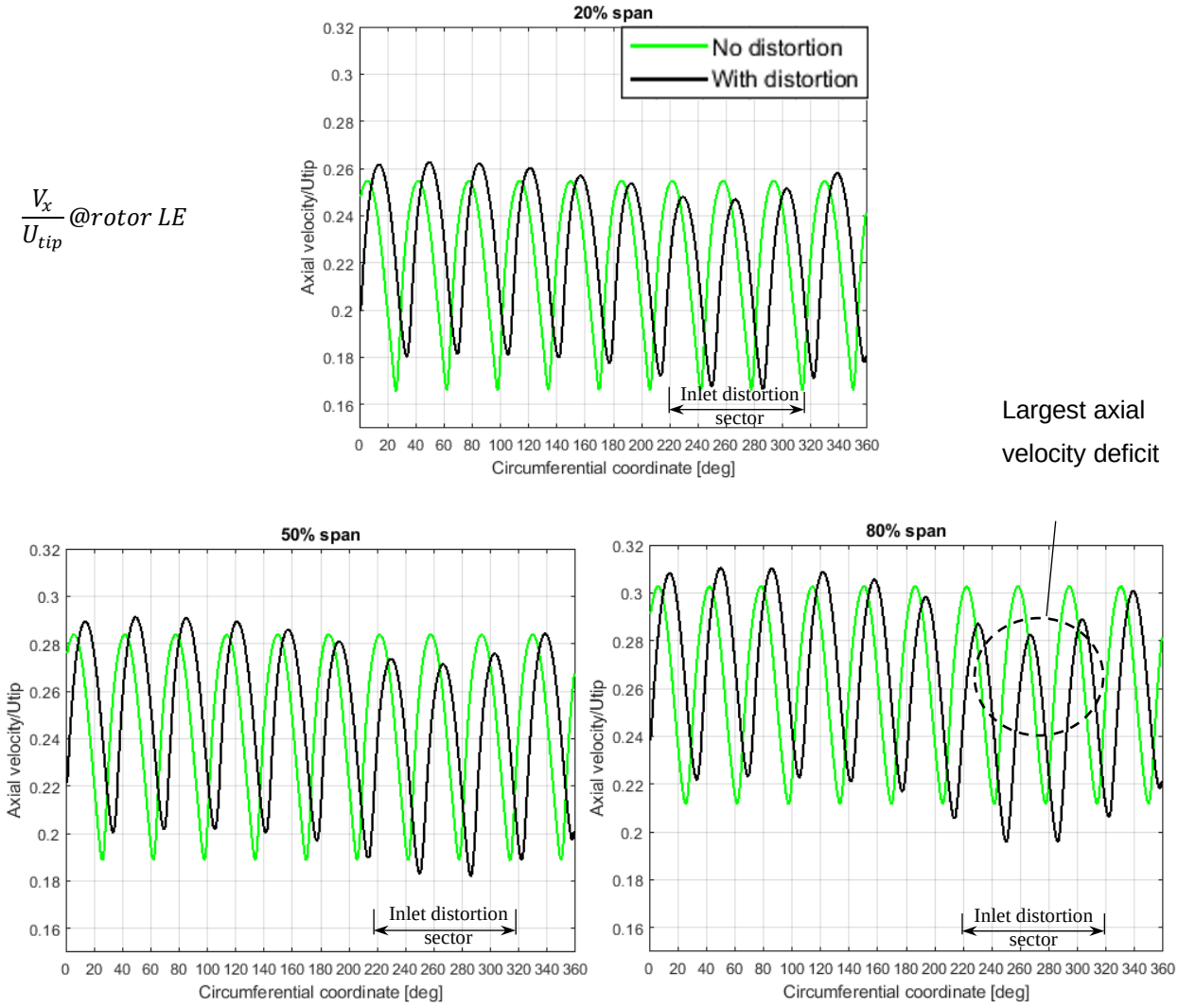

Figure 4.4 Effect of inlet distortion on axial velocity at low-speed fan rotor LE

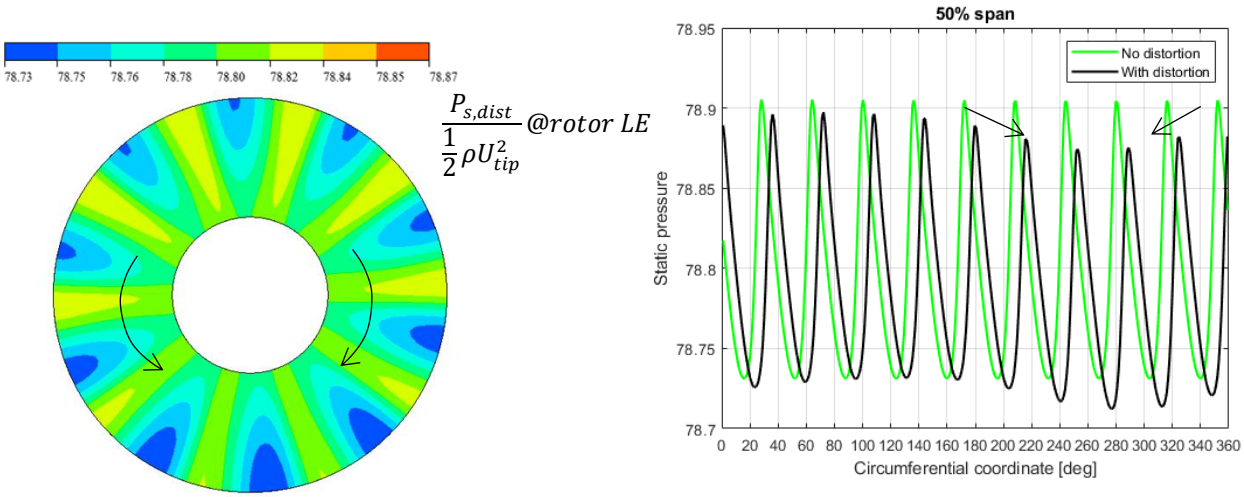

Figure 4.5 Effect of inlet distortion on static pressure distribution at low-speed fan rotor LE plane

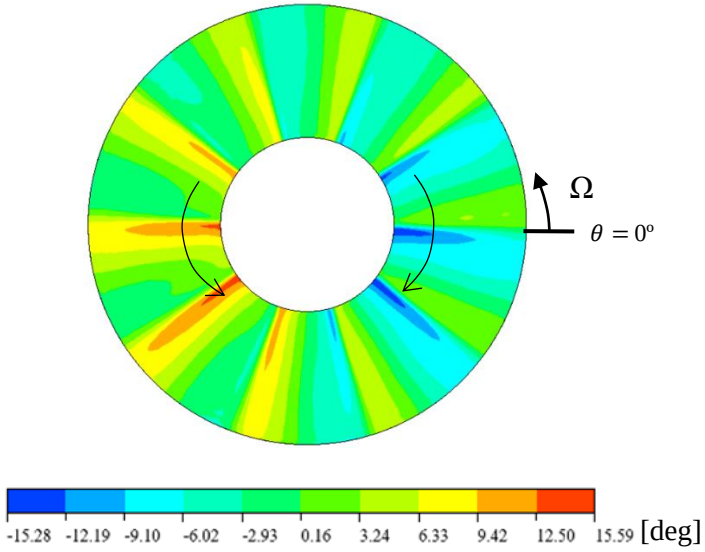

Figure 4.6 Effect of inlet distortion on absolute flow angle at low-speed fan rotor LE plane

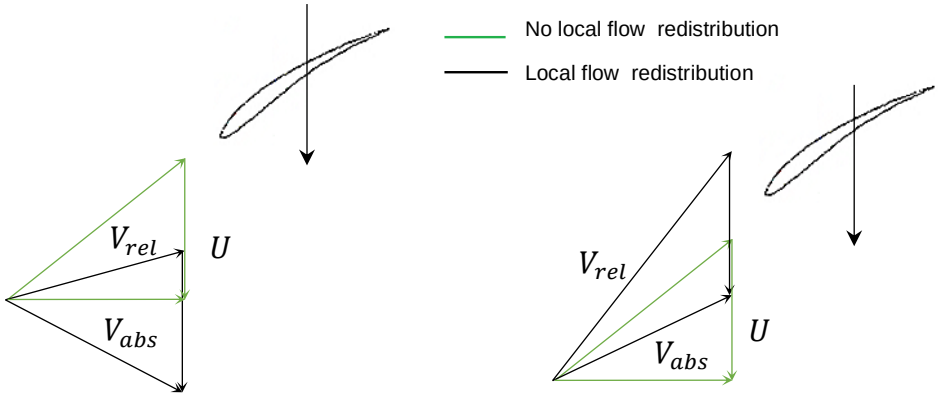

(a) Distortion region LE (b) Distortion region TE

Figure 4.7 Velocity triangles at distortion region LE and TE

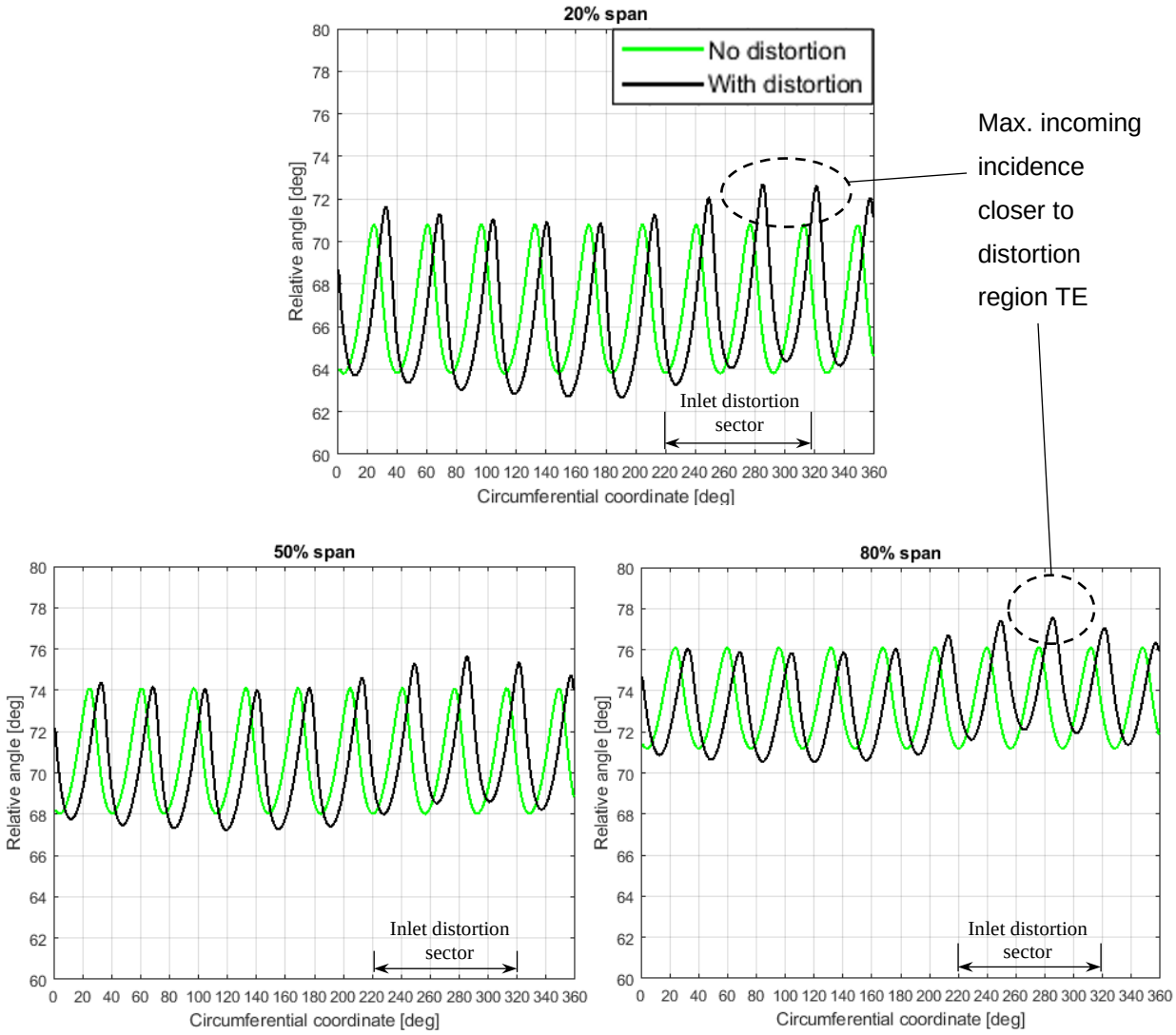

Figure 4.8 Effect on inlet distortion on relative flow angle at low-speed fan rotor LE plane

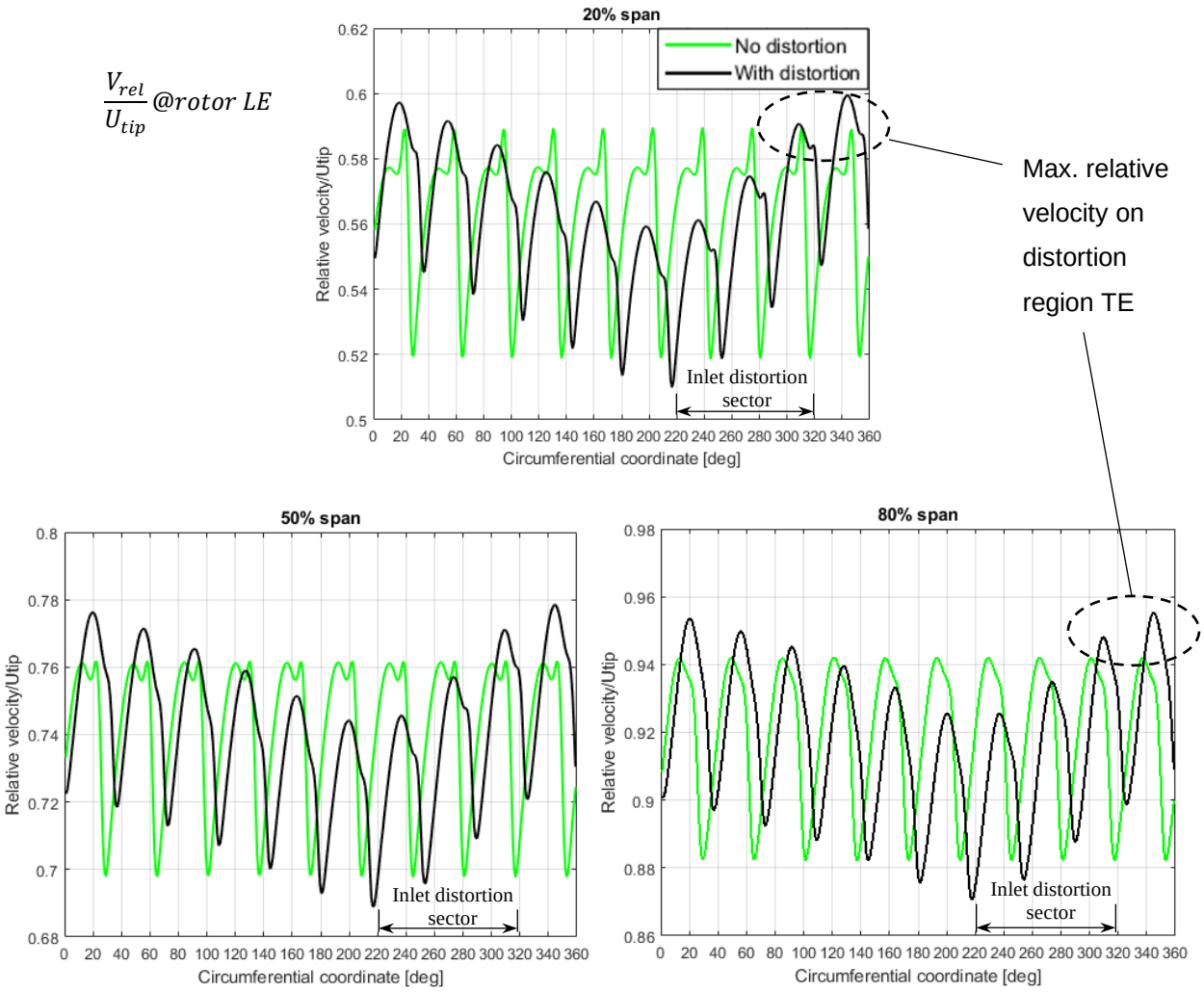

Figure 4.9 Effect of inlet distortion on relative flow velocity at low-speed fan rotor LE plane

4.1.2 Blade Force

Figure 4.10 compares the variation in blade aerodynamic force for the low-speed fan rotor with distortion to the reference no-distortion case. The fan under distortion is subjected to a variation of blade (aerodynamic) force from 149.1 N to 159.4 N, or of 7% or nominal (no-distortion) value. The blade force of fan with inlet distortion is lower than that without distortion in the range of 40º to 230º, and higher at other angular locations. As predicted by the circumferential shift in the maxima of relative inlet flow angle and velocity in Figures 4.8 and 4.9 due to local flow redistribution at the edge of the distortion region, the maximum blade force is shifted toward the

distortion region TE, seemingly more influenced by the (larger) circumferential shift of the relative velocity than that of the relative flow angle.

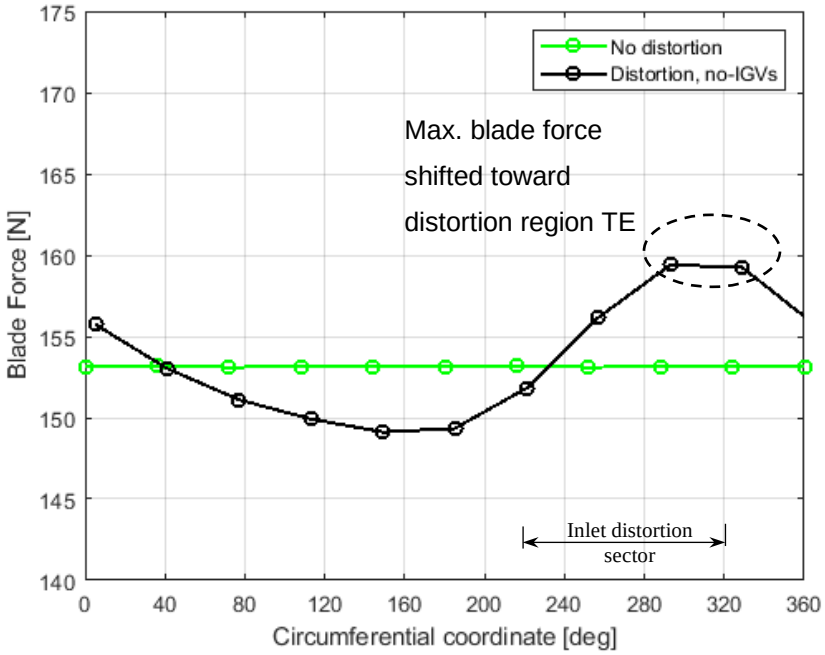

Figure 4.10 Effect of distortion on blade force for low-speed fan rotor

4.1.3 Rotor Outlet Conditions

Figure 4.11 presents the circumferential distribution of (non-dimensionalized) total pressure for the no-distortion versus with-distortion cases at the rotor LE and rotor TE planes. The amplitude of total pressure distortion does not change significantly across the rotor because of the low rotation speed. One can observe that the background trend of the circumferential total pressure variation (*i.e.* discounting the ondulations due to the discrete blades) follows that of the blade force in Figure 4.10, as can be expected since total pressure rise correlates with blade (aerodynamic) force increase. As such, the annular sector between 40º to 230º will see lower total pressure rise due to lower blade force than the no-distortion case. Moreover, the sector (180º-220º) near the distortion region LE combines low blade force (due to local flow redistribution as

explained previously) with low rotor LE total pressure (due to inlet distortion) resulting in the lowest TE total pressure.

$$\frac{P_T}{\frac{1}{2}\rho U_{tip}^2} @rotor\ LE\ \&\ TE$$

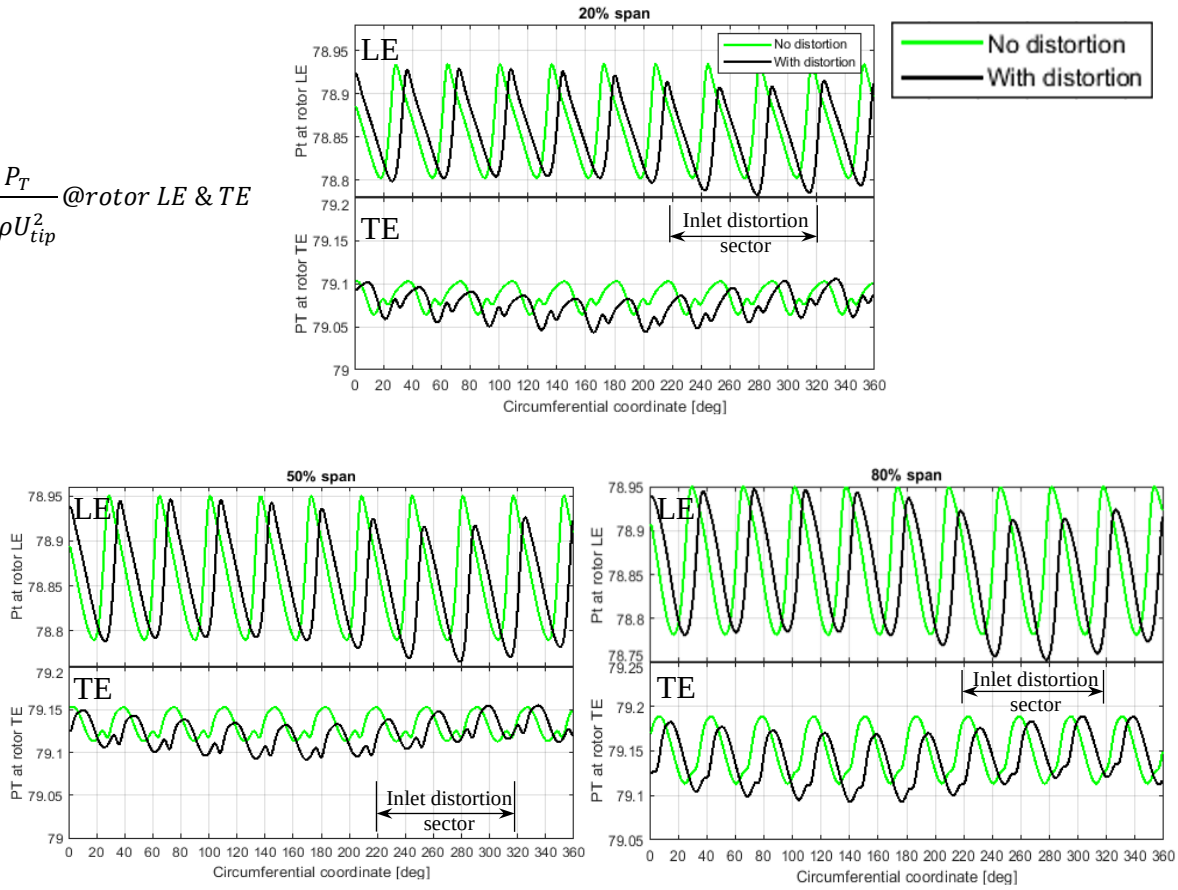

Figure 4.11 Effect of inlet distortion on evolution of total pressure from LE to TE planes of low-speed fan rotor

4.2 Asymmetric IGVs Design

Figure 4.12 shows the trailing edge angle distribution of the asymmetric IGVs after three design iterations. The asymmetric IGVs exit angle distributions for all three design iterations can be found in Appendix B (Section B.1). For this preliminary assessment, the IGVs are infinitely thin and inviscid with a circular arc profile. A positive IGV exit angle induces counter-swirl (swirl in direction against fan rotation) to increase incidence and blade loading, while a negative IGV exit angle induces co-swirl and decreases incidence and blade loading. Based on Figure 4.10, the positive IGV exit angles are applied in the 40º-230º annular sector to increase blade loading

while negative IGV exit angles are applied in the remaining sector where blade loading under distortion is higher than the no-distortion case.

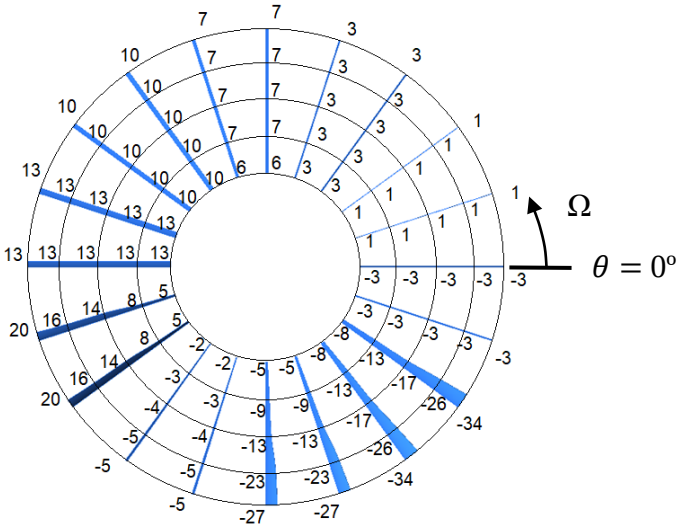

Figure 4.12 Asymmetric IGV trailing edge angles for low-speed fan rotor

4.3 Blade Force Assessment

4.3.1 Integral Blade Force

Figure 4.13 shows the effect of the asymmetric IGVs of Figure 4.12 by comparing the circumferential variation of aerodynamic blade force for this case versus those with distortion but no IGV and without distortion. The asymmetric IGVs reduce the variation amplitude of blade force under distortion (from 10.3 N to 3.3 N). Given this asymmetric IGVs design is obtained based on only a few manual iterations and not yet optimized, an optimized version will likely achieve even better results, bringing the blade loading variation even closer to the no-distortion case.

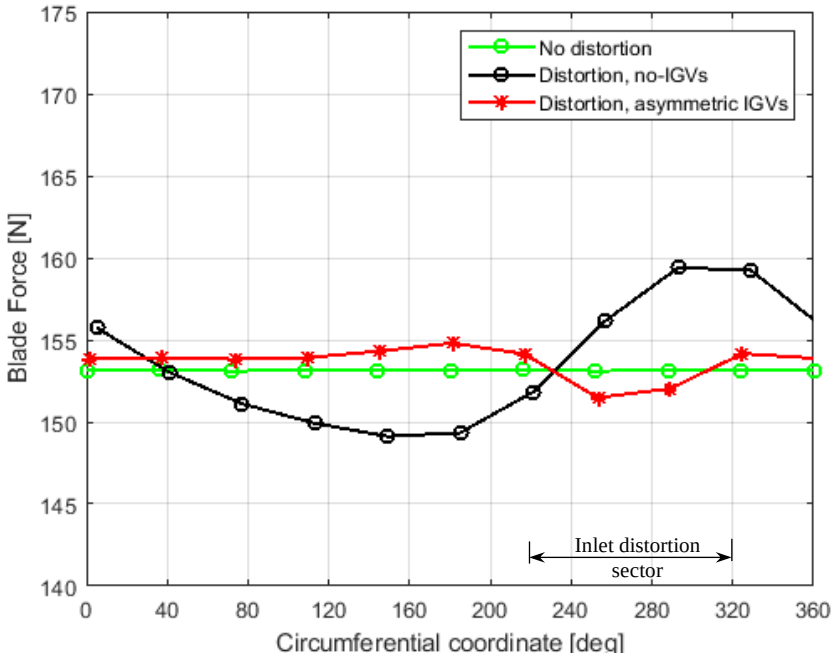

Figure 4.13 Effect of asymmetric IGVs on low-speed fan rotor blade force variation

4.3.2 Spanwise Blade Loading

Figure 4.14 plots the circumferential distribution of blade loading (force per unit area) at 20%, 50% and 80% span under distortion with and without IGVs, as obtained from a control volume analysis using CFD data in Appendix B (Section B.3). The results indicate that the blade loading non-uniformity is reduced at the two outer span (50% and 80%). However, the data also suggests that this IGVs design is far from optimal at the lower spans. The blade loading increase at 20% span is higher than needed across the entire annulus but is also more non-uniform than without IGVs due to excessively high loading increase outside the inlet distortion annular sector. Moreover, the overshoot in blade loading due to the IGVs in the inlet distortion sector effectively forces the IGVs to overturn (excessive co-swirl) to reduce loading at the outer spans to compensate. To improve the IGVs design, the IGVs trailing edge should be turned more in the rotor rotation direction flow angle outside of the 220º-320º sector for the outer spans. This should also be done for the inner span across the entire annulus but with higher co-swirl outside of the 220º-320º to attenuate the excessive loading increase. These design modification should help make the loading more uniform at all spans and bring the blade force with IGVs even closer to the no-distortion case in Figure 4.13.

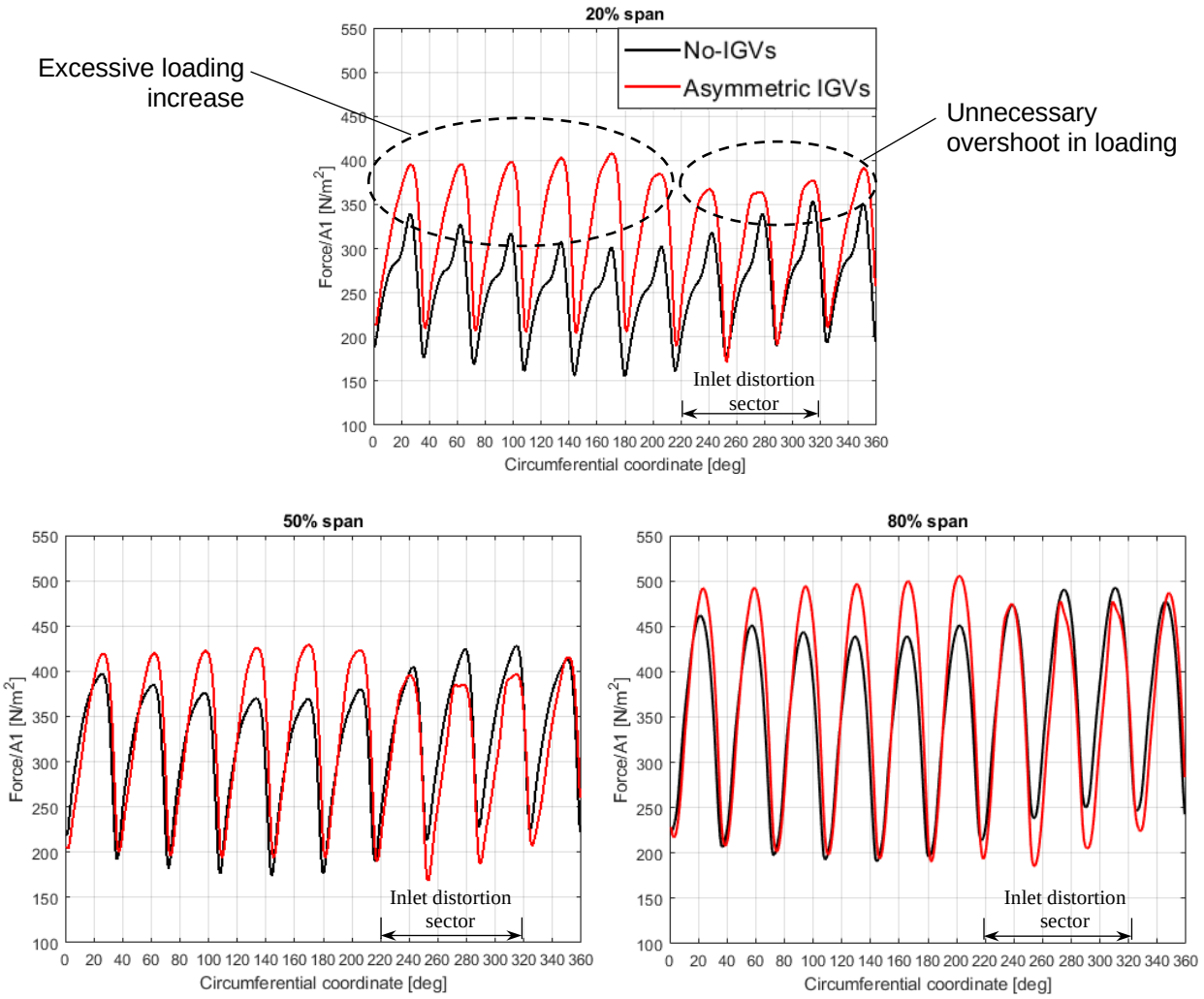

Figure 4.14 Circumferential variation of blade loading at different spans for low-speed fan rotor

4.4 Flow Field Analysis

This section presents the effect of the asymmetric IGVs design on the flow to try to explain the effect on the asymmetric IGVs on the blade force variation seen in Figure 4.13 and to provide means to further improve the IGVs design, as well as to assess its effect, if any, on attenuating the total pressure distortion in the rotor exit flow field.

4.4.1 Effect of IGVs on Rotor Inlet Flow

Figure 4.15 shows the effect on the asymmetric IGVs on the relative velocity and flow angle at the rotor LE plane. The data indicates that the IGVs increase the relative inlet velocity and flow angle in the annular sector 40º-230º at all three spans to provide the increase in lift seen in Figure

4.13 for this sector. The increase is more dramatic, especially for the relative velocity, in the 120º-220º sector where the force deficit under distortion is the most pronounced. Inversely, the IGVs decrease the rotor inlet relative velocity and flow angle in most of the high blade force annular sector (slightly offset from the inlet distortion region due to local flow redistribution) to reduce blade force as intended. In addition, in the annular sectors with the largest IGV exit angle magnitude in Figure 4.12 (160º-220º and 270º-330º), the change in local relative velocity is more dramatic than that of the relative flow angle. This is a result of flow redistribution in presence of the IGVs, as can be seen in the effect of IGVs on the axial velocity distribution in Appendix B (Section B.3).

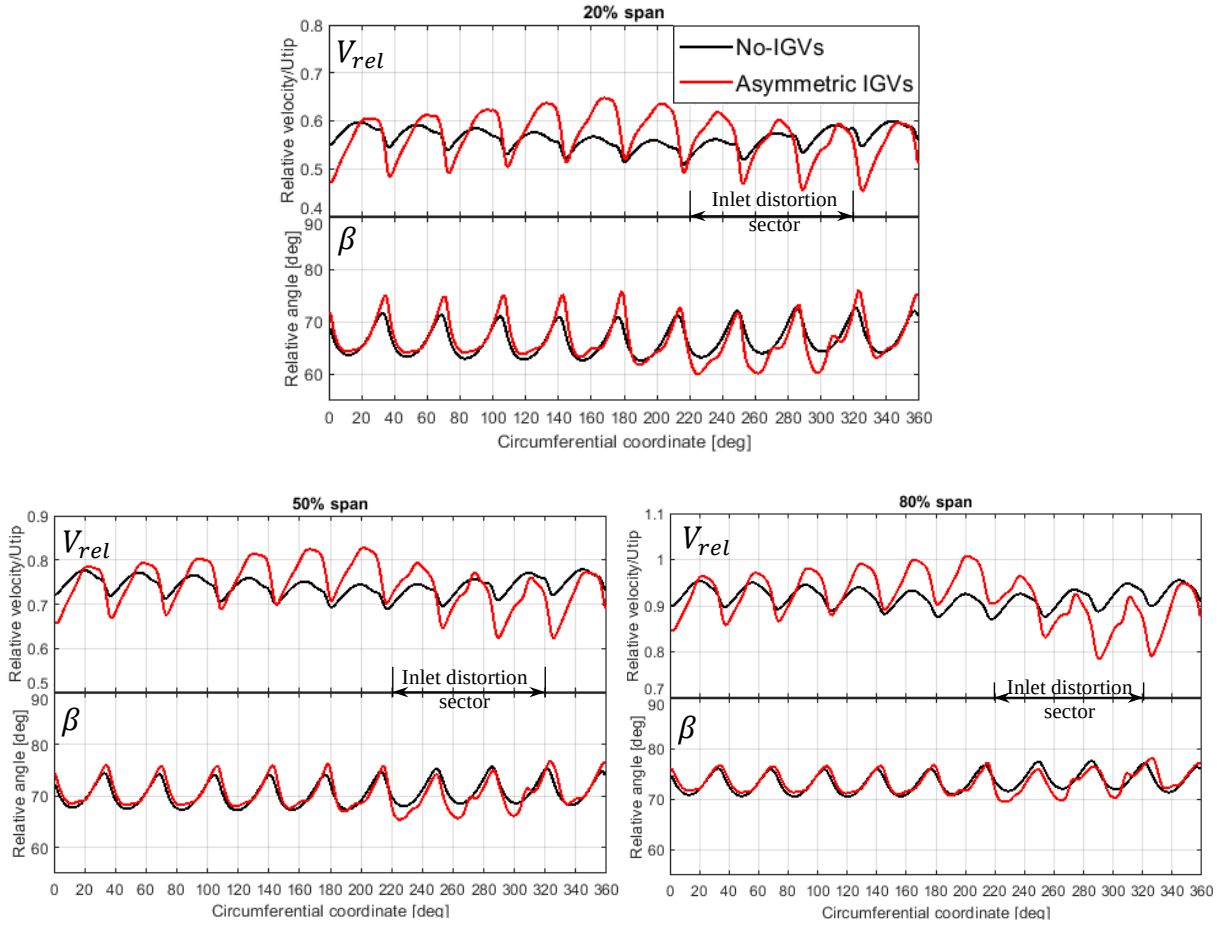

Figure 4.15 Circumferential variation of relative velocity and relative flow angle at low-speed rotor LE for different spans

4.4.2 Effect of IGVs on Rotor Exit Flow

Figure 4.16 compares the non-dimensionalized total pressure contours at the rotor TE plane for the no-distortion case to those for the distortion cases with and without IGVs. One immediately observes that implementation of this asymmetric IGVs design does not attenuate the total pressure circumferential non-uniformity at the rotor exit but makes it slightly worse especially near the hub and the tip.

For a more quantitative assessment, Figure 4.17 compares the same parameter at the 20%, 50% and 80% span for the distortion cases with and without IGVs. The data show than the circumferential non-uniformity is worse with IGVs at all three spans, but more so at 20% span. This observation correlates with the blade loading distribution in Figure 4.14, which shows excessive and more non-uniform blade loading at 20% span due to the IGVs that is also reflected in the rotor exit total pressure distribution at this span. As such, the IGVs design corrections to improve loading uniformity suggested in Section 4.3.2 should also improve the rotor exit total pressure uniformity with IGVs and perhaps even beyond the no-IGV case.

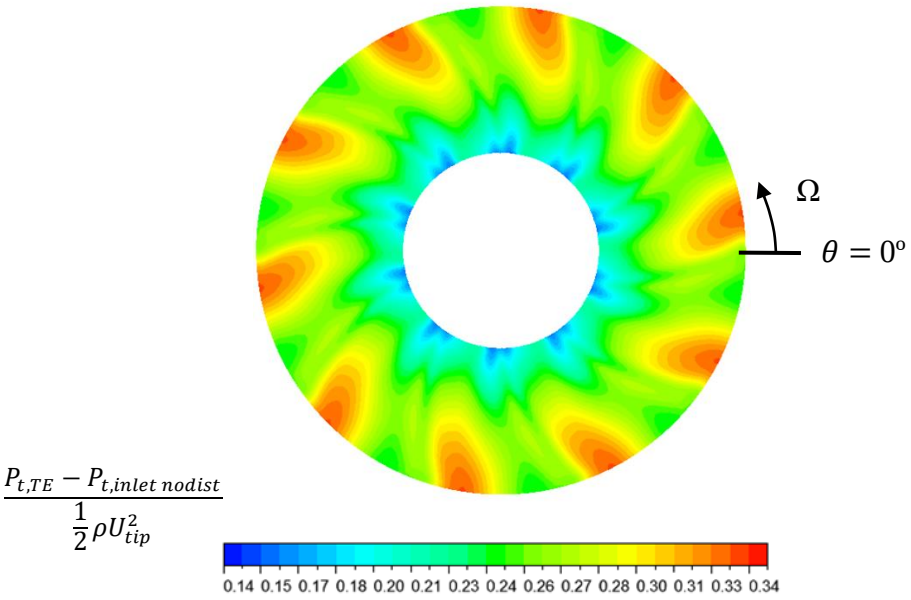

(a) No inlet distortion

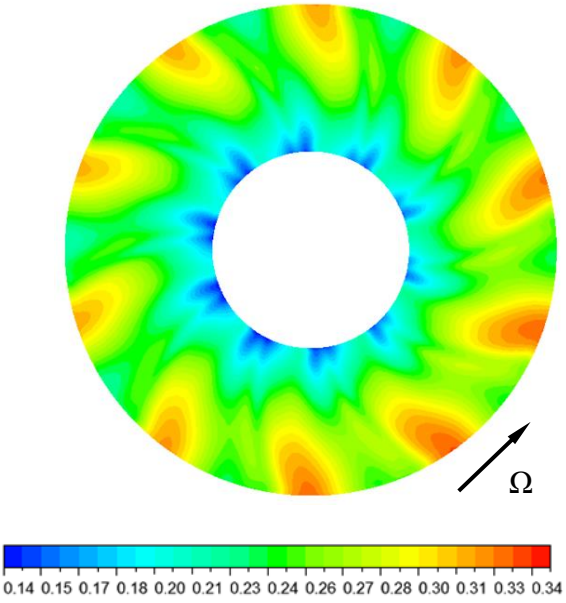

(b) Inlet distortion, without IGVs

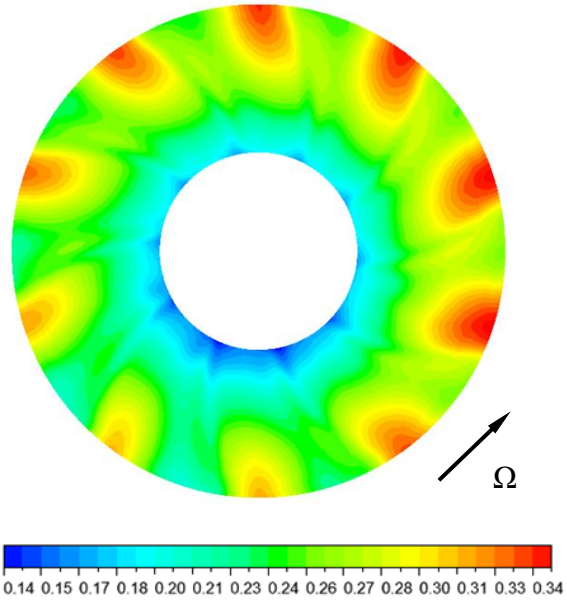

(c) Inlet distortion, with IGVs

Figure 4.16 Total pressure contours at low-speed fan rotor TE plane

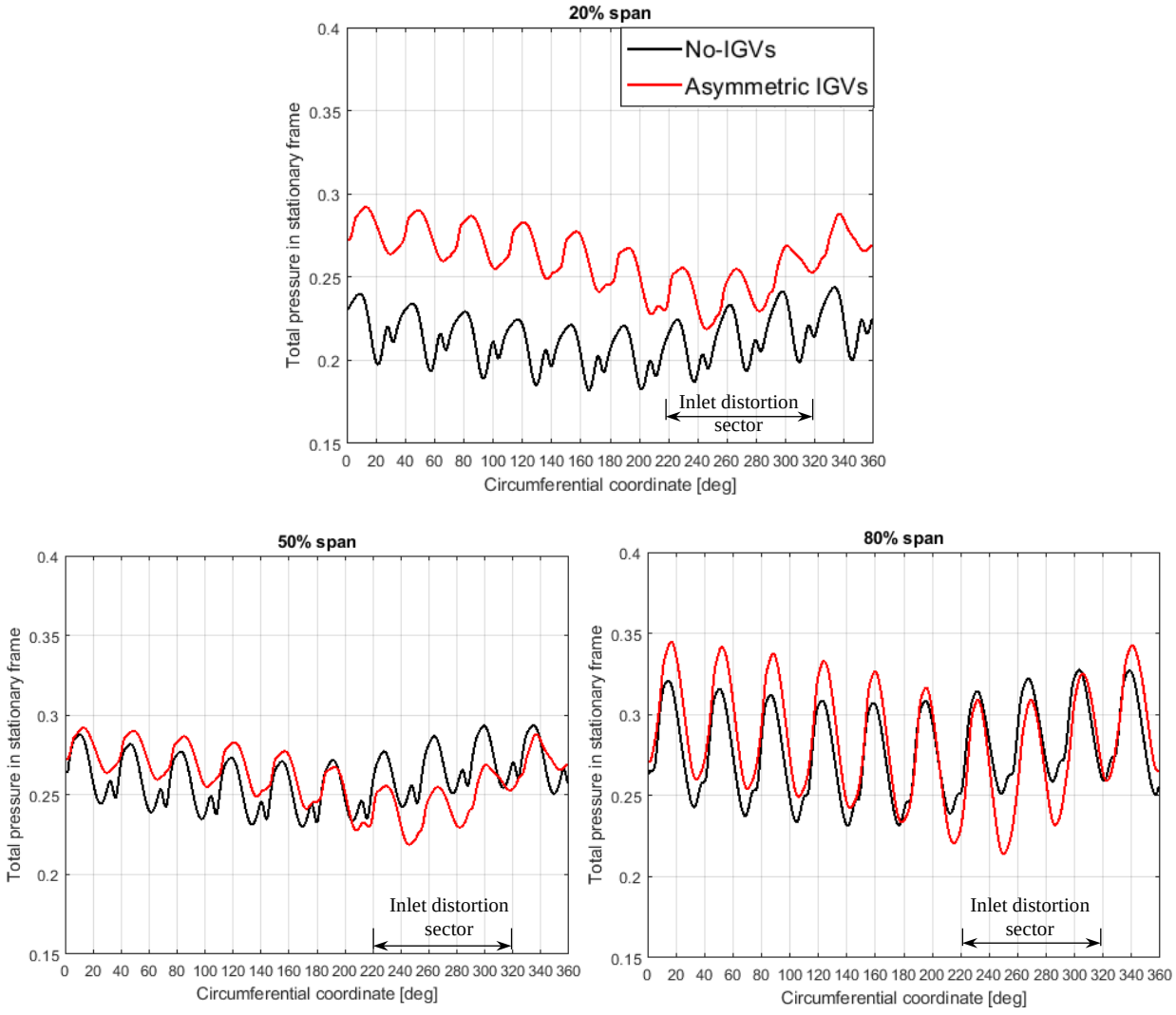

$$\frac{P_{t,TE} - P_{t,inlet\ nodist}}{\frac{1}{2}\rho U_{tip}^2}$$

Figure 4.17 Circumferential variation of total pressure at low-speed fan rotor TE for different spans

4.5 Effect on Fan Performance

Table 4.1 presents the total pressure ratio of the low-speed fan rotor for the cases without distortion and under inlet distortion with and without asymmetric IGVs. In addition to attenuating blade force variation, the results indicate that this non-optimized asymmetric IGVs design helps to recover almost half of the drop in total pressure rise due to inlet distortion. While a better IGVs

design may improve this pressure ratio recovery, the viscous losses in actual IGVs may at least partially cancel it.

Table 4.1 Effect of distortion and asymmetric IGVs of low-speed fan rotor

	No distortion	Distortion without IGVs	Distortion with Inviscid IGVs
Total pressure ratio	1.00341	1.00329	1.00334

4.6 Discussion

The results presented in this chapter show that the asymmetric IGVs can significantly reduce the blade force variation and loss in fan total pressure rise due to modest inlet distortion in a low-speed fan by decreasing incidence and relative velocity over much of the distortion region to reduce blade force and the opposite elsewhere to increase blade force, as intended. While this IGVs design iteration did not improve the total pressure distortion at the rotor exit, local blade loading analysis indicates that a better 3D design of the asymmetric IGVs can resolve this problem as well as further reduce the blade force variation and loss in fan total pressure rise. The next chapter will verify whether this concept can work on a realistic transonic fan with more severe inlet distortion.

CHAPTER 5 HIGH-SPEED FAN RESULTS

This chapter presents the results for the high-speed fan rotor (NASA Rotor 67). As in Chapter 4, the effect of inlet distortion on the fan rotor is assessed first. Thereafter, the latest asymmetric IGVs design iteration is described and its effects on aerodynamic blade force and fan rotor inlet/exit flow fields and performance are assessed. Again, the contour plots are shown for an observer looking downstream with the rotor turning in the clockwise direction.

5.1 Effect of Inlet Distortion

5.1.1 Rotor Inlet Conditions

Figure 5.1 shows the total pressure distribution (relative to the uniform inlet total pressure with no distortion) at the computational domain inlet for the high-speed rotor. The distortion covers exactly one third of the inlet domain, in the annular sector between 210º and 330º. Figures 5.2 and 5.3 show the contours of non-dimensional total pressure and axial velocity, respectively, at the rotor LE plane. Similar to observation for the low-speed fan rotor in Chapter 4, Figures 5.2 and 5.3 point to a general flow redistribution, with low axial velocity in the distortion region at the bottom and higher axial velocity in the opposite (undistorted) region.

However, a closer inspection of Figure 5.3 indicates that the highest axial velocity actually occurs at the distortion region TE while the lowest axial velocity is on the distortion region LE. This observation is confirmed by the plots the circumferential variation of axial velocity at three spans in Figure 5.4. As discussed in Section 4.1.1 for the low-speed fan rotor, this is the result of local flow distribution (flow deviation into the distortion region) at the distortion region LE and TE driven by the lower static pressure in the distortion region as shown in Figure 5.5. However, in this case, the flow deviation is much larger than that seen for the low-speed fan rotor in Chapter 4, as evidenced by the absolute (swirl) angle distribution at the rotor LE plane in Figure 5.7 showing the induced swirl angle up to ± 25° at the edge of the distortion region. The large change in axial flow and swirl angle relative to the no-distortion case in these two regions results in a gradient in incidence angle and a relative velocity at the rotor LE across the distortion annular sector that is several times larger than that seen in the low-speed fan, as evidenced by comparing

Figures 5.7 and 5.8 to Figures 4.8 and 4.9, which will have a great influence on blade force distribution.

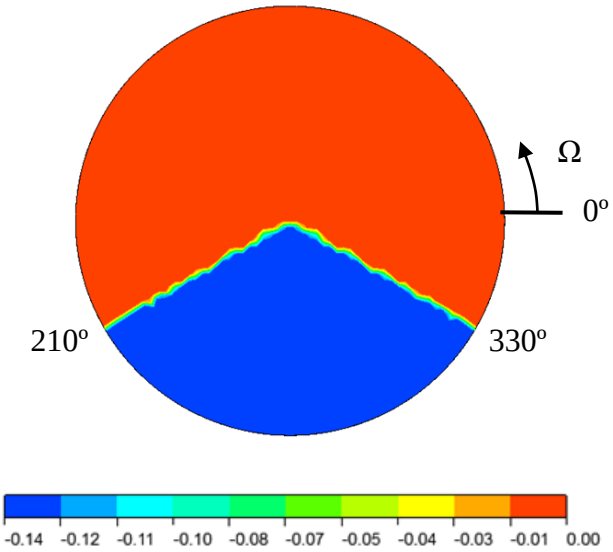

$$\frac{P_{T,inlet\ dist} - P_{T,inlet\ nodist}}{\frac{1}{2}\rho U_{tip}^2}$$

Figure 5.1 Total pressure distribution at high-speed fan domain inlet

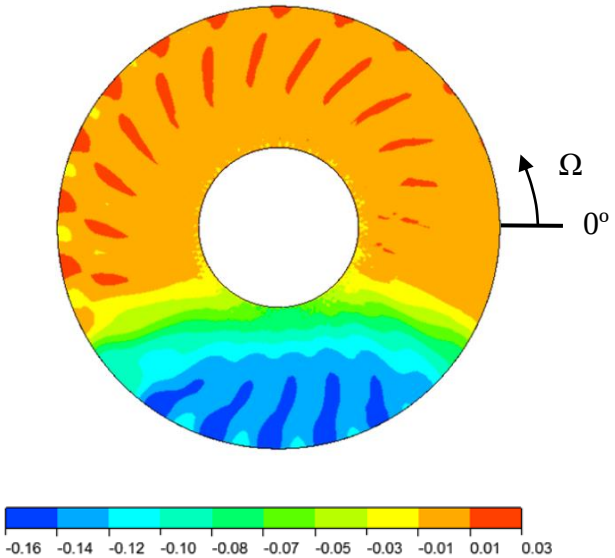

$$\frac{P_{T,LE} - P_{T,inlet\ nodist}}{\frac{1}{2}\rho U_{tip}^2}$$

Figure 5.2 Total pressure distribution at high-speed fan rotor LE plane

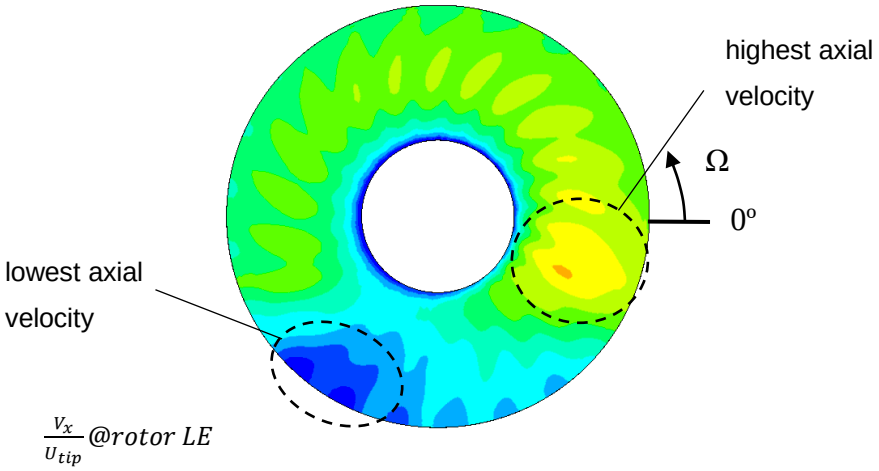

Figure 5.3 Effect of inlet distortion on axial velocity at high-speed fan rotor LE plane

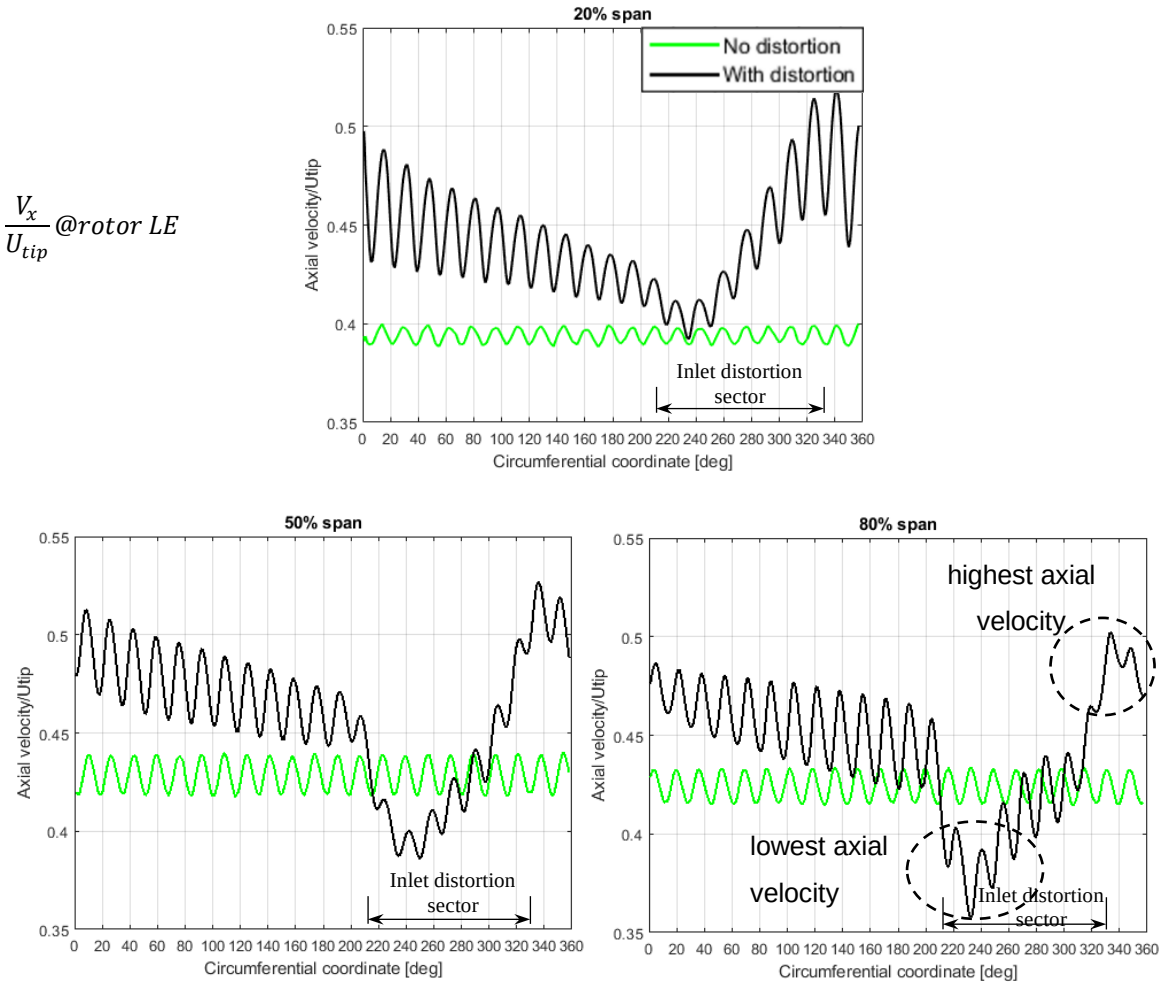

Figure 5.4 Spanwise effects of inlet distortion on axial velocity at high-speed fan rotor LE plane

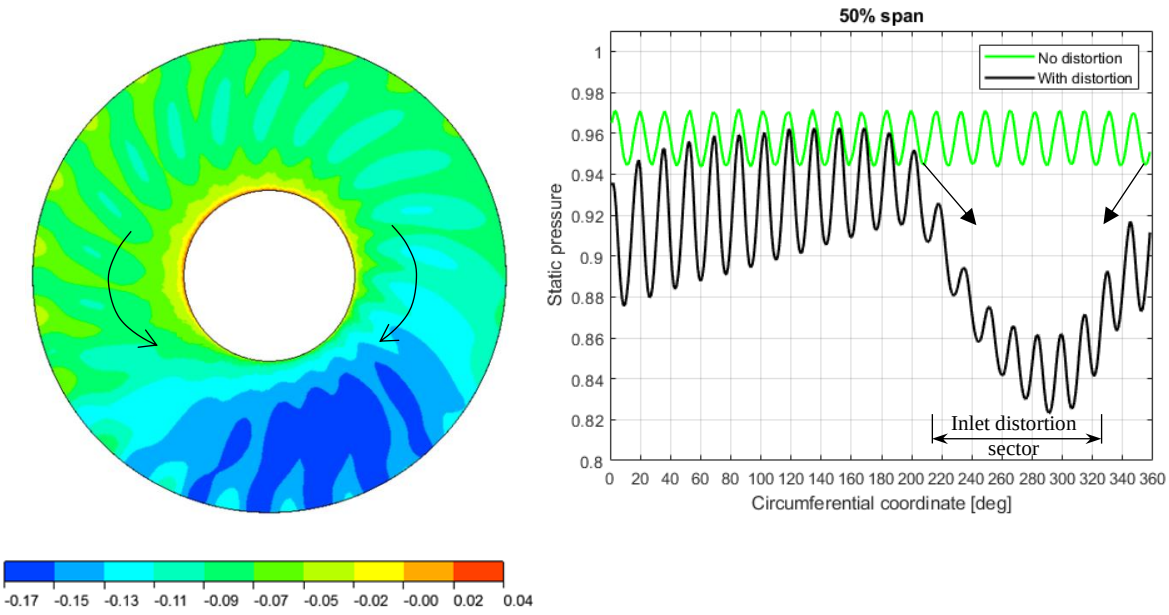

$$\frac{P_{s,LE} - P_{s,inlet\ nodis}}{\frac{1}{2}\rho U_{tip}^2}$$

Figure 5.5 Effect of inlet distortion on static pressure distribution at high-speed fan rotor LE plane

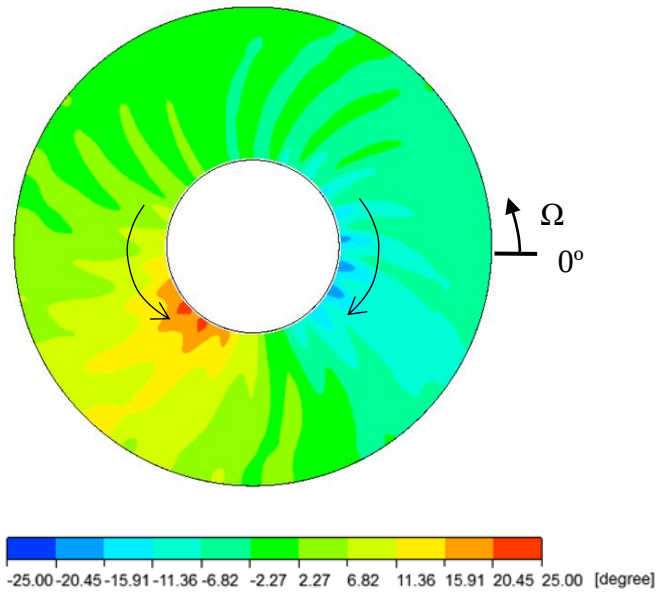

Figure 5.6 Effect of inlet distortion on absolute flow angle at high-speed fan rotor LE plane

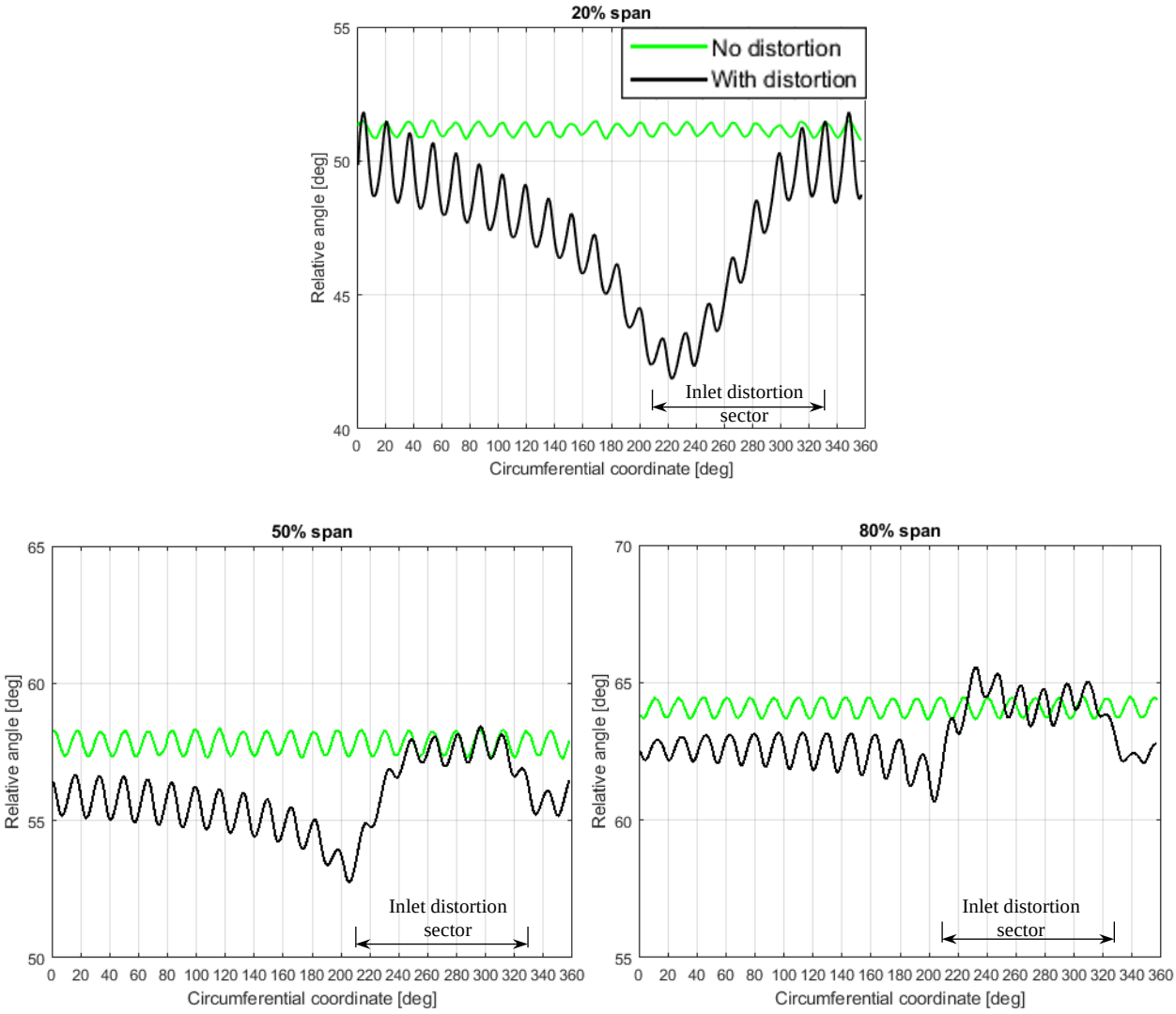

Figure 5.7 Effect of inlet distortion on relative flow angle at high-speed rotor LE plane

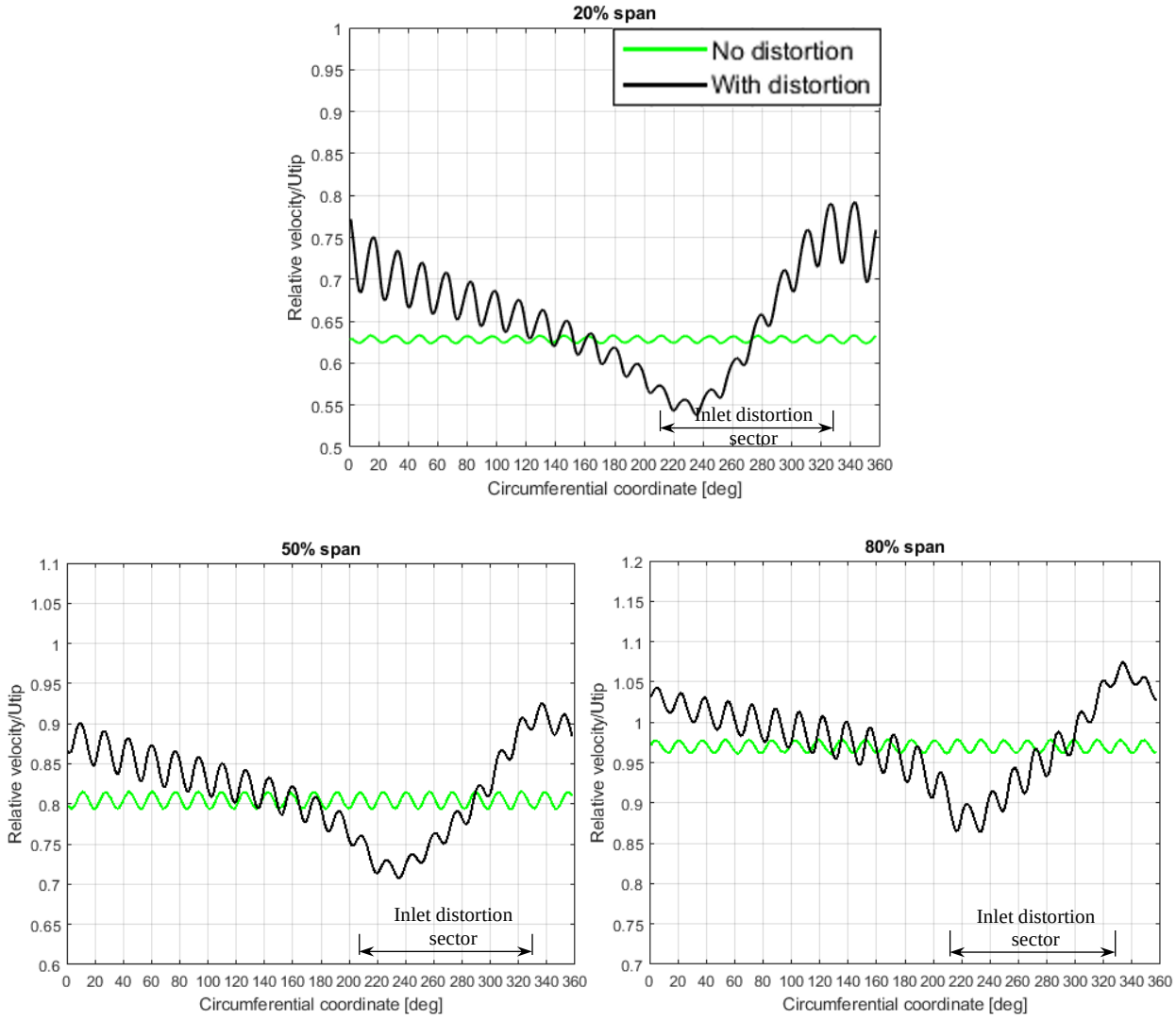

$$\frac{V_{rel}}{U_{tip}}@rotor\ LE$$

Figure 5.8 Relative flow velocity at high-speed fan rotor LE plane

5.1.2 Blade Force

As predicted at the end of Section 5.1.1, the very large swing in rotor inlet relative velocity and incidence from their smallest values near the distortion region LE to their largest values near the distortion TE, as shown in Figures 5.7 and 5.8, leads to an excessively large variation in blade (aerodynamic) force over this annular sector. Figure 5.9 shows that the blade force of the high-speed fan changes dramatically from 143 N to 366 N, such that the fan blades will be subjected to

an aerodynamic force change of almost 75% of the non-distortion level as they rotate in and out of the distortion region. Moreover, as was the case with the low speed-fan rotor, the location of maximum aerodynamic force is shifted toward the distortion region TE. In addition, Figure 5.9 also indicates that much of the blades operate below the nominal (no-distortion) value with only the blades in the narrow 280º-340º sector operating above the nominal force.

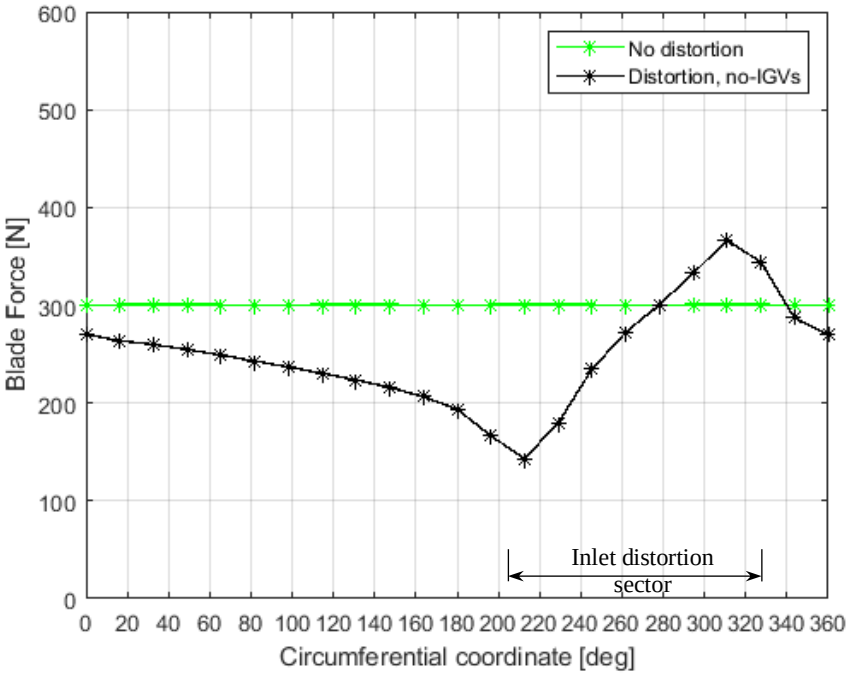

Figure 5.9 Effect of inlet distortion on blade force for high-speed fan rotor

5.1.3 Rotor Outlet Conditions

As expected from Figure 5.9, Figure 5.10 shows that the total pressure distortion worsens (variation amplitude increases) significantly as it crosses the rotor. Furthermore, the circumferential total pressure variation follows the trend of the blade force in Figure 5.9, since total pressure rise typically increases with blade aerodynamic force. However, one can see that the outer spans (50% and 80%) suffer the most from the inlet distortion as rotor exit total pressure falls below the no-distortion value around the entire annulus.

$$\frac{P_T}{\frac{1}{2}\rho U_{tip}^2} @rotor\ LE\ \&\ TE$$

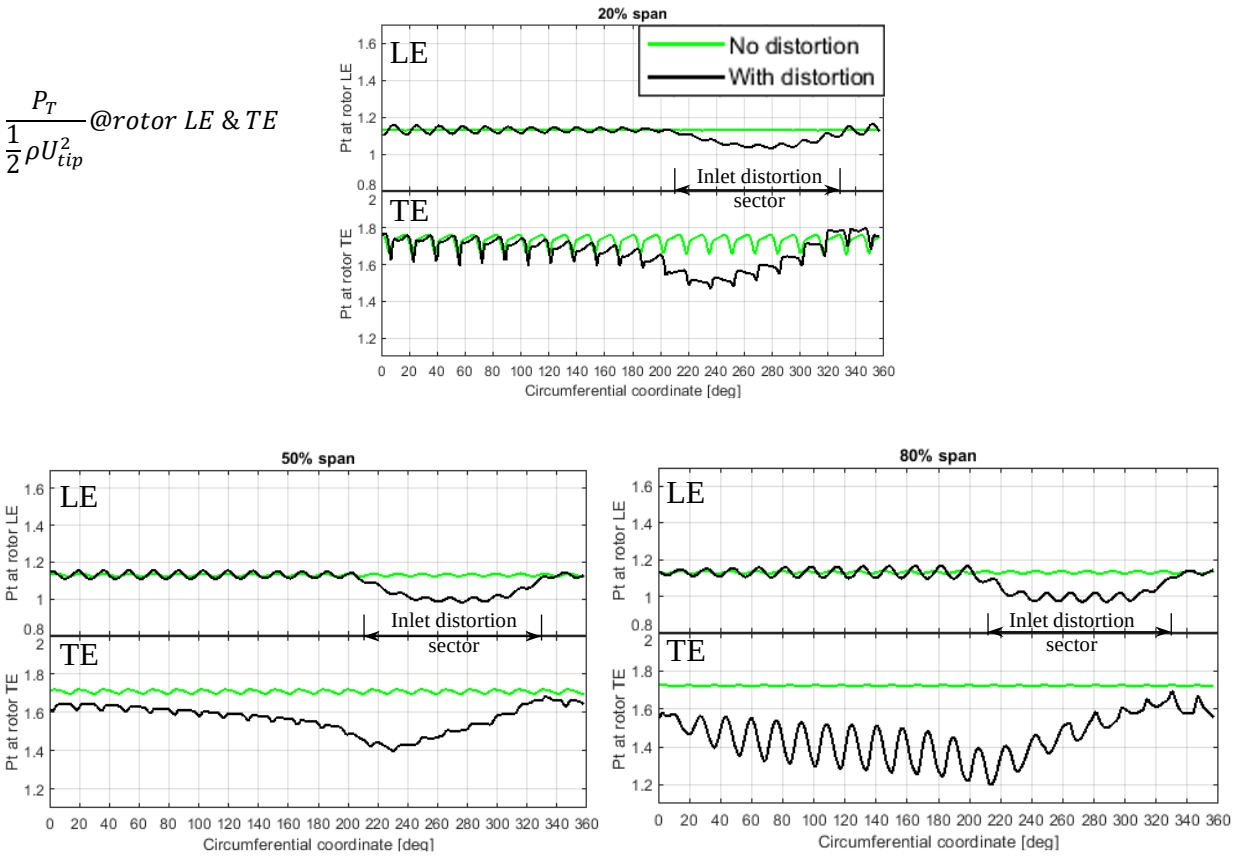

Figure 5.10 Effect of inlet distortion on evolution of total pressure from LE to TE planes of high-speed fan rotor

5.2 Asymmetric IGVs Design

Based on the data from Figures 5.9 and 5.10, the asymmetric IGVs design will have to focus in increasing the blade loading (positive exit IGV angle to induce counter-swirl) over most of the annulus with the largest counter-swirl produced around the distortion region LE (210º) and less dramatic blade loading decrease with negative IGV exit angle (co-swirl) in the 280º-340º sector. As mentioned in Chapter 3, each IGV blade design is an inviscid, infinitely thin circular arc for this case due to the length of the simulation convergence time restricting the number of design iterations. Figure 5.11 shows the TE angle distribution of the asymmetric IGVs after three design iterations, with 21 blades. The asymmetric IGVs exit angle distributions for all three design iterations can be found in Appendix C (Section C.1).

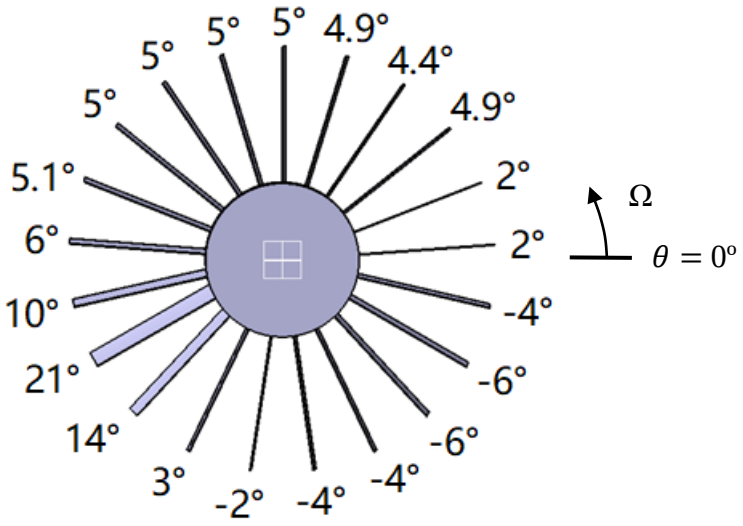

Figure 5.11 Asymmetric IGV trailing edge angles for high-speed fan rotor

5.3 Blade Force Assessment

5.3.1 Integral Blade force

Figure 5.12 plots the circumferential variation of aerodynamic blade force for the high-speed fan rotor for the no-distortion case versus those under inlet distortion without IGVS and with the asymmetric IGVs in Figure 5.11. The results show that this asymmetric IGVs design significantly reduces the variation amplitude of blade force, from nearly 75% to 27% of the nominal force. However, further improvement can be achieved by reducing the loading in the 200º-240º and 280º-340º sectors.

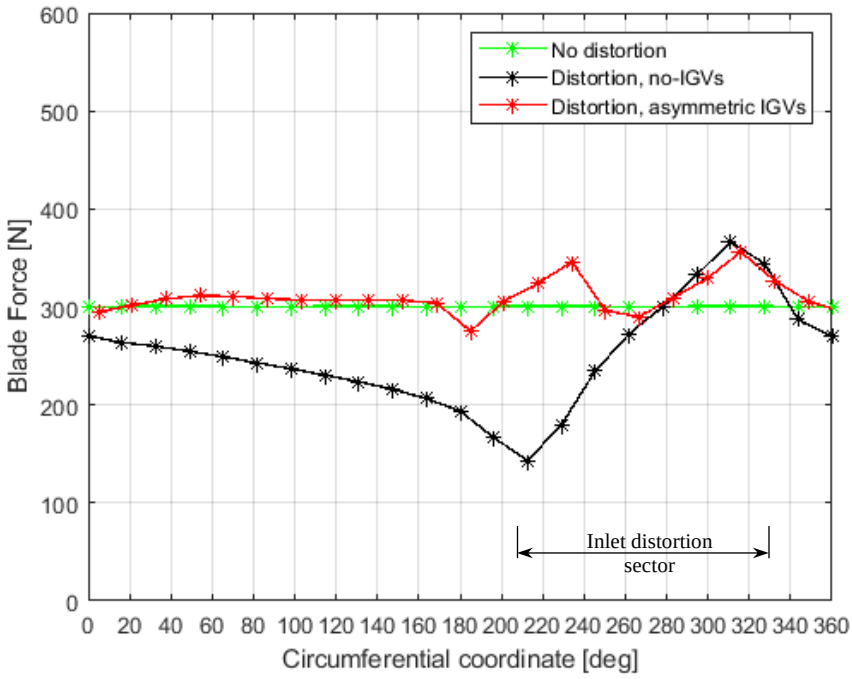

Figure 5.12 Effect of asymmetric IGVs on high-speed fan rotor blade force variation

5.3.2 Spanwise Blade Loading

The circumferential variations in blade loading at 20%, 50% and 80% spans are obtained from control volume analysis using input parameters from the CFD data in Appendix C (Section C.3). Plotted in Figure 5.13, the results indicate that this IGVs design significantly improves the blade loading uniformity over the annulus at all spans by successfully increasing the blade loading in the 0º-280º annular sector with proper modulation. However, the IGVs have some difficulty in the 200º-240º sector (near the distortion LE) where there a high loading spike at 20% and 50% span, which is seen in the resulting blade force in Figure 5.12. Figure 5.11 indicates that this region features two opposing large gradients in IGV exit angles (10º -21º-14º) that may makes it difficult to control the circumferential variation in actual flow angle without more IGV blades, at least locally. Moreover, there is also a loading spike at 80% span in the 280º-340º sector that could be corrected with 3D asymmetric IGVs blade design. Addressing these blade loading spikes should further reduce blade force variation.

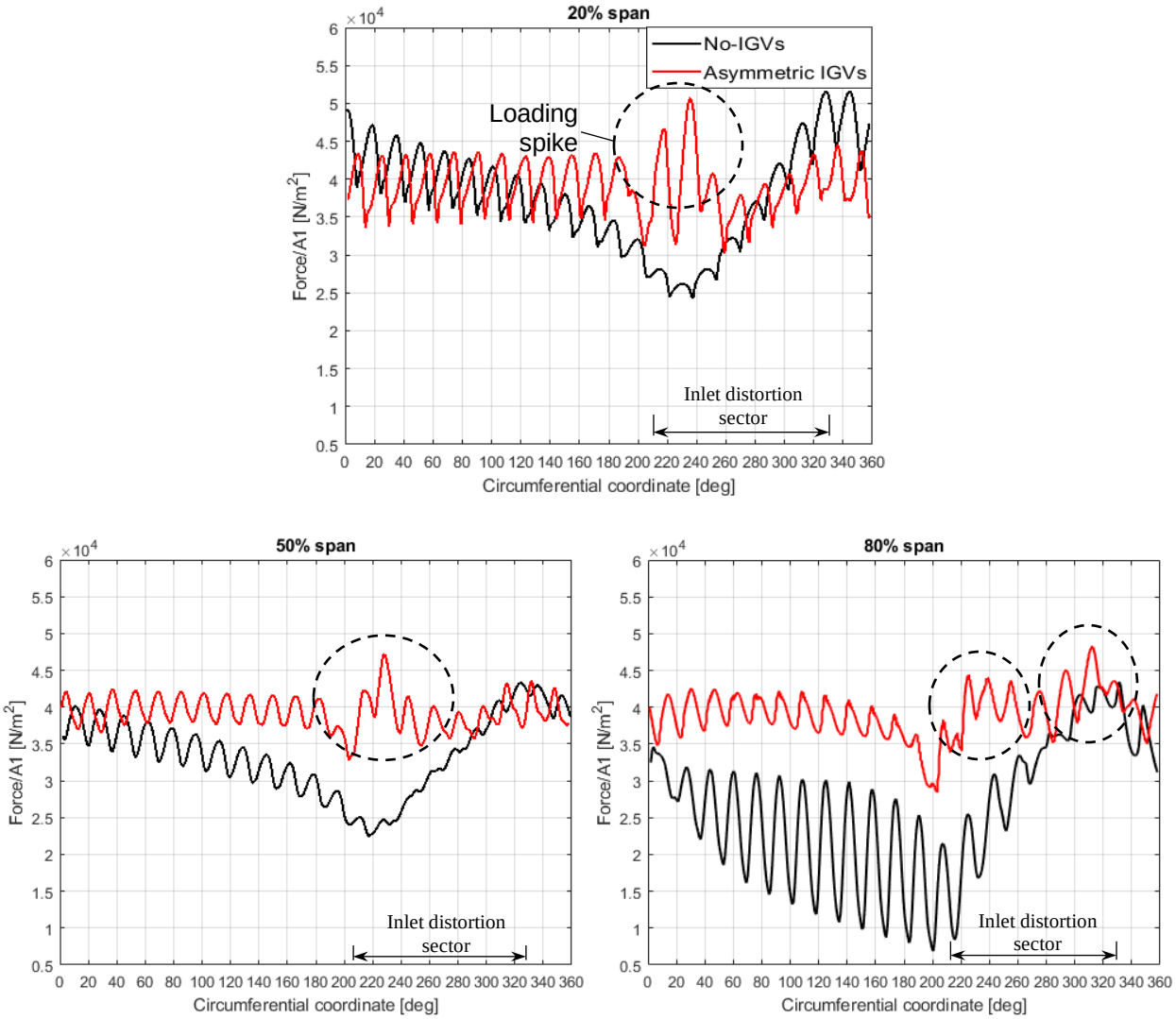

Figure 5.13 Circumferential variation of blade loading at different spans for high-speed fan rotor

5.4 Flow Field Analysis

5.4.1 Effect of IGVs on Rotor Inlet Flow

Figure 5.14 follows the same trend as Figure 5.13 in showing that this asymmetric IGVs design succeeds in reducing the non-uniformity in rotor inlet relative velocity and flow angle, with positive spikes in these parameters in the 200º-240º sector causing excessive blade loading in this region.

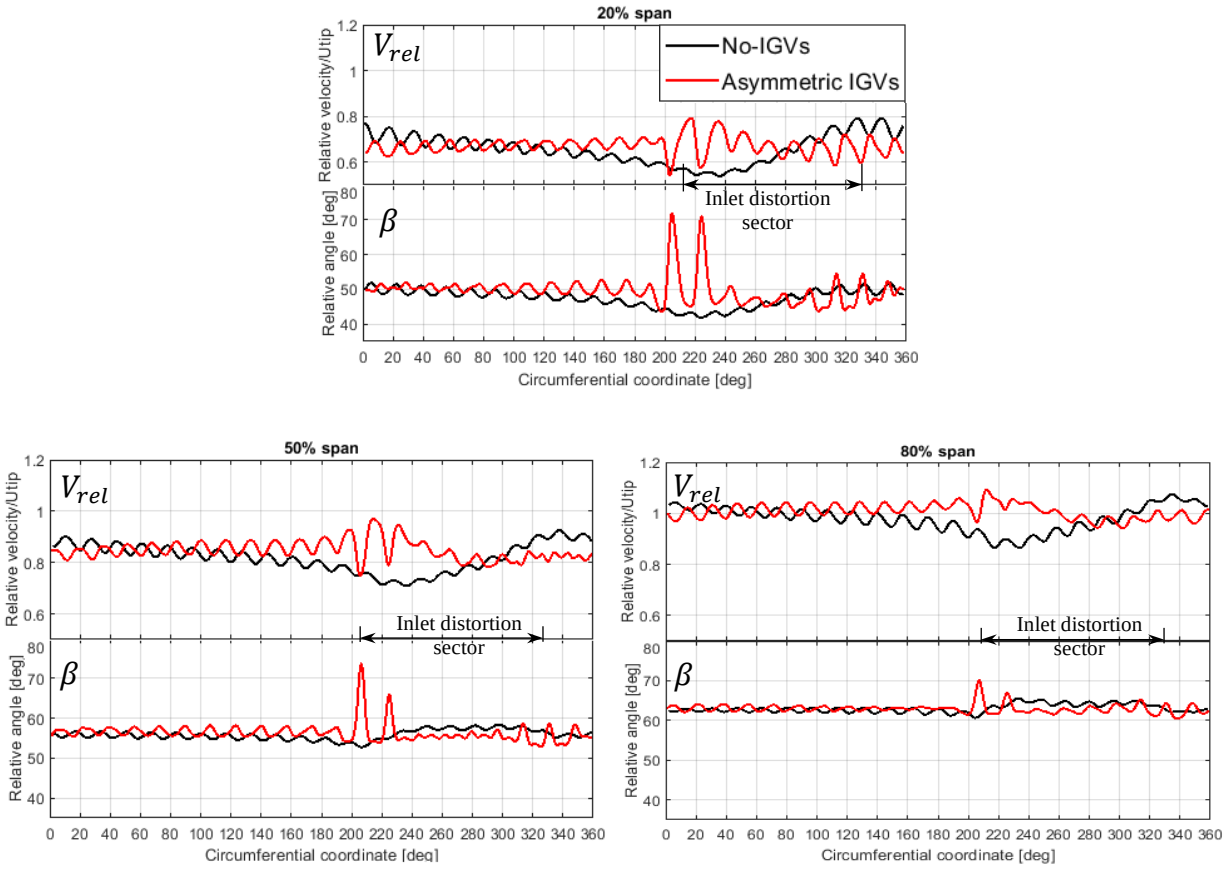

Figure 5.14 Circumferential variation of relative velocity and relative flow angle at high-speed rotor LE for different spans

5.4.2 Effect on Rotor Exit Flow Field

The comparison of the non-dimensionalized total pressure contours at the rotor TE plane for the no-distortion case to those for the distortion cases with and without IGVs are shown in Figure 5.15. It indicates that this asymmetric IGVs design attenuates the flow distortion (amplitude of total pressure variation) at the rotor exit, bringing it closer to the no-distortion case. This is more clearly observed through the rotor TE total pressure distribution at the 20%, 50% and 80% spans for the distortion cases with and without IGVs in Figure 5.16. This outcome is logical as it correlates with the trends observed in the blade loading distributions of Figure 5.13. One can expect that an improved IGVs design with more uniform blade loading distributions at all spans will also better attenuate flow distortion across the rotor.

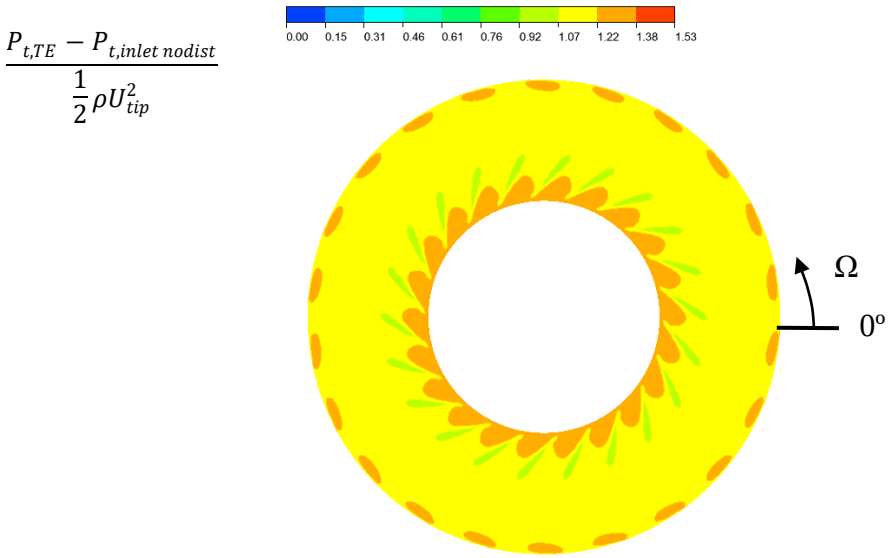

(a) No inlet distortion

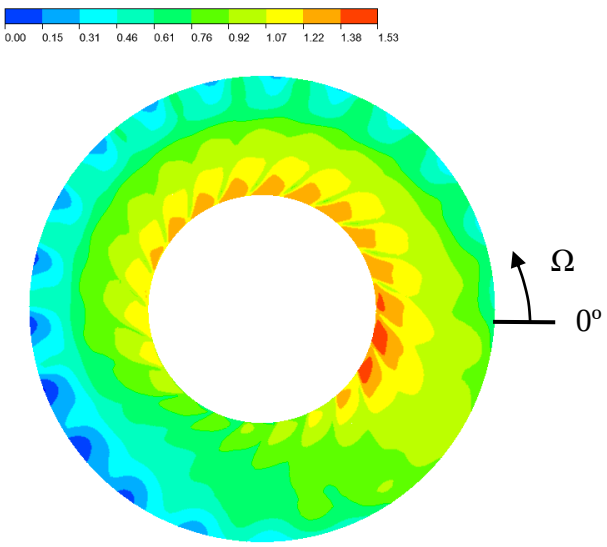

(b) Inlet distortion, without IGVs

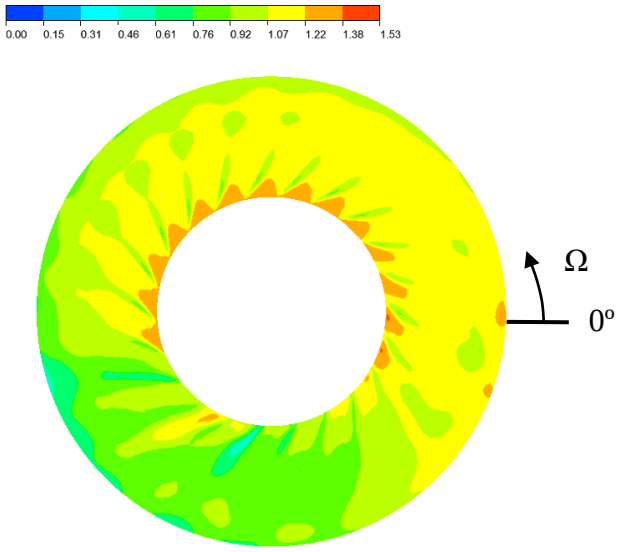

(c) Inlet distortion, with IGVs

Figure 5.15 Total pressure contours at high-speed fan rotor TE plane

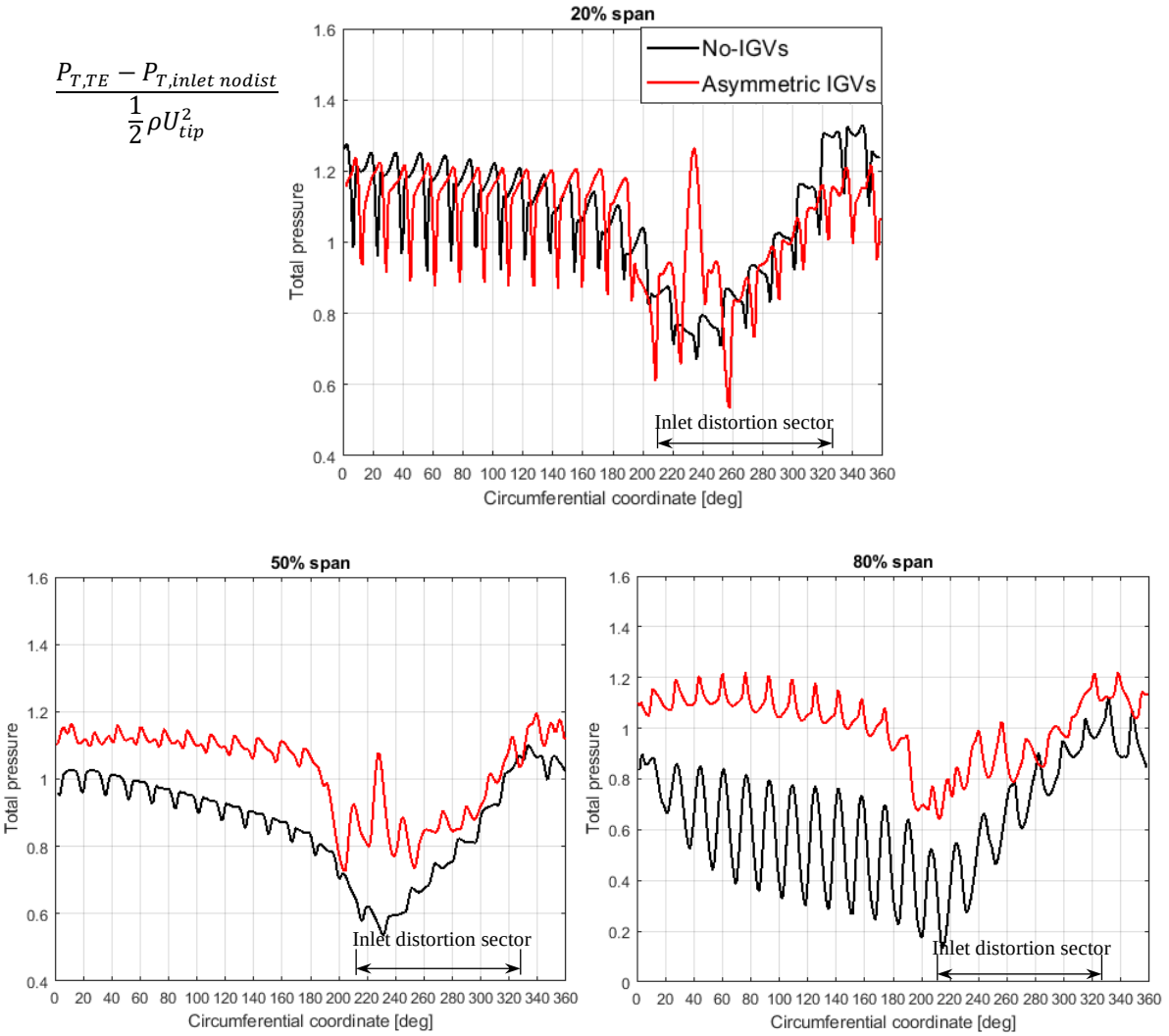

Figure 5.16 Circumferential variation of total pressure at the high-speed rotor TE for different spans

5.5 Effect on Fan Performance

Table 5.1 presents pressure ratio of the high-speed fan rotor for the cases without distortion and under inlet distortion with and without asymmetric IGVs. The results indicate that this (non-optimized) asymmetric IGVs help to recover almost 60% of the drop in total pressure rise due to inlet distortion. A better IGVs design should improve this pressure ratio recovery further while viscous losses in the real IGVs would reduce the advantage. A conservative estimation of the impact of IGV viscous loss on performance is carried out in Appendix C (Section C.4) by

estimating the loss of total pressure across a viscous IGV blade with the largest trailing edge angle (21°) obtained from RANS CFD. This loss is subtracted from the mass-averaged total pressure at the high-speed rotor TE plane and the total pressure ration is recalculated to give a value of 1.4506, which still corresponds to a 52.5% recovery in total pressure rise loss due to inlet distortion. Hence, the viscous effect if the IGV on performance is small.

Table 5.1 Effect of distortion and asymmetric IGVs of high-speed fan rotor

	No distortion	Distortion without IGVs	Distortion with Inviscid IGVs
Total pressure ratio	1.5254	1.3680	1.4590

5.6 Discussion

The results in this chapter indicate that the asymmetric IGVs concept is effective for a high-speed fan under severe inlet distortion. Indeed, even a non-optimal 2D asymmetric IGVs design reduces the integral blade force variation by two third, as well as improves total pressure uniformity at the rotor exit and recovering almost 60% of the loss in rotor total pressure rise due to inlet distortion. The spanwise blade loading analysis also suggests that the effectiveness of the asymmetric IGVs could be even further improved with in the region around the distortion LE and TE by adding more IGV blades locally (high circumferential gradient of IGV exit is required) and 3D IGVs blade design to prevent local loading spikes.

CHAPTER 6 LOW-SPEED TEST FAN STAGE RESULTS

This chapter presents the results for the test fan stage. As indicated in Section 3.1.3, particularities with this fan geometry include a virtual inviscid flow separator in the computational domain inlet (see Figure 3.6) to simulate the distortion screen arrangement in the test rig as well as straight IGVs just upstream of the rotor. These elements are expected to interfere with the flow redistribution upstream of the rotor. The effect of inlet distortion on the fan rotor is first assessed, followed by the presentation of the latest asymmetric IGVs design and the evaluation of its effects on aerodynamic blade force variation, fan rotor inlet/exit flow fields and performance. The contours plots are shown for an observer looking downstream. However, this rotor turns in the clockwise direction as opposed to the previous two fan geometries. As such, the reference (zero) angular position is the start of third quadrant (instead of first quadrant), from which the angular coordinate increases in the clockwise direction as indicated on Figure 6.1.

6.1 Effect of Inlet Distortion

6.1.1 Rotor Inlet Conditions

Figure 6.1 presents total pressure contours at the domain inlet (relative to the uniform inlet pressure with no distortion), which is characterized by lower total pressure in the distorted region between 205º and 335º. Figures 6.2 and 6.3 show the effect of distortion on total pressure and axial velocity, respectively, at the rotor LE plane. Perhaps due to the presence of the bullet, the edges of the distortion region seem to have migrated downstream becoming more radial (solid black line to dashed line in Figure 6.2). As expected, the mean total pressure and axial velocity at the rotor LE plane are lower in the distortion annular sector, confirmed by the plots of axial velocity at different spans in Figure 6.4. One can also observe through the green curves in Figure 6.4 that the inlet flow for the no-distortion case does not have blade-to-blade periodicity. The is due to the simulation procedure used to speed up the no-distortion case, as explained in Figure 3.19, resulting in a slightly non-axisymmetric inlet shroud boundary layer, the asymmetric effect is amplified by the tip clearances in the rotor and stator.

As with the previous two fan geometries under inlet distortion, Figure 6.5 indicates a lower static pressure inside the distortion region. However, the virtual inviscid flow separator in the inlet duct

and the straight IGVs seem to have significantly hindered flow local redistribution at the inlet distortion LE and TE, resulting in mass flux accumulation beyond the distortion region (which appears as axial velocity spikes in Figure 6.4), and a more sudden drop in axial velocity at the edges of the distortion region than for the two previously analyzed fans. Other indications of the stifled local flow redistribution include very spatially limited regions of induced swirl at the rotor LE plane (Figure 6.6) and relatively uniform circumferential distributions at the rotor LE plane of relative flow angle (Figure 6.7) and relative velocity (Figure 6.8) both inside and outside the inlet distortion region.

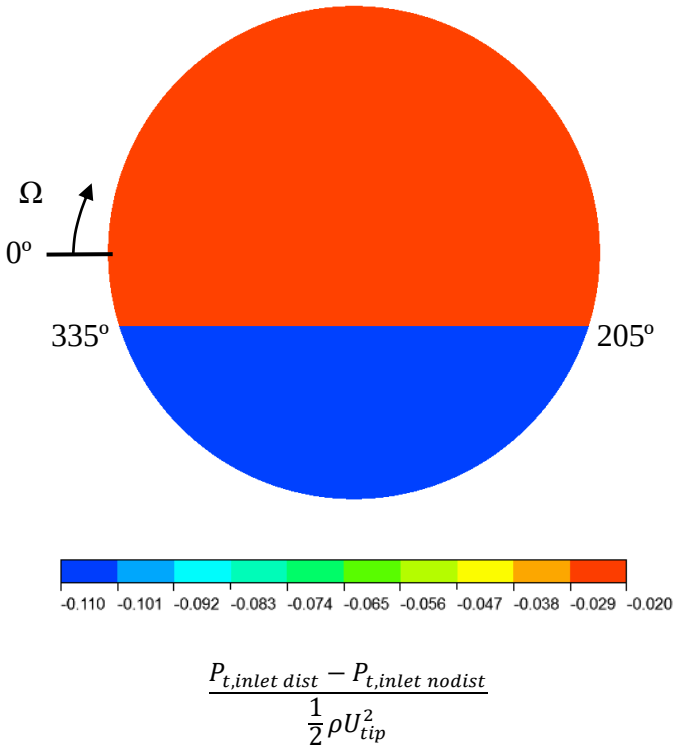

Figure 6.1 Total pressure distribution at test fan domain inlet

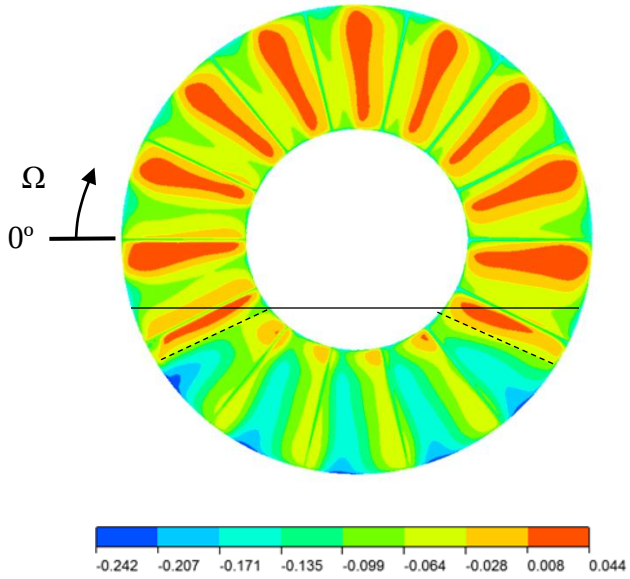

$$\frac{P_{t,LE} - P_{t,inlet\ nodist}}{\frac{1}{2}\rho U_{tip}^2}$$

Figure 6.2 Total pressure distribution at test fan rotor LE plane

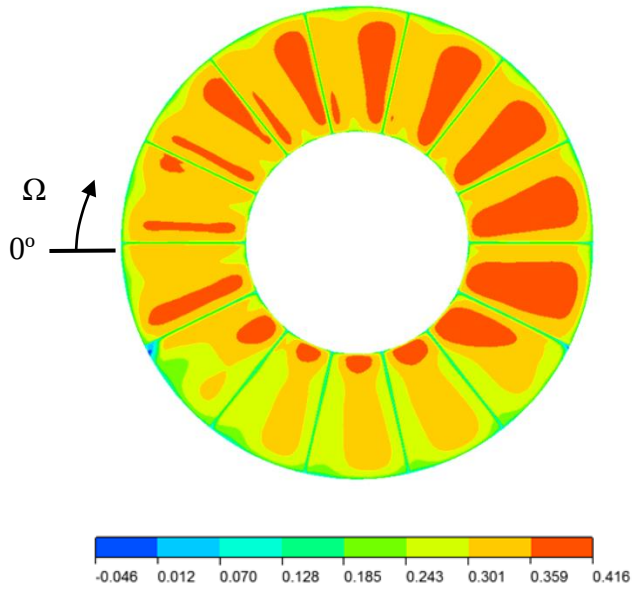

$$\frac{V_x}{U_{tip}} @rotor\ LE$$

Figure 6.3 Effect of inlet distortion on axial velocity at test fan rotor LE plane

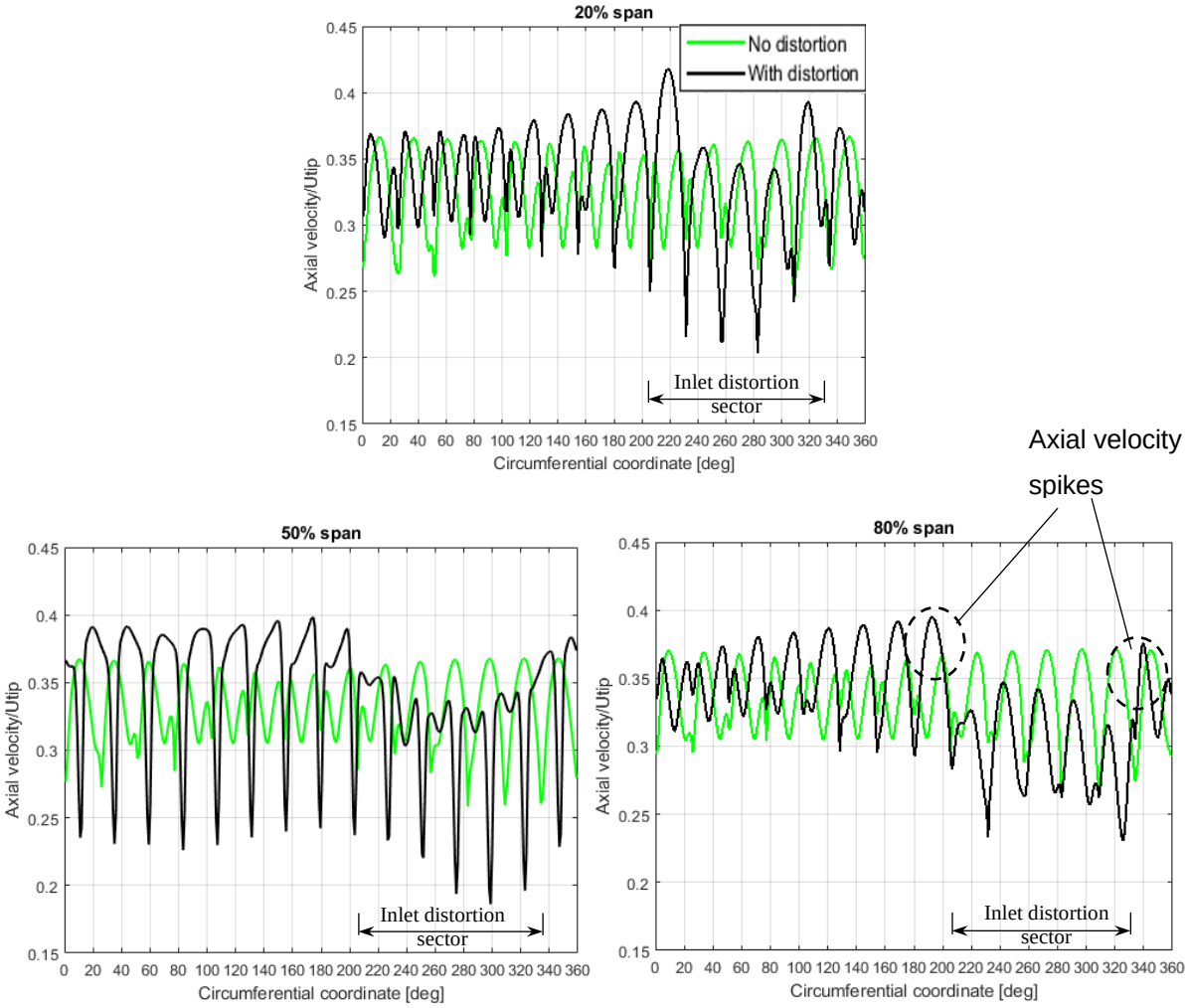

Figure 6.4 Spanwise effect of inlet distortion on axial velocity at test fan rotor LE plane

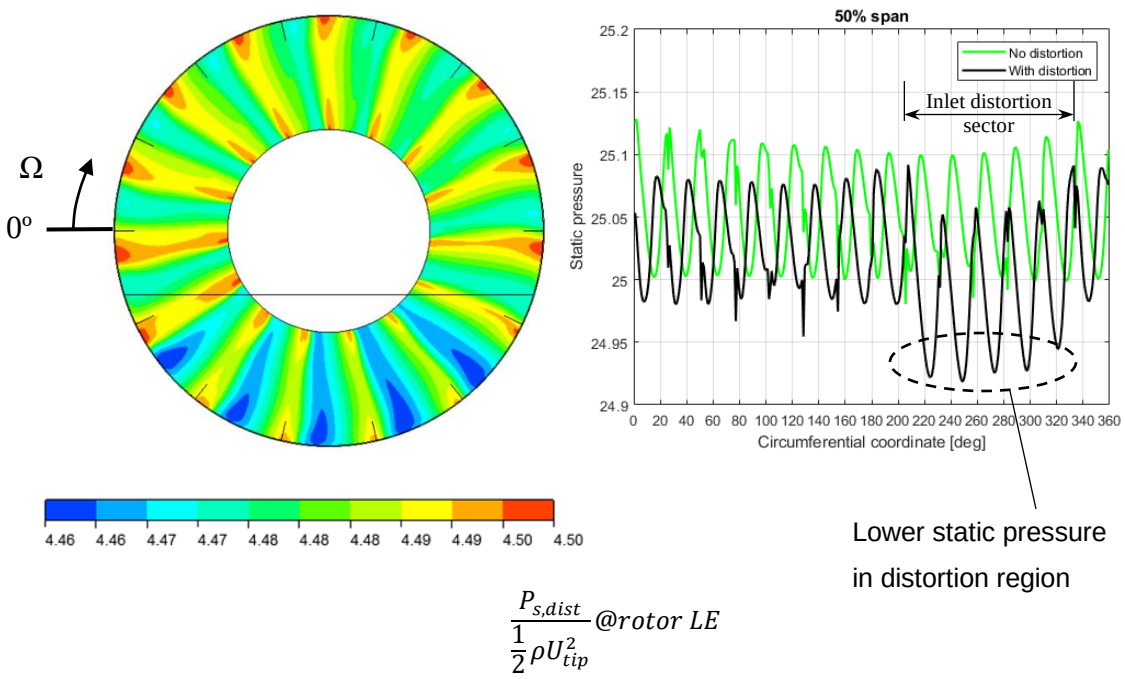

Figure 6.5 Effect of inlet distortion on static pressure distribution at test fan rotor LE plane

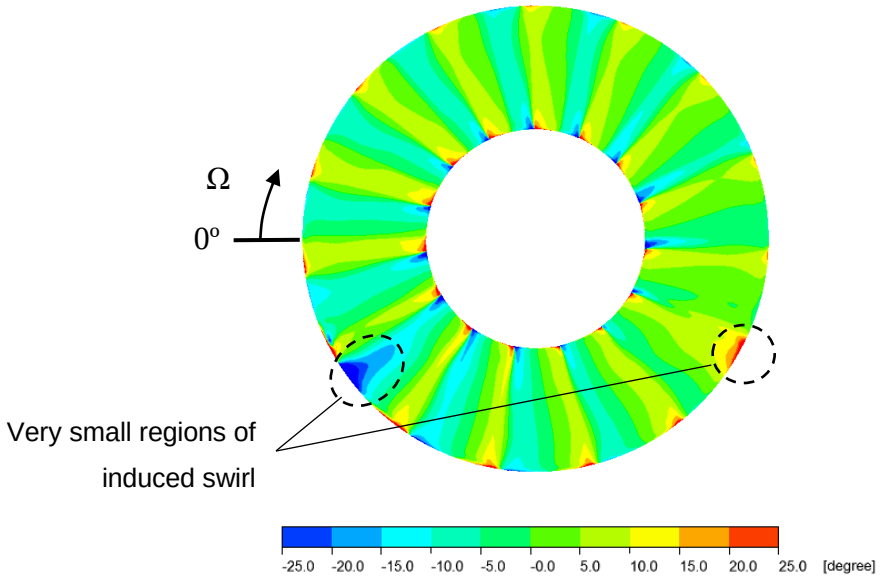

Figure 6.6 Effect of inlet distortion on absolute flow angle at test fan rotor LE plane

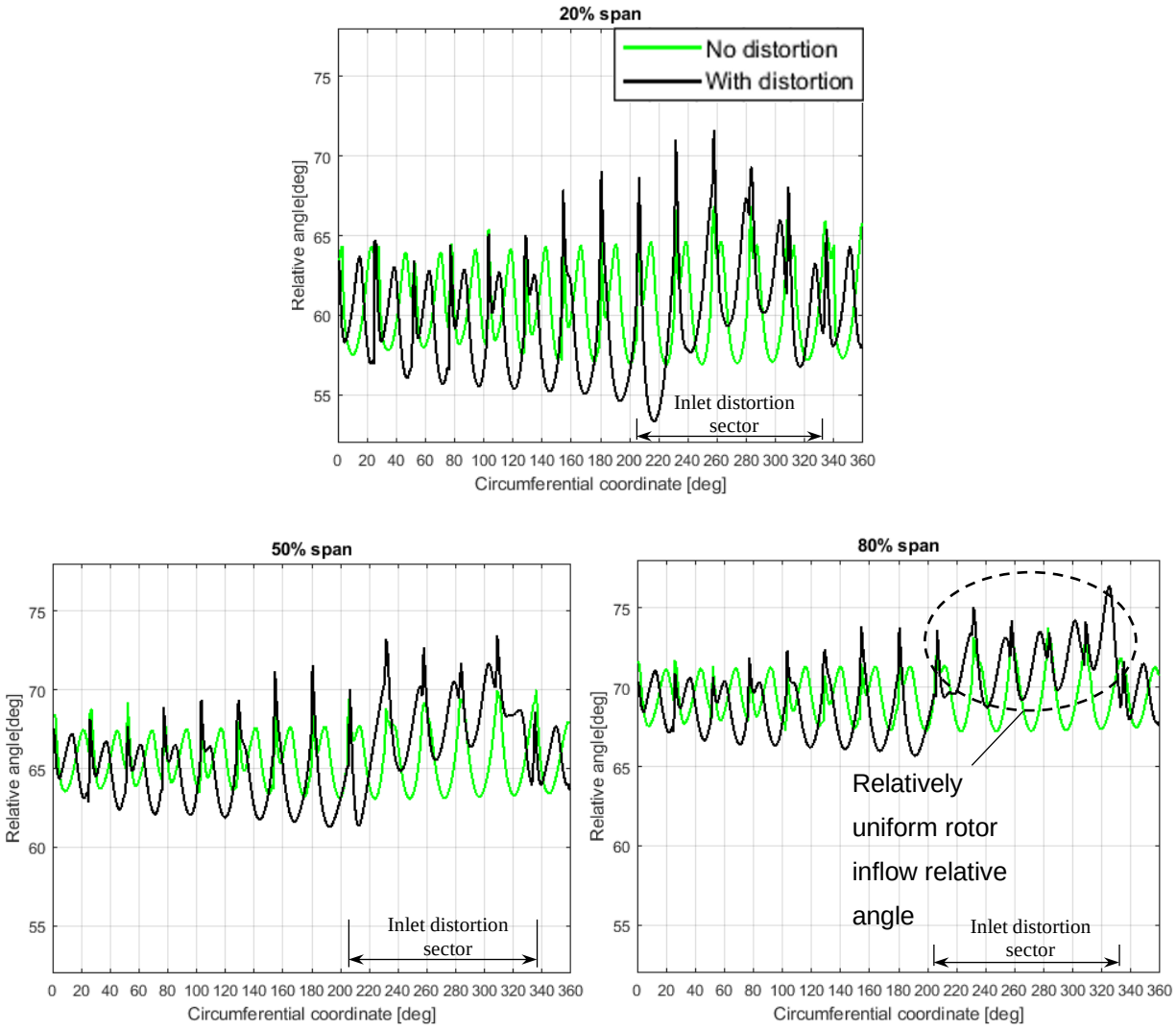

Figure 6.7 Effect on inlet distortion on relative flow angle at test fan rotor LE plane

$\frac{V_{rel}}{U_{tip}}@rotor\ LE$

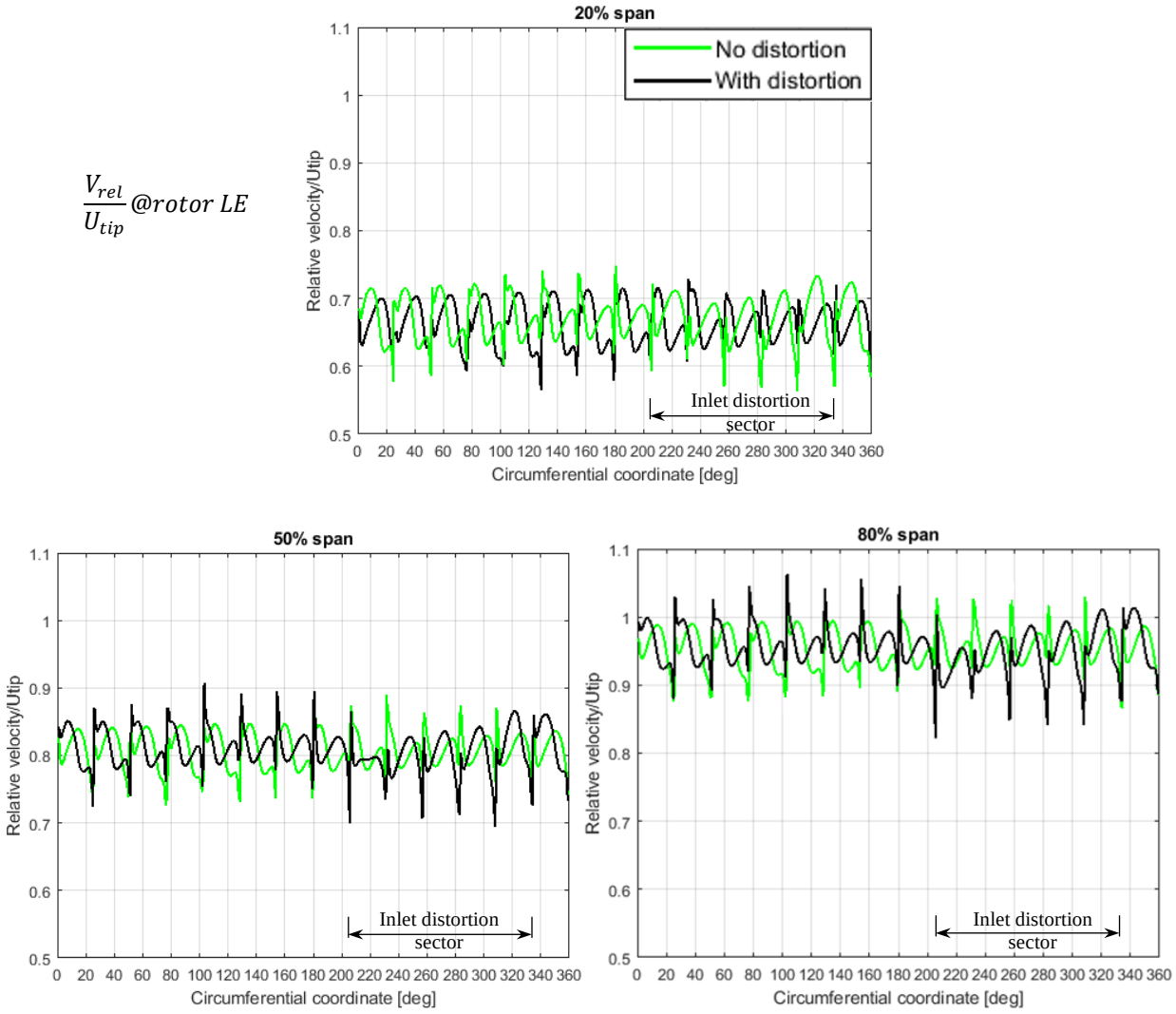

Figure 6.8 Spanwise effect of inlet distortion on relative flow velocity at test fan rotor LE plane

6.1.2 Blade Force

Figure 6.9 presents the blade force variation for the test fan rotor with and without inlet distortion (both incorporating straight IGVs). Due to the asymmetry in inlet duct shroud boundary layer, as in Figure 3.10, there is a slight circumferential variation in the blade force even without distortion. As expected from the relatively uniform circumferential distributions of relative rotor inflow (incidence) angle and velocity, both inside and outside of the distortion region, the blade force distribution is quite uniform in either of these regions with a sudden change in blade force at the distortion region LE and TE. Moreover, the variation between the maximum and minimum

blade force is only about 2% of the nominal (no distortion value) value. From these observations, one can infer that the reduction of local flow recirculation can have a potentially important impact on reducing blade force variation.

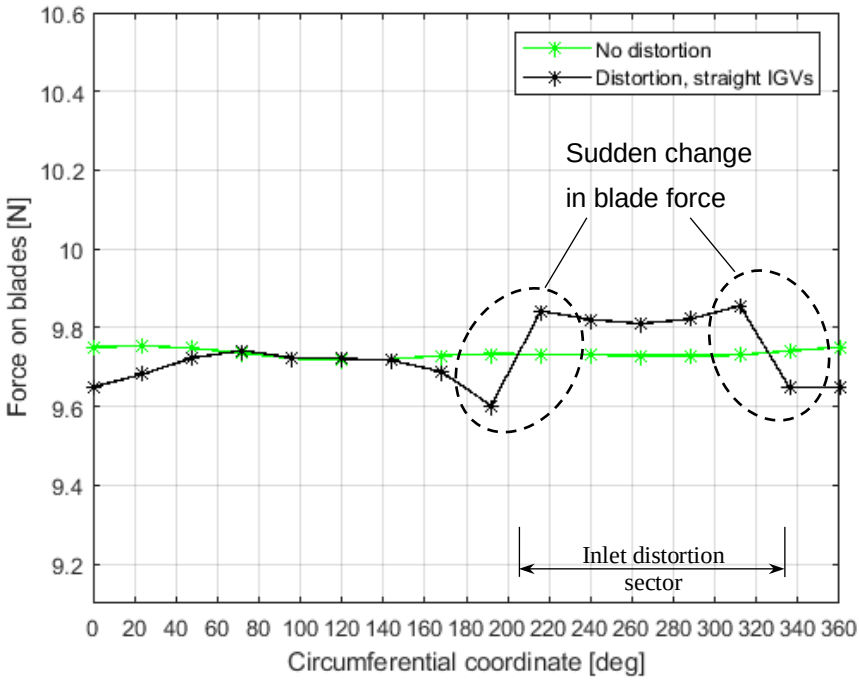

Figure 6.9 Blade force of the low-speed test fan stage

6.1.3 Rotor Outlet Conditions

Figure 6.10 presents the circumferential distribution of non-dimensionalized total pressure for the no-distortion versus distortion cases at the rotor LE and TE planes. The amplitude of total pressure distortion does not change significantly across the rotor because of the low rotation speed.

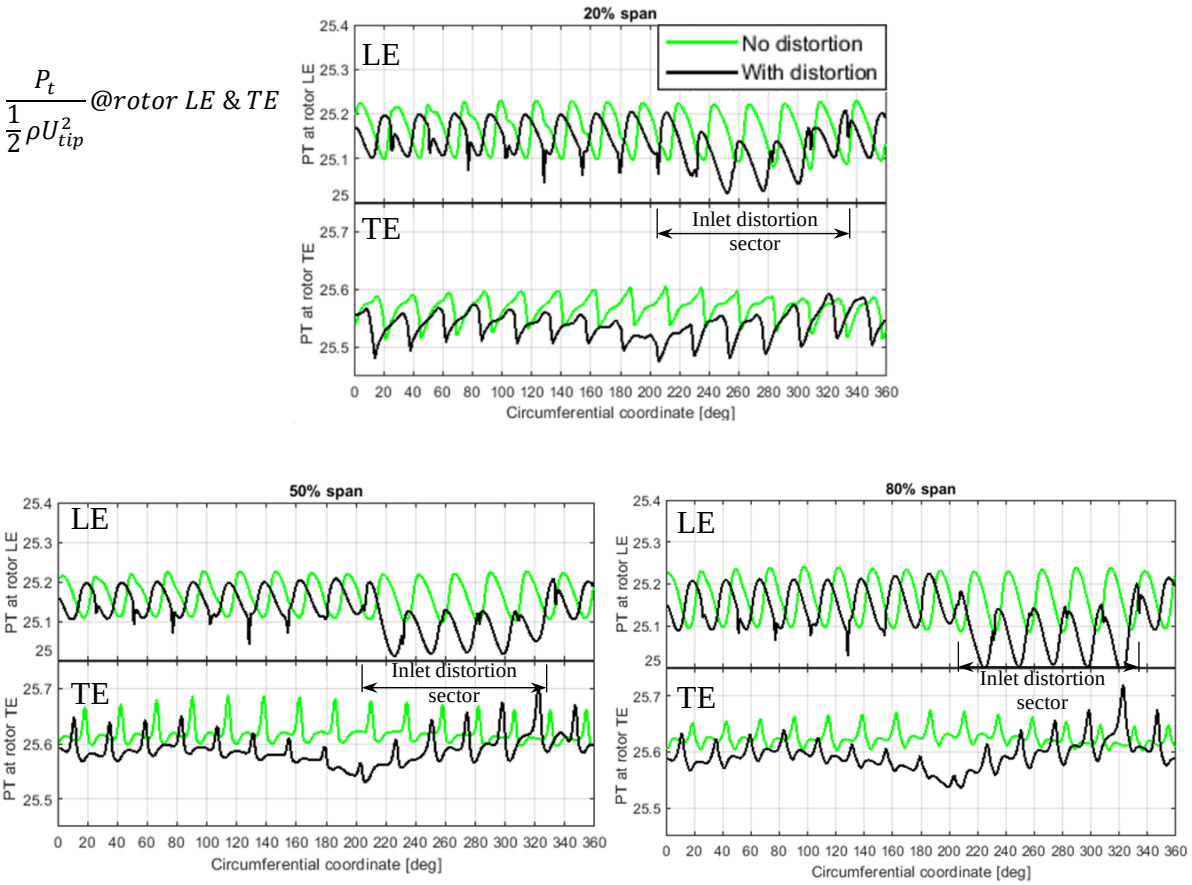

Figure 6.10 Effect of inlet distortion on evolution of total pressure from LE to TE planes of test fan rotor

6.2 Asymmetric IGVs Design

Due to the long convergence time, the IGVs design is 2D in nature. The last of four IGVs design iterations is shown in Figure 6.11. The asymmetric IGVs exit angle distributions for all four design iterations can be found in Appendix D (Section D.1). Again, negative IGV exit angle induces co-swirl (reduces blade loading) and positive IGV exit angle causes counter-swirl (increased blade loading). In this case, due to the large IGV exit flow angles close to the distortion region TE, more IGV were added to this area to ensure proper flow turning, while blades are removed from location with low IGV exit angle in order to keep the number of blades reasonable. The sudden change in force near the edges of the distortion region resulted in large gradient in IGV exit angle as well (from -10º to -30º and from -20º to 40º at the distortion region

LE and TE, respectively) making the design of the asymmetric IGV blades difficult and their effectiveness questionable in these regions.

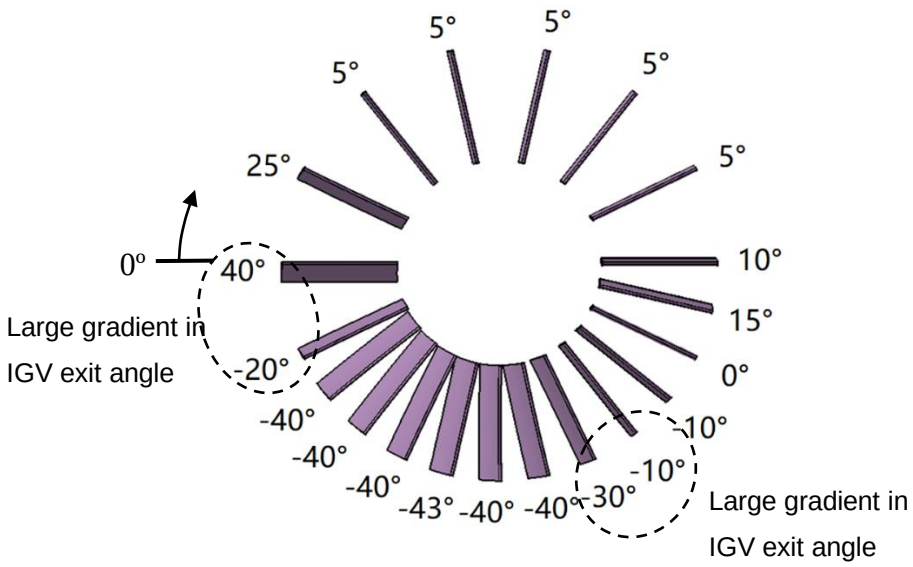

Figure 6.11 Asymmetric IGV trailing edge angles for test fan rotor

6.3 Blade Force Assessment

6.3.1 Integral Blade Force

Figure 6.12 presents circumferential variation of aerodynamic blade force for the cases with and without inlet distortion (both with straight IGVs) and with inlet distortion. While the IGVs succeed in reducing blade force in the middle part of the annular distortion sector, it has a lot trouble at the edge of the distortion region where the blade force varies suddenly. The large gradient in IGV exit angle in these regions render the design ineffective, especially near the distortion region TE (in the 300º-360º-0º-20º annular sector). As a result, the amplitude of the blade force variation under distortion (through small) is increased by this asymmetric IGVs design due its poor performance in the 300º-360º-0º-20º annular sector.

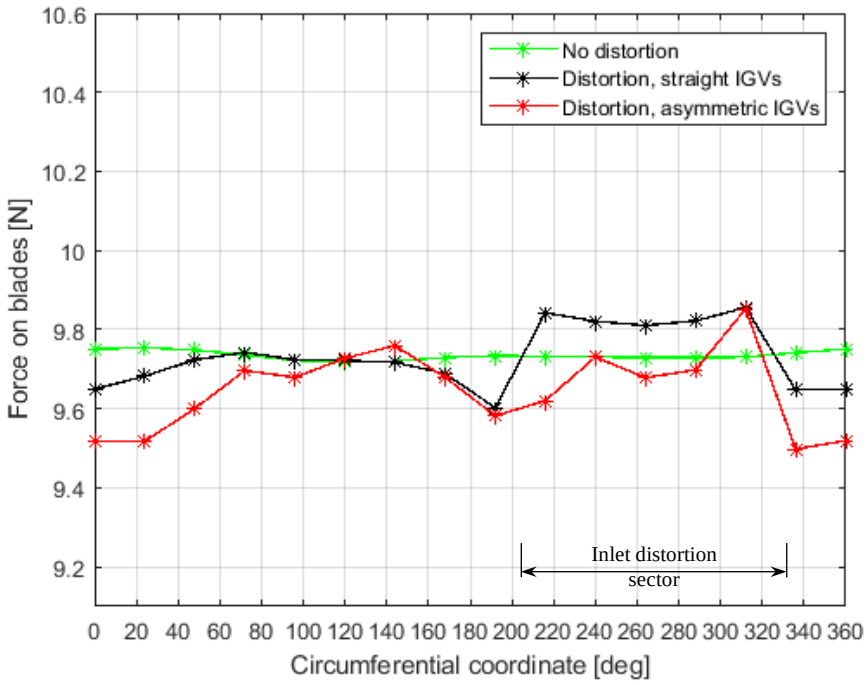

Figure 6.12 Effect of asymmetric IGVs on test fan rotor blade force variation

6.3.2 Spanwise Blade Loading

Figure 6.13 plots the circumferential distribution of blade loading at 20%, 50% and 80% span with distortion by straight IGVs and with asymmetric IGVs, as obtained from a control volume analysis using CFD data in Appendix D (Section D.3). Although the blade loading uniformity is slightly improved at the outer spans, the large variation in blade loading in the 300º-360º annular sector in Figure 6.12 comes from the lower (20%) span where the blade loading drops excessively, by around 60%. While a flow field analysis will provide more clues to the cause, one can already conclude that a 2D IGVs design is inadequate in this case.

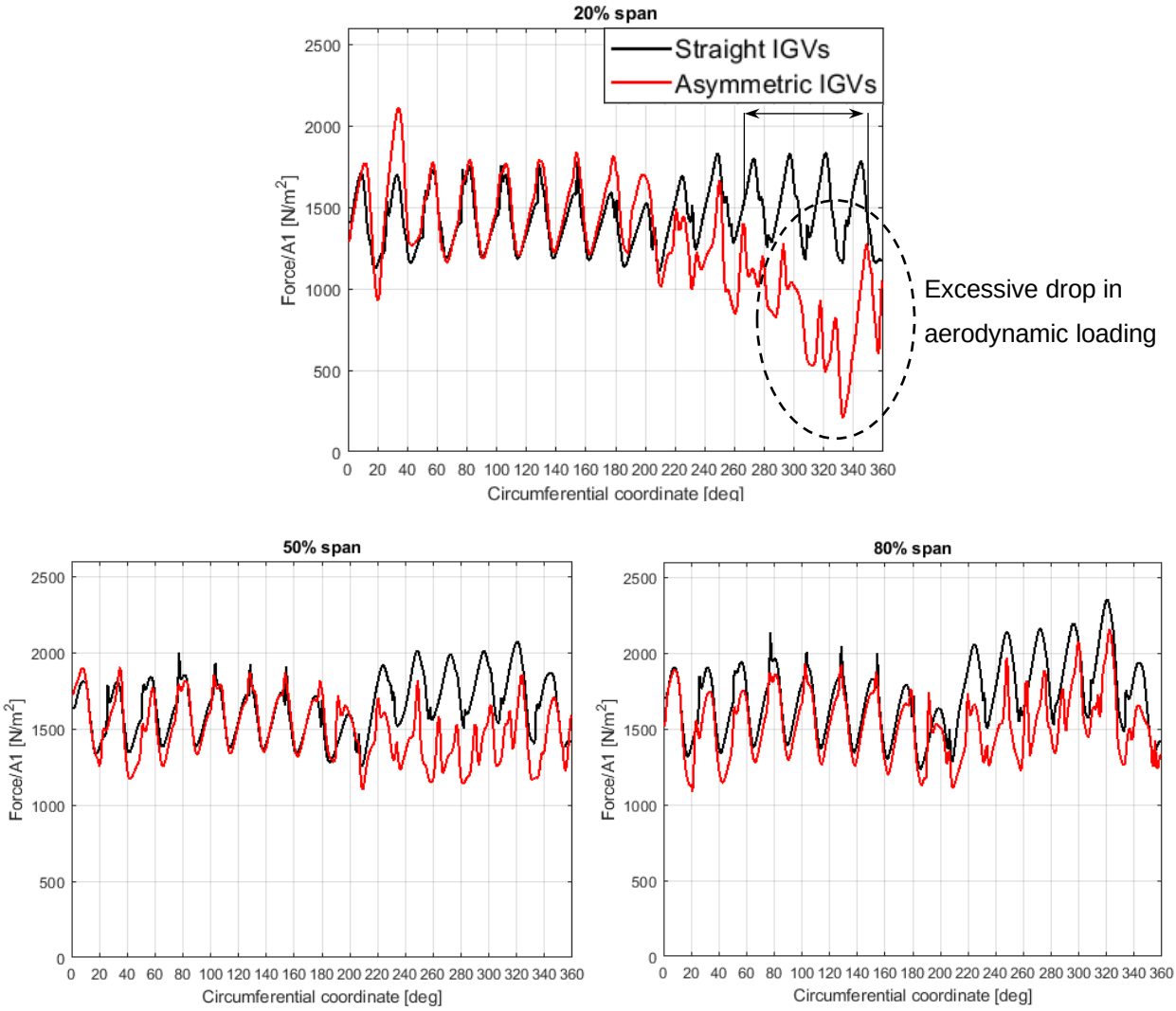

Figure 6.13 Circumferential variation of blade loading at different spans for test fan stage rotor

6.4 Flow Field Analysis

6.4.1 Effect of IGVs on Rotor Inlet Flow

Figure 6.14 presents the relative velocity and flow angle at the test fan rotor LE plane at 20%, 50% and 80% span. The relative velocity is reduced in the distortion region for all spans. In the aft part of the distortion region at 20% span, the flow exhibits an approximate 10° drop in relative incidence angle., which is enough nullify any local pressure rise across the rotor. Moreover, this is followed immediately by spikes in incidence angle of about 20°, enough to stall a fan blade in

the 300º-360º annular sector. This flow angle behaviour explains the excessive drop in aerodynamic loading seen at 20% span in Figure 6.13.

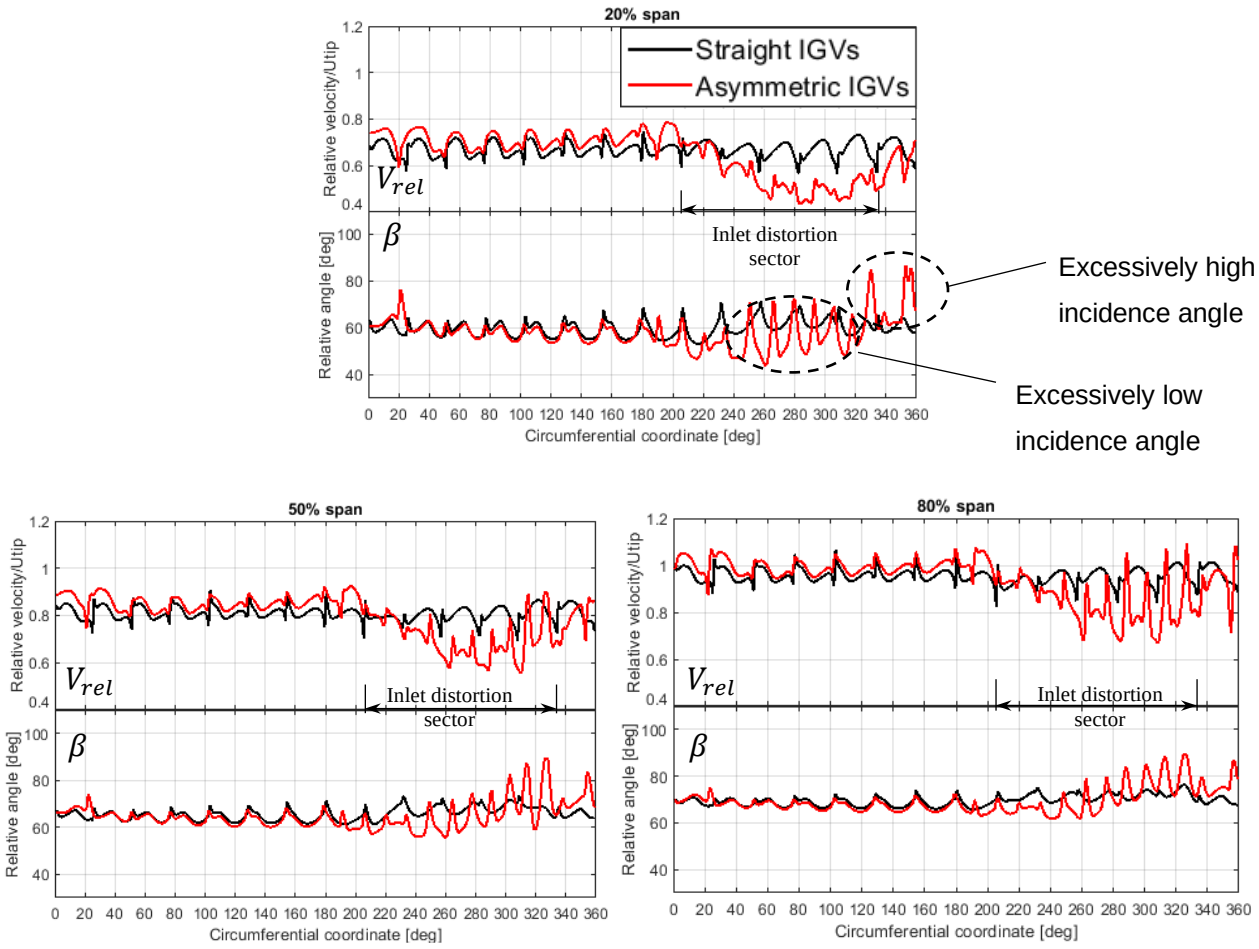

Figure 6.14 Circumferential variation of relative velocity and relative flow angle at test fan rotor LE for different spans

6.4.2 Effect of IGVs on Rotor Exit Flow

Figure 6.15 presents the non-dimensional total pressure contours at the test fan rotor TE plane for the cases with and without inlet distortion and straight IGVs, and with distortion and asymmetric IGVs. As expected based on Figures 6.12 through 6.14, the results show that this asymmetric IGVs design makes the total pressure circumferential non-uniformity worse, particularly in the 300º-360º-0º-20º annular sector. One can see that at 20% span, the excessively low and high incidence issues in Figure 6.14 leads to very low total pressure rise near the hub in Figure 6.15

(c). Again, one can observe that the rotor exit total pressure distribution with inlet distortion and straight IGVs are already quite uniform, which leads one to suspect that straight IGVs are successful in attenuating the impact of inlet distortion through limiting local flow redistribution.

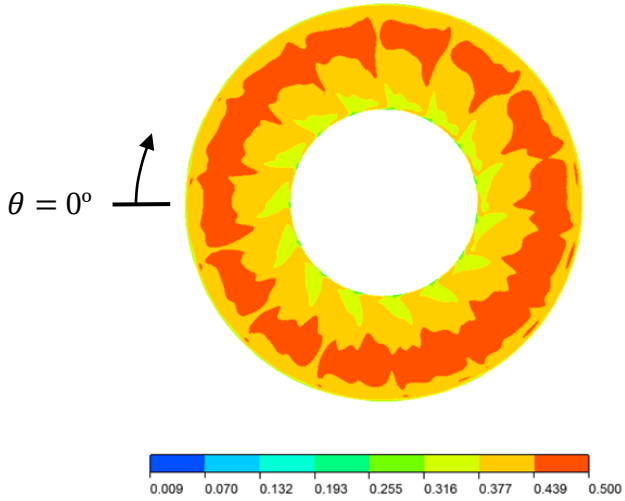

(a) No distortion, straight IGVs

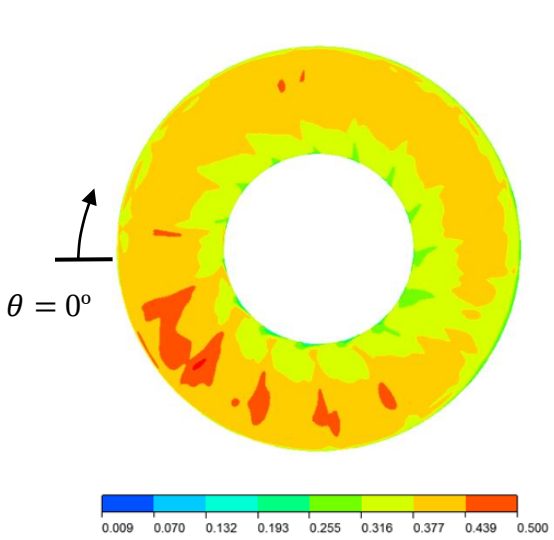

(b) Inlet distortion, straight IGVs

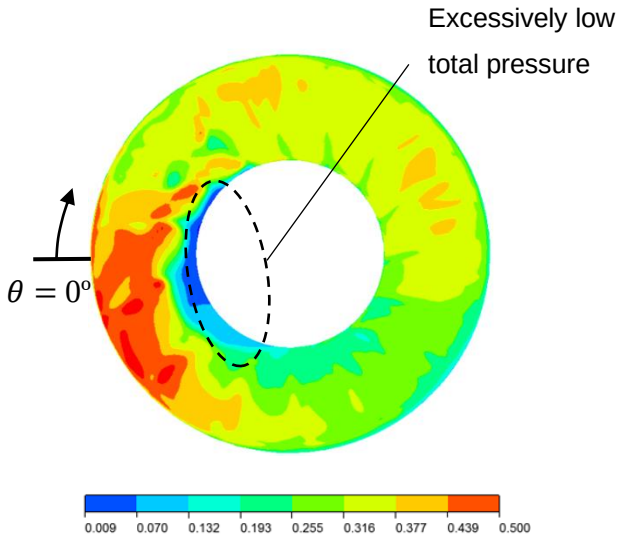

(c) Inlet distortion, asymmetric IGVs

$$\frac{P_{t,TE} - P_{t,inlet\ nodist}}{\frac{1}{2}\rho U_{tip}^2}$$

Figure 6.15 Total pressure contours at test fan rotor TE plane

6.5 Effect on Fan Performance

Table 6.1 compares pressure ratio for the test fan stage for the cases with and without inlet distortion and straight IGVs versus the case with inlet distortion and asymmetric IGVs. As expected, rather than alleviating it, the results show that the poor performance of asymmetric IGVs causes a further drop in pressure ratio.

Table 6.1 Pressure ratio comparison of test fan stage

	No distortion with straight IGVs	Distortion with straight IGVs	Distortion with IGVs
Total pressure ratio	1.0161	1.0149	1.0131

6.6 Discussion

The results in this chapter indicate that distortion screen location and straight IGVs in the low-speed distortion test rig cause the fan stage response peculiar and probably unrealistic, in that the stifled flow distribution results in very small (hard to measure) aerodynamic blade force variation with sudden jump in blade force at the edges of the distortion region. The asymmetric IGVs design has a lot trouble with the latter feature due to the large circumferential gradient in IGV exit angle. Moreover, a 2D IGVs design is totally inadequate for this fan setup as it leads to excessively low and high incidence angles in the distortion region and around its TE near the hub that negate total pressure rise. As a result, the 2D asymmetric IGVs design is ineffective in this case. Based on these results, the experimental validation of the asymmetric IGVs concept should be done on a fan rig with the following features: high-speed for higher (measurable) force variation, and distortion screen placed further upstream and no straight IGVs for more realistic flow redistribution.

On the other hand, the results in Chapter 6 also suggests that a straight IGVs may be highly effective in attenuating the impact of inlet distortion by reducing local flow redistribution at the edges of the distortion region. A preliminary assessment of this hypothesis is carried out on the high-speed fan rotor of Chapter 5, for which a simulation with straight IGVs are carried. The

results shown in in Appendix C (Section C.5) indicate that even the local flow redistribution is reduced, the effectiveness of the straight IGVs in attenuating the variation in blade force is far below than that of the asymmetric IGVs.

CHAPTER 7 CONCLUSIONS AND FUTURE WORK

This work represents the first evaluation of a novel concept to attenuate the effect of inlet distortion on fans used for aircraft propulsion to enable the implementation of future BLI aircraft. The concept consists of placing a row of asymmetric IGVs just upstream of the fan to produce a spatially varying swirl distribution. The swirl distribution is tailored to reduce flow incidence in the distorted flow region and to increase it in the undistorted flow region to attenuate the negative effects of inlet distortion on fan structure and performance. The objective of this project is to assess the effectiveness of the asymmetric IGVs concept for attenuation of inlet distortion effects on low and high-speed fans, in terms of reducing the aerodynamic force fluctuation amplitude on the fan blades, the attenuation of total pressure distortion at the fan rotor exit, as well as the recovery of loss in fan aerodynamic performance due to inlet distortion.

A computational study is carried out on three fan geometries: a low-speed fan rotor scaled with an inlet distortion pattern imported from a published work for a low-speed fan; a high-speed (transonic) fan rotor (NASA Rotor 67) with published geometry and test/CFD data under large inlet distortion; a low-speed test fan stage from a distortion test rig at Polytechnique Montréal in which the fan rotor is preceded by a row of straight IGVs and followed by a stator. The evaluation of the concept on the last geometry is aimed at experimentally validating the asymmetric IGVs concept. Full-annulus, unsteady, 3D CFD simulations are carried out in ANSYS CFX, a commercial RANS CFD code, with a distortion pattern prescribed in the form of an asymmetric distribution of total pressure at the computational domain inlet. To keep the simulation time and resources manageable, the simulations are performed without inviscid surfaces and no tip clearance, except for the last geometry since it is intended to be rig tested. For each geometry, simulations are first carried out with and without the inlet distortion to evaluate the effect of inlet distortion on inlet flow redistribution and blade aerodynamic force distribution around the annulus. The latter is then used to design the asymmetric IGVs through a process of hand iterations and CFD simulations, to take into account the change in flow redistribution with every asymmetric IGVs geometry. The IGVs design is assumed to be thin inviscid circular arcs for the first two fans and limited to 2D IGV blades for the last two fans, due to computational time and resource constraints. The asymmetric IGVs design are assessed in terms of blade

aerodynamic force variation around the annulus, total pressure distortion at the fan rotor exit and fan pressure ratio in comparison to the nominal and with-distortion cases.

For the low-speed and high-speed fan rotors, local flow redistribution at the edges of the distortion region leads to relatively smooth circumferential variation of rotor blade aerodynamic force, which is relatively small (7%) for the low-speed fan and very large (75%) for the high-speed fan. In both cases, the asymmetric IGVs design, though not optimized, reduces the aerodynamic force variation amplitude by approximately 66%. The asymmetric IGV designs also recover half or more of the loss in rotor total pressure rise due to inlet distortion, although this gain will be slightly offset if viscous IGVs were used. The asymmetric IGVs are also able to reduce the total pressure distortion at the fan rotor exit for the high-speed fan but were not successful for the low-speed fan. Spanwise analysis indicates that the effectiveness of the asymmetric IGVs can be improved on all three metrics if better 3D IGV blade shaping are carried out.

In the case of the test fan stage, the local flow redistribution at the edges of the distortion region is reduced due to the straight IGVs and position of the distortion screen, leading to sudden changes in rotor blade aerodynamic force near the edges of the distortion region. The local jump in aerodynamic force makes the asymmetric IGVs difficult to design (due to large circumferential gradients in IGVs exit angles) and ineffective. However, the straight IGVs used are unrealistic for a real fan. Moreover, the results for the case with inlet distortion and straight IGVs strongly suggest that the straight IGVs itself can significantly attenuates the impact of inlet distortion, at least at low speed, on the fan through limited local flow redistribution near the edges of the distortion region. However, straights IGVs do not seem to be so effective for high-speed fans.

Based on the findings from this research, three recommendations can be made for future work. The first is to develop a method to optimize a 3D design of asymmetric IGVs to maximize its effectiveness. This method would require a much faster simulation tool than standard CFD simulations even in inviscid mode. One possibility is to validate the body force model proposed by Hall *et al*. [18] for fans operating at transonic speeds and/or with lower blade count and, if successful, to use this model in optimization loop.

The second recommendation is to validate the concept on a fan test rig with relatively high tip speed so that the variation in aerodynamic blade force and rotor exit total pressure distribution

under inlet distortion is significant enough to be measured and to represent realistic fan inlet condition operating conditions.

The third recommendation is to design the asymmetric IGVs with more spans, especially near the blade tip, to achieve finer control.

The final recommendation is to investigate further the use of straight IGVs in high-speed fans to explain why they are not as effective for high-speed fans even though they seem to significantly reduce local flow redistribution.

REFERENCES

[1] Tony, T. (2014). The International Air Transport Association: Annual Review 2014 [PowerPoint slides]: Retrieved from https://www.iata.org/about/Documents/iata-annual-review-2014.pdf

[2] Fan, A. (2010). An Assessment of Environmental Impacts of A NextGen Implementation Scenario and Its Implications on Policy-Making (Master thesis, Massachusetts Institute of Technology, Cambridge, USA).

[3] Smith, L. H. (1993). Wake Ingestion Propulsion Benefit. Journal of Propulsion and Power, 9(1), 74-82.

[4] Sato, S. (2012). The Power Balance Method for Aerodynamic Performance Assessment. (Doctoral dissertation, Massachusetts Institute of Technology, Cambridge, USA).

[5] Hall, D. K. (2015). Analysis of Civil Aircraft Propulsors with Boundary Layer Ingestion. (Doctoral dissertation, Massachusetts Institute of Technology, Cambridge, USA).

[6] Drela, M. (2009). Power Balance in Aerodynamic Flows. AIAA journal, 47(7), 1761-1771.

[7] Van Dam, E. M. (2015). Inlet Distortion Characterization of the Boundary Layer Ingesting D8 Aircraft, (Master's thesis, Delft University of Technology, Netherlands).

[8] Hall, D. K., Huang, A. C., Uranga, A., Greitzer, E. M., Drela, M., and Sato, S. (2017). Boundary Layer Ingestion Propulsion Benefit for Transport Aircraft. Journal of Propulsion and Power, 1-12.

[9] Hall, C. A., and Crichton, D. (2005). Engine and Installation Configurations for A Silent Aircraft. ISABE, 1164, 2005.

[10] Diedrich, A., Hileman, J., Tan, D., Willcox, K., and Spakovszky, Z. (2006, January). Multidisciplinary Design and Optimization of the Silent Aircraft. In 44th AIAA Aerospace Sciences Meeting and Exhibit (p. 1323).

[11] Hileman, J. I., Spakovszky, Z. S., Drela, M., Sargeant, M. A., and Jones, A. (2010). Airframe Design for Silent Fuel-Efficient Aircraft. Journal of aircraft, 47(3), 956-969.

[12] Hardin, L., Tillman, G., Sharma, O., Berton, J., and Arend, D. (2012). Aircraft System Study of Boundary Layer Ingesting Propulsion. In 48th AIAA/ASME/SAE/ASEE Joint Propulsion Conference and Exhibit (p. 3993).

[13] Uranga, A., Drela, M., Greitzer, E. M., Titchener, N. A., Lieu, M. K., Siu, N. M., Hannon, J. A. (2014). Preliminary Experimental Assessment of the Boundary Layer Ingestion Benefit for the D8 Aircraft. Paper AIAA 2014-0906, in proceedings of the 52th AIAA Aerospace Sciences Meeting, National Harbor, MD, USA (pp. 1-25).

[14] Lord, W., MacMartin, D., and Tillman, G. (2000). Flow Control Opportunities in Gas Turbine Engines. In Fluids 2000 Conference and Exhibit (p. 2234).

[15] AMO Smith. (1947). The Jet Airplane Utilizing Boundary Layer Air for Propulsion. Journal of the Aeronautical Sciences, 14(2), 97-109.

[16] Florea, R. V., Matalanis, C., Hardin, L. W., Stucky, M., and Shabbir, A. (2015). Parametric Analysis and Design for Embedded Engine Inlets. Journal of Propulsion and Power, 31(3), 843-850.

[17] Hall, D. K., Greitzer, E. M., and Tan, C. S. (2017). Analysis of Fan Stage Conceptual Design Attributes for Boundary Layer Ingestion. Journal of Turbomachinery, 139(7), 071012.

[18] Defoe, J.J. and Hall, D.K. (2016). Fan Performance Scaling with Inlet Distortions. Paper GT2016-58009, in proceedings of ASME Turbo Expo 2016, Seoul, South Korea.

[19] Gunn, E. J., and Hall, C. A. (2014, June). Aerodynamics of Boundary Layer Ingesting Fans. In ASME Turbo Expo 2014: Turbine Technical Conference and Exposition (pp. V01AT01A024-V01AT01A024). American Society of Mechanical Engineers.

[20] Owens, L. R., Allan, B. G., and Gorton, S. A. (2008). Boundary-Layer-Ingesting Inlet Flow Control. Journal of Aircraft, 45(4), 1431-1440.

[21] Bakhle, M., Reddy, T. S. R., Herrick, G., Shabbir, A., and Florea, R. (2012, July). Aeromechanics Analysis of a Boundary Layer Ingesting Fan. In 48th AIAA/ASME/SAE/ASEE Joint Propulsion Conference and Exhibit (p. 3995).

[22] Aeromechanics Analysis of a Boundary Layer Ingesting Fan Boundary Layer Ingesting Fan in NASA-Glenn's 8-Foot by 6-Foot Transonic Wind Tunnel.

Retrieved from

http://www.utrc.utc.com/20170316_UTRC%20and%20NASA%20successfully%20test%20the%20worlds%20first%20boundary%20layer%20ingesting%20fan%20for%20jet%20engines%20.html

[23] Conrad, E. W., and Sobolewski, A. E. (1950). Investigation of Effects of Inlet-Air Velocity Distortion on Performance of Turbojet Engine.

[24] Conrad, E. W., Hanson, M. P., and McAulay, J. E. (1955). Effect of Inlet-Air-Flow Distortion on Steady-State Altitude Performance of An Axial-Flow Turbojet Engine.

[25] Atinault, O., Carrier, G., Grenon, R., and Verbecke, C. (2013). Numerical and Experimental Aerodynamic Investigations of Boundary Layer Ingestion for Improving Propulsion Efficiency of Future Air Transport. In 31st AIAA Applied Aerodynamics Conference (p. 2406).

[26] Pearson, H., and McKenzie, A. (1959). Wakes in Axial Compressors. The Journal of the Royal Aeronautical Society, 63(583), 415-416. doi:10.1017/S0368393100071273.

[27] Davis, M. W., and Cousins, W. T. (2011, January). Evaluating Complex Inlet Distortion with A Parallel Compressor Model: Part 2—Applications to Complex Patterns. In ASME 2011 Turbo Expo: Turbine Technical Conference and Exposition (pp. 13-23). American Society of Mechanical Engineers.

[28] Gong, Y. (1999). A Computational Model for Rotating Stall and Inlet Distortions in Multistage Compressors (Doctoral dissertation, Massachusetts Institute of Technology).

[29] Gong, Y., Tan, C. S., Gordon, K. A., and Greitzer, E. M. (1998). A Computational Model for Short Wavelength Stall Inception and Development in Multi-stage Compressors. In ASME 1998 International Gas Turbine and Aeroengine Congress and Exhibition (pp. V001T01A114-V001T01A114). American Society of Mechanical Engineers.

[30] Yao, J., Gorrell, S. E., and Wadia, A. R. (2010). High-Fidelity Numerical Analysis of Per-Rev-Type Inlet Distortion Transfer in Multistage Fans—Part I: Simulations with Selected Blade Rows. Journal of Turbomachinery, 132(4), 041014.

[31] Jerez-Fidalgo, V, Hall, C.A., and Colijn, Y. (2012). A Study of Fan-Distortion Interaction Within the NASA Rotor 67 Transonic Stage. Journal of Turbomachinery, 134(3), 051011.

[32] Andraos, A., Belaïd, E., Drai, A., Duranleau-Hendrickx, L., Fandoux, C., Grézaud, P., Lavallée, C., Le Brasseur, S., Maréchal, J., Pépin, K., Saives, A., Samson, B. and Tremblay, S. (2019), AER8875 – Projet intégrateur IV en génie aérospatial, Rapport de design – Livrable B, Design Report, Polytechnique Montréal.

[33] Rediniotis, O., Bowersox, R., Kirk, A., Kumar, A., & Tichenor, N. (2007). Active control of jet engine inlet flows. Texas Engineering Experiment Station College Station.

[34] https://grabcad.com/library/nasa-rotor-67-1

[35] Strazisar, A. J., Hathaway, M. D., Suder, K. L., & Wood, J. R. (1989). Laser anemometer measurements in a transonic axial-flow fan rotor. NASA Lewis Research Center.

APPENDIX A POST-PROCESSING PROCEDURE

A.1 OUTPUT PARAMETERS CALCULATION

The post-processing is made by using ANSYS CFD-*Post*. Some specified expressions need to be edited.

Total Pressure Ratio is defined with the expression:

$$\frac{massFlowAve(Total\ Pressure\ in\ Stn\ Frame)@Plane\ 2}{massFlowAve(Total\ Pressure\ in\ Stn\ Frame)@Plane\ 1} \tag{A.1}$$

Blade force is defined with the expression:

$$\sqrt{force\_x()@blade1^2 + force\_y()@blade1^2 + force\_z()@blade1^2} \tag{A.2}$$

Relative velocity is defined with the expression:

$$\sqrt{(\Omega \times R - (Velocity\ in\ Stn\ Frame\ Circumferential))^2 + (Velocity\ in\ Stn\ Frame\ w)^2} \tag{A.3}$$

Relative angle is defined with the expression:

$$\tan^{-1}\left(\frac{\Omega \times R - Velocity\ in\ Stn\ Frame\ Circumferential}{|Velocity\ in\ Stn\ Frame\ w|}\right) \tag{A.4}$$

Absolute swirl angle is defined with the expression:

$$\text{atan}\left(\frac{Velocity\ in\ Stn\ Frame\ Circumferenctial}{Velocity\ in\ Stn\ Frame\ w}\right) \tag{A.5}$$

Corrected mass flow is defined by:

$$\dot{m}_c = \frac{\dot{m}\sqrt{\frac{T_{amb}}{288.15\ K}}}{\frac{P_{amb}}{101325\ Pa}} \tag{A.6}$$

A.2 EQUATIONS FOR CONTROL VOLUME ANALYSIS

Figure A-1 is a schematic diagram of the control volume in the $x - \theta$ plane. The variables involved in the blade force equation are, pressure, axial velocity, circumferential velocity, density at rotor LE, and area. The blade force per unit square meter are calculated according to the conservation of momentum equation.

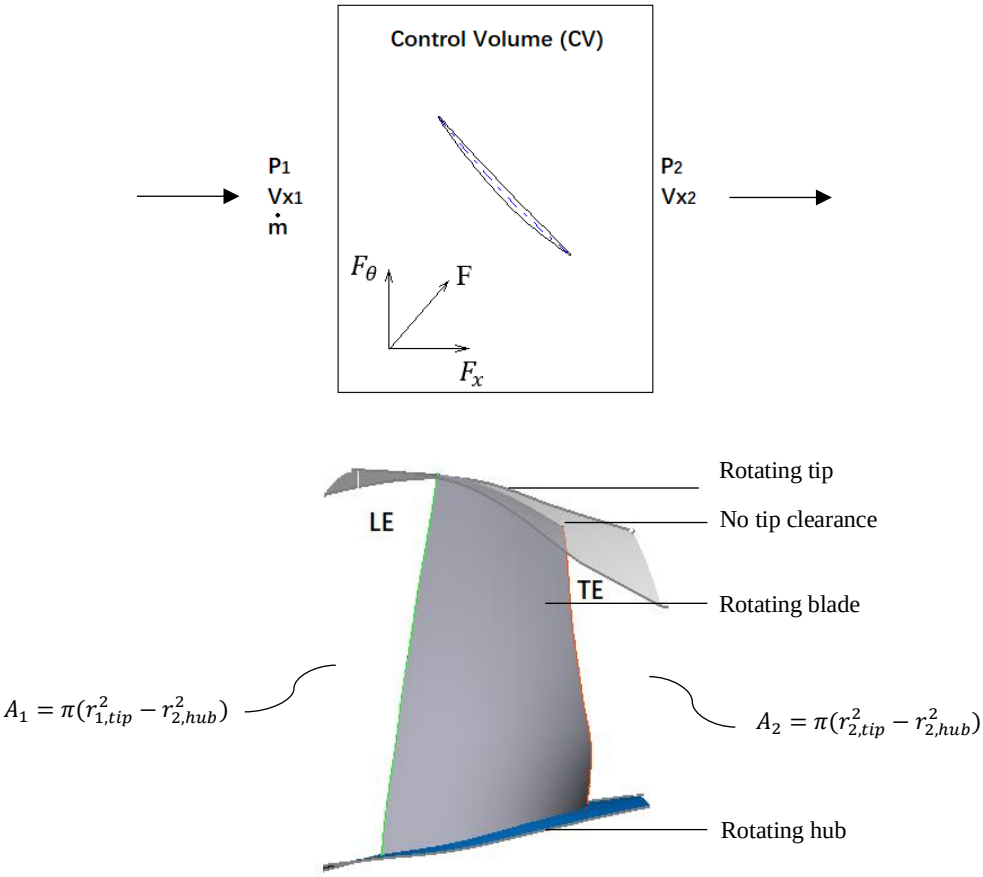

Figure A-1 Control volume

Conservation of Momentum Equation,

In x-direction:

$$\sum_{CV} F_x = \oint_{CV} V_x d\dot{m} \tag{A.7}$$

$$\int P_1 dA_1 - \int P_2 dA_2 - F_{hub\&shroud} + F_x = -\int V_{x1} d\dot{m} + \int V_{x2} d\dot{m} \tag{A.8}$$

$$A_1 P_1 - A_2 P_2 - F_{hub\&shroud} + F_x = -\dot{m}_x \overline{V_{x1}^{\dot{m}}} + \dot{m}_x \overline{V_{x2}^{\dot{m}}} \tag{A.9}$$

$$\dot{m} = A_1 \rho_1 V_{x1} \tag{A.10}$$

$$F_{hub\&shroud} = \frac{(P_1+P_2)}{2}(A_1 - A_2) \tag{A.11}$$

$$F_x = A_1 \rho_1 V_{x1}(V_{x2} - V_{x1}) + P_2 A_2 - A_1 P_1 + \frac{(P_1+P_2)}{2}(A_1 - A_2) \tag{A.12}$$

$$\frac{F_x}{A_1} = \rho_1 V_{x1}(V_{x2} - V_{x1}) + P_2 \frac{A_2}{A_1} - P_1 + \frac{P_1+P_2}{2}\left(1 - \frac{A_2}{A_1}\right) \tag{A.13}$$

In θ-direction:

$$\sum_{CV} F_\theta = \oint V_\theta d\dot{m} \tag{A.14}$$

$$F_\theta = -\int V_{\theta 1} d\dot{m} + \int V_{\theta 2} d\dot{m} \tag{A.15}$$

$$F_\theta = \dot{m}(\overline{V_{\theta 2}^{m}} - \overline{V_{\theta 1}^{m}}) \tag{A.16}$$

$$\frac{F_\theta}{A_1} = \rho_1 V_{x1}(V_{\theta 2} - V_{\theta 1}) \tag{A.17}$$

$$\frac{F}{A_1} = \sqrt{(\frac{F_x}{A_1})^2 + (\frac{F_\theta}{A_1})^2} \tag{A.18}$$

APPENDIX B LOW-SPEED FAN ROTOR

B.1 ASYMMETRIC IGVS DESIGN ITERATIONS

Tables B-1 through B-3 list the exit blade angles for the three asymmetric IGVs design iterations for the low-speed rotor. The blade number represents the coordinate position of the blade in Figure 4.12. The blade starts at 3 o'clock position and counts counterclockwise.

Table B-1 First Asymmetric IGVs design iteration for low-speed fan rotor

Blade No.	1	2	3	4	5	6	7	8	9	10	11	12	13	14	15	16	17	18	19	20
tip	0	1	1	3	3	7	7	10	10	14	14	10	10	-10	-10	-30	-30	-30	-30	0
75% span	0	1	1	3	3	7	7	10	10	14	14	6	6	-9	-9	-26	-26	-22	-22	0
50% span	0	1	1	3	3	7	7	10	10	14	14	5	5	-5	-5	-16	-16	-16	-16	0
25% span	0	1	1	3	3	7	7	10	10	14	14	3	3	-3	-3	-11	-11	-10	-10	0
hub	0	1	1	3	3	6	6	10	10	14	14	2	2	-2	-2	-6	-6	-6	-6	0

[deg]

Table B-2 Second Asymmetric IGVs design iteration of low-speed fan rotor

Blade No.	1	2	3	4	5	6	7	8	9	10	11	12	13	14	15	16	17	18	19	20
tip	-5	1	1	3	3	7	7	10	10	14	14	25	25	-2	-2	-29	-29	-37	-37	-5
75% span	-5	1	1	3	3	7	7	10	10	14	14	18	18	-2	-2	-25	-25	-28	-28	-5
50% span	-5	1	1	3	3	7	7	10	10	14	14	14	14	-1	-1	-14	-14	-19	-19	-5
25% span	-5	1	1	3	3	7	7	10	10	14	14	8	8	0	0	-10	-10	-15	-15	-5
hub	-5	1	1	3	3	6	6	10	10	14	14	5	5	0	0	-5	-5	-10	-10	-5

[deg]

Table B-3 Third Asymmetric IGVs design iteration of low-speed fan rotor

Blade No.	1	2	3	4	5	6	7	8	9	10	11	12	13	14	15	16	17	18	19	20
tip	-3	1	1	3	3	7	7	10	10	13	13	20	20	-5	-5	-27	-27	-34	-34	-3
75% span	-3	1	1	3	3	7	7	10	10	13	13	16	16	-5	-5	-23	-23	-26	-26	-3
50% span	-3	1	1	3	3	7	7	10	10	13	13	14	14	-4	-4	-13	-13	-17	-17	-3
25% span	-3	1	1	3	3	7	7	10	10	13	13	8	8	-3	-3	-9	-9	-13	-13	-3
hub	-3	1	1	3	3	6	6	10	10	13	13	5	5	-2	-2	-5	-5	-8	-8	-3

[deg]

B.2 TIME STEP STUDY

In Figure B-1 shows the result of the time step study for the low-speed fan rotor. It indicates that a setting of 20 time steps per rotor blade passing is adequate.

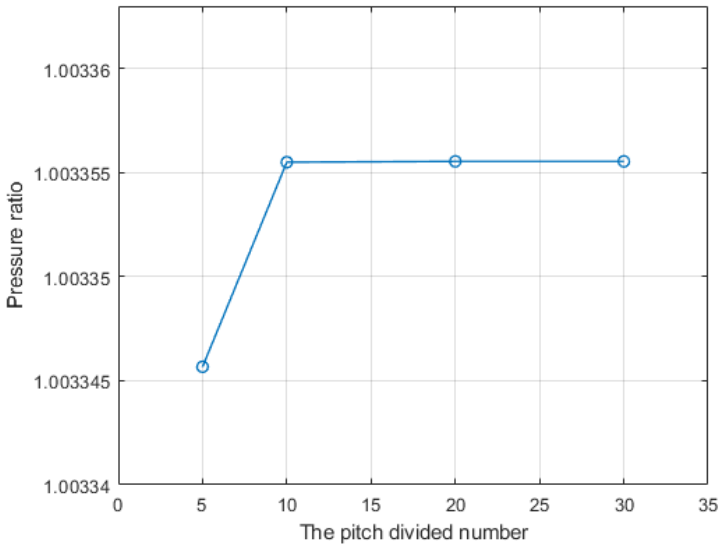

Figure B-1 Total pressure ratio versus number of time step per blade passing for low-speed fan rotor

B.3 CONTROL VOLUME ANALYSIS

This section presents the input and detailed output of the control volume analysis as detailed in appendix A (section A.2) for the low-speed rotor. The black and red lines in the figures represent the fan parameters without IGVs and with asymmetric IGVs, respectively. The solid and dotted lines represent parameters at the rotor LE and rotor TE, respectively. Figures B-2 through B-5 show the input to the analysis, namely the circumferential distributions of static pressure, axial velocity, circumferential velocity and density at different span as extracted from the CFD predictions. Figures B-6 and B-7 plot the resulting axial and circumferential blade loading from the control volume analysis. Their combination according to equation (A.18) gives the total blade loading distributions in Figure 4.14.

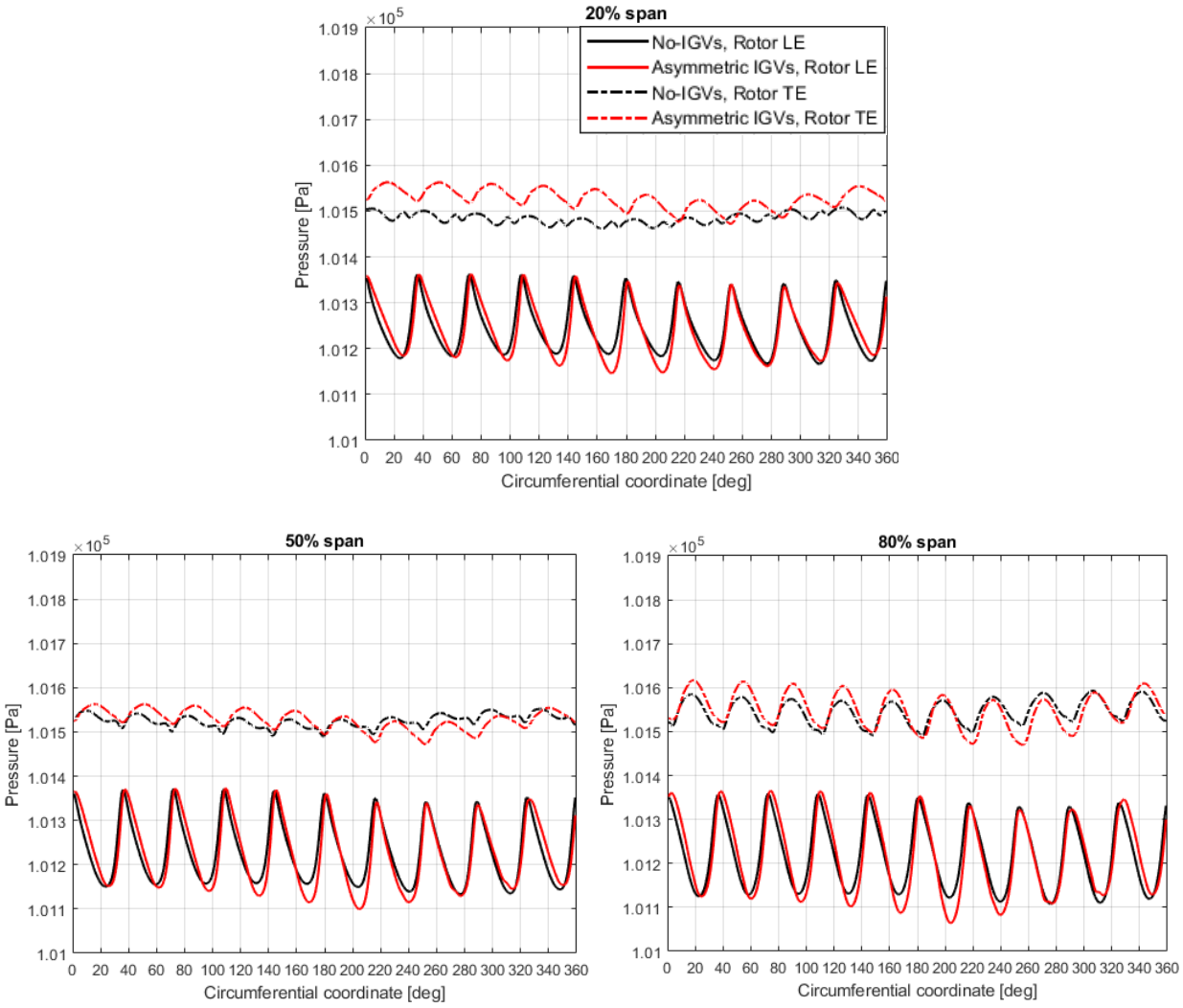

Figure B-2 Static pressure at rotor LE and TE for 20%, 50% and 80% spans

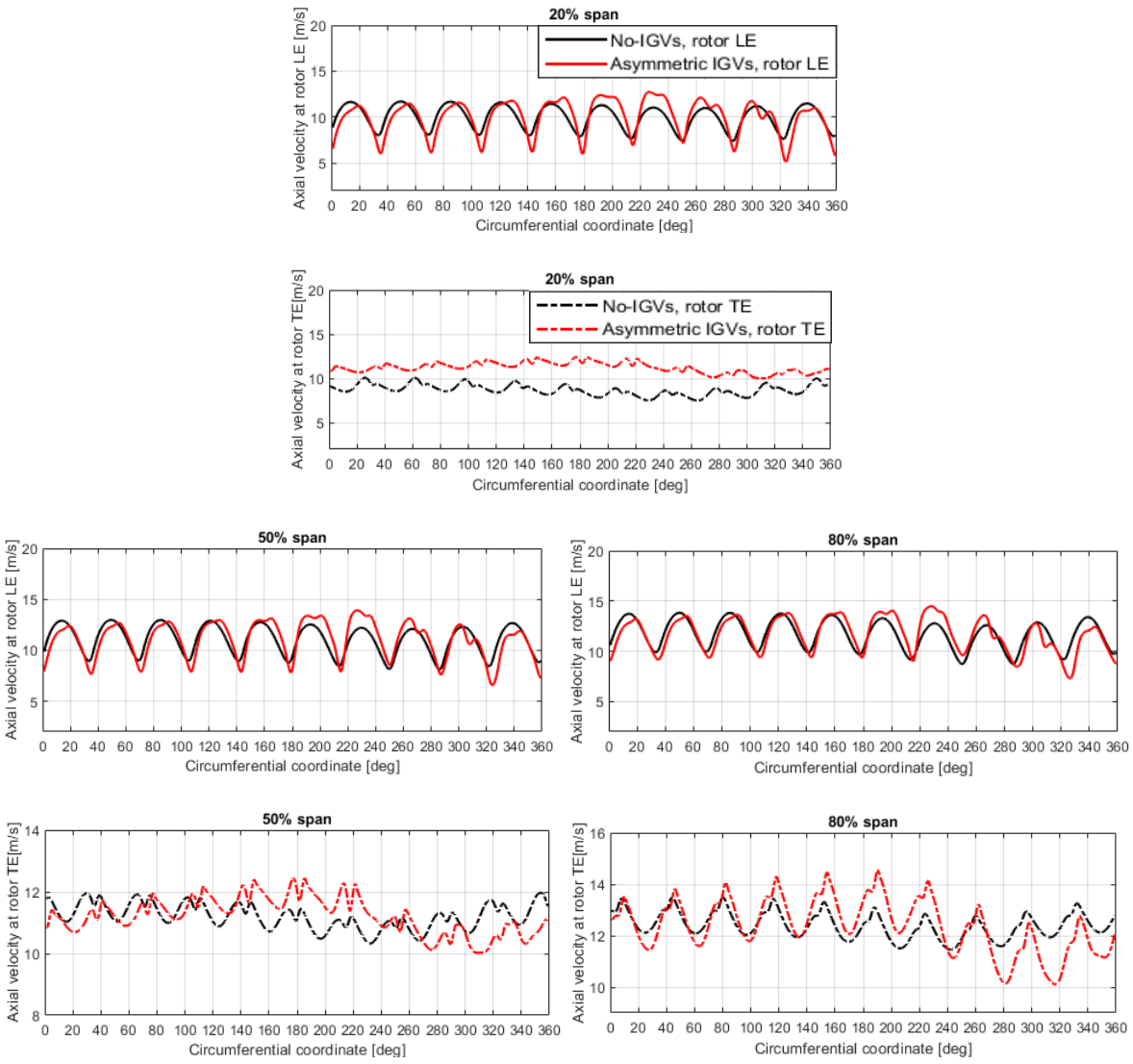

Figure B-3 Axial velocity at rotor LE and TE for 20%, 50% and 80% spans

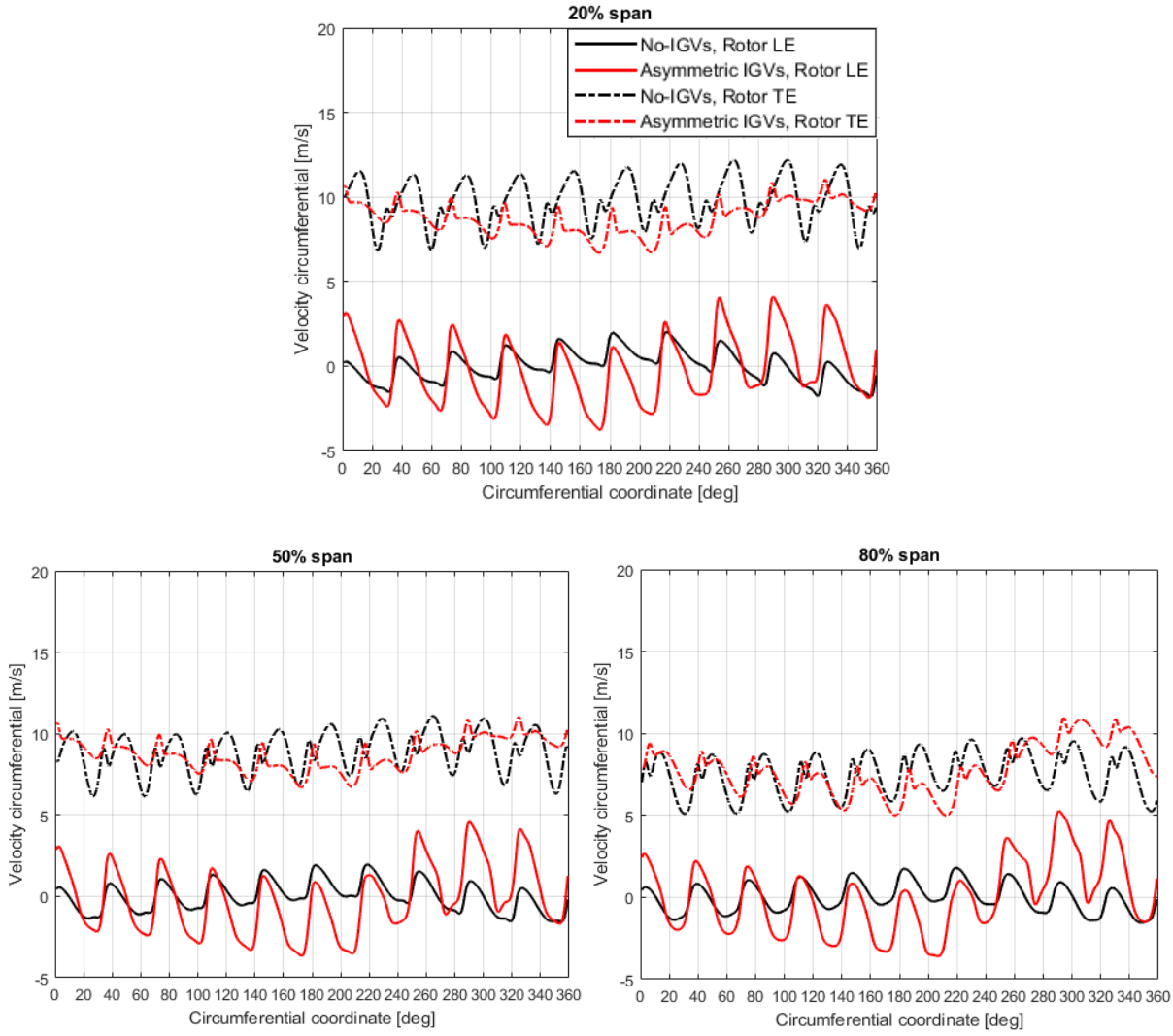

Figure B-4 Circumferential velocity in stationary frame at rotor LE and TE for 20%, 50% and 80% spans

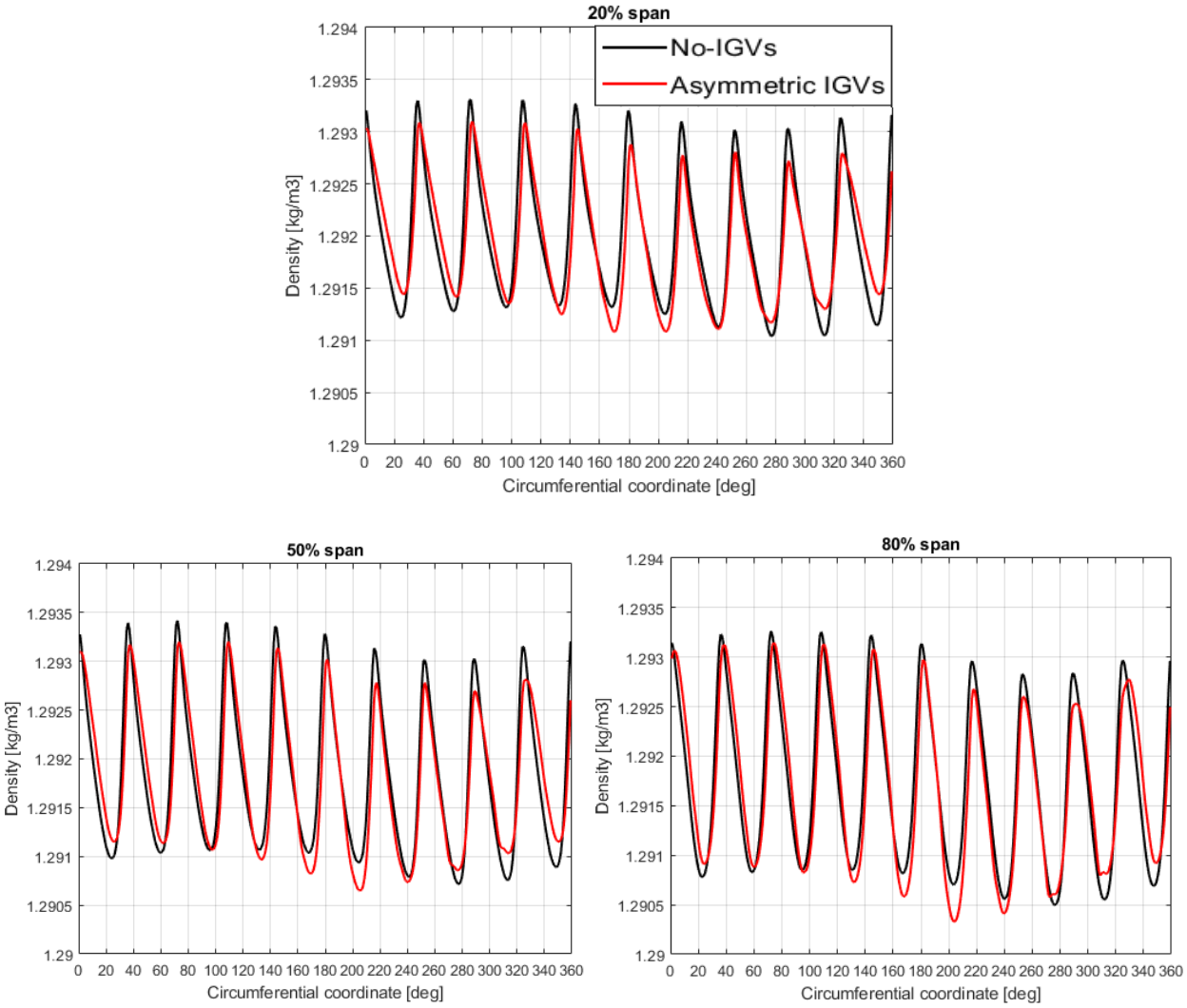

Figure B-5 Density at rotor LE for 20%, 50% and 80% spans

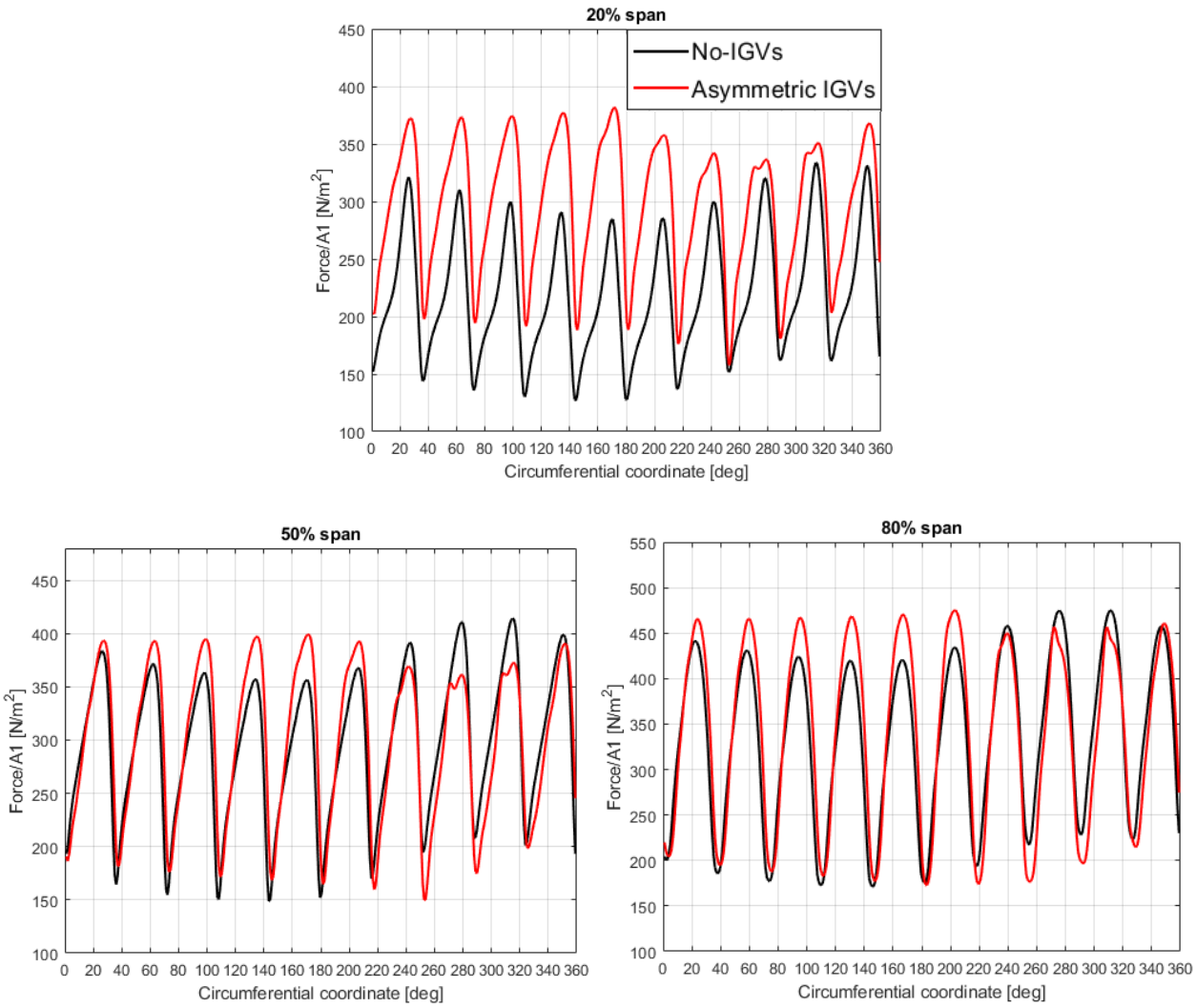

Figure B-6 Axial blade force per square meter in upstream direction for 20%, 50% and 80% spans

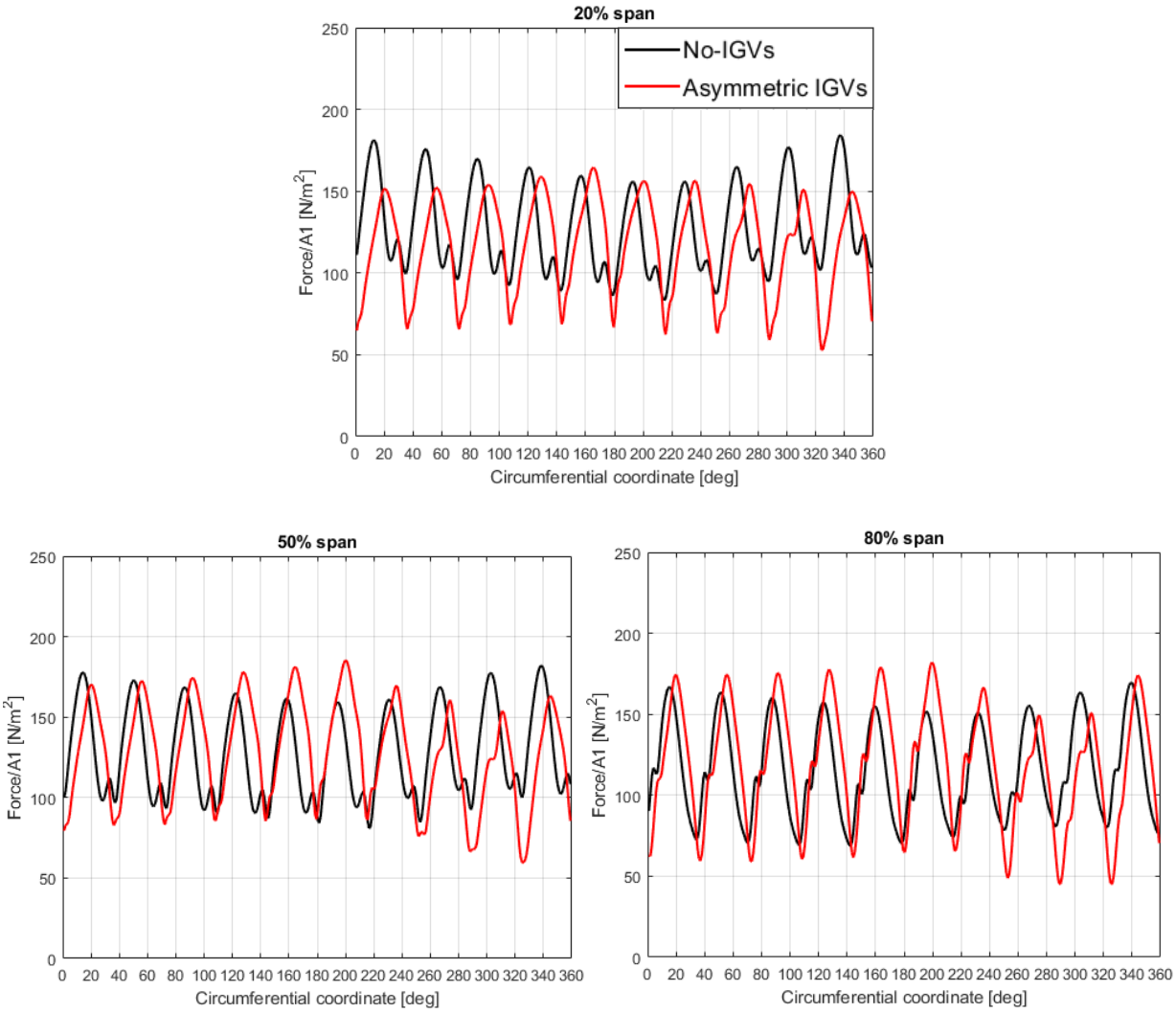

Figure B-7 Circumferential blade force per square meter opposite rotation direction for 20%, 50% and 80% spans

B.4 EFFECT OF USING TOTAL VERSUS STATIC TEMPERATURE INLET BOUNDARY CONDITIONS

To validate the choice of the a static temperature inlet boundary condition used in the high-speed fan rotor, simulations with and without distortion without IGVs are carried out on the low-speed fan rotor with this boundary condition and compared to the equivalent simulations with the total temperature inlet boundary condition presented in Chapter 4. Figures B-9 and B-10 compares the blade aerodynamic force variation and the rotor exit total pressure contours (with distortion),

respectively. These results indicate that the change from total to static inlet temperature boundary conditions have negligible effects on the parameters relevant to the current study.

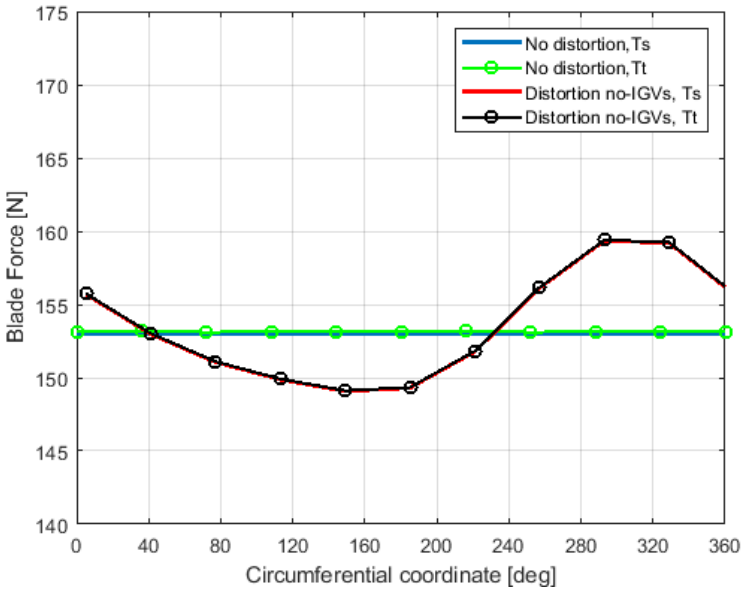

Figure B-9 Effect of different temperature inlet boundary conditions on blade force for low-speed fan rotor

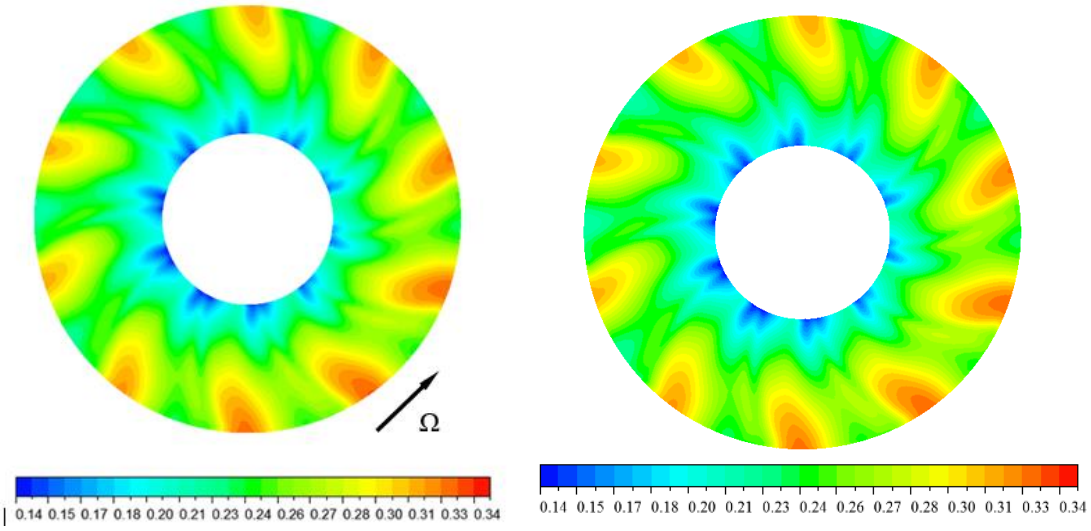

Total temperature inlet boundary condition Static temperature inlet boundary condition

B-10 Total pressure at rotor TE without IGV

APPENDIX C HIGH-SPEED FAN ROTOR

C.1 ASYMMETRIC IGVS DESIGN ITERATIONS

Tables C-1 the exit blade angles for the three asymmetric IGVs design iterations for the high-speed rotor. The blade number represents the coordinate position of the blade in Figure 5.11. The blade starts at 3 o'clock position and counts counterclockwise.

Table C-1 Asymmetric IGVs design iterations of high-speed fan rotor

	Blade No.	1	2	3	4	5	6	7	8	9	10	11	12	13	14	15	16	17	18	19	20	21
Iteration 1	Exit angle [deg]	5	5	5	5	5	5	5	5	5	5	5	6	7	6	5	3	2	2	0	-1	3
Iteration 2	Exit angle [deg]	3.8	3.5	4.9	4.4	4.9	5	5	5	5	5.1	5.7	7.3	13	11	4	1	0.5	0	-1	-2	1.4
Iteration 3	Exit angle [deg]	2	2	4.9	4.4	4.9	5	5	5	5	5.1	6	10	21	14	3	-2	-4	-4	-6	-6	-4

C.2 TIME STEP STUDY

In Figure C-1 shows the result of the time step study for Rotor 67. It indicates that a time a setting of 20 time steps per rotor blade passing is adequate.

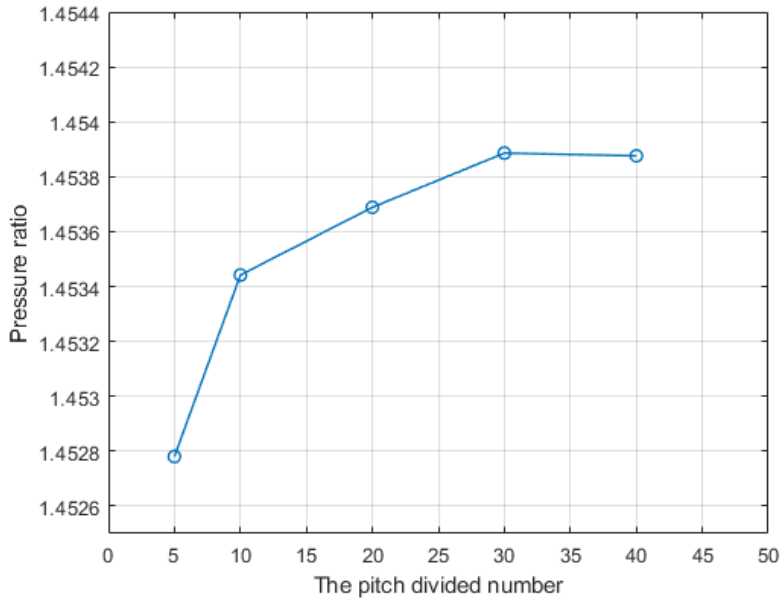

Figure C-1 Total pressure ratio versus number of time step per blade passing for Rotor 67

C.3 CONTROL VOLUME ANALYSIS

This section presents the input and detailed output of the control volume analysis as detailed in appendix A (section A.2) for the high-speed rotor. The black and red lines in the figures represent the fan parameters without IGVs and with asymmetric IGVs, respectively. The solid and dotted lines represent parameters at the rotor LE and rotor TE, respectively. Figures C-2 through C-5 show the input to the analysis, namely the circumferential distributions of static pressure, axial velocity, circumferential velocity and density at different span as extracted from the CFD predictions. Figures C-6 and C-7 plot the resulting axial and circumferential blade loading from the control volume analysis. Their combination according to Equation (A.18) gives the total blade loading distributions in Figure 5.13.

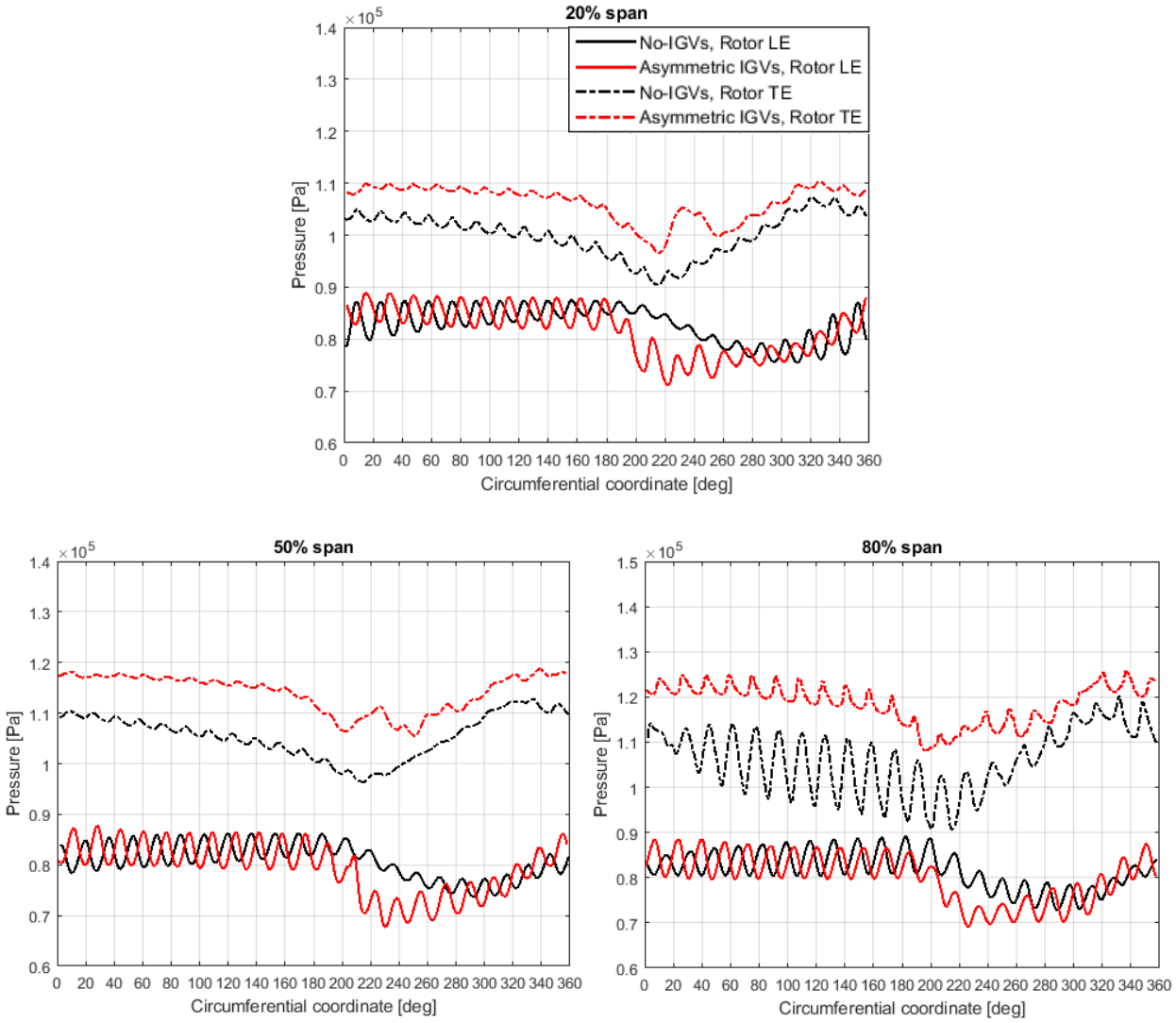

Figure C-2 Static pressure at Rotor 67 LE and TE for 20%, 50% and 80% spans

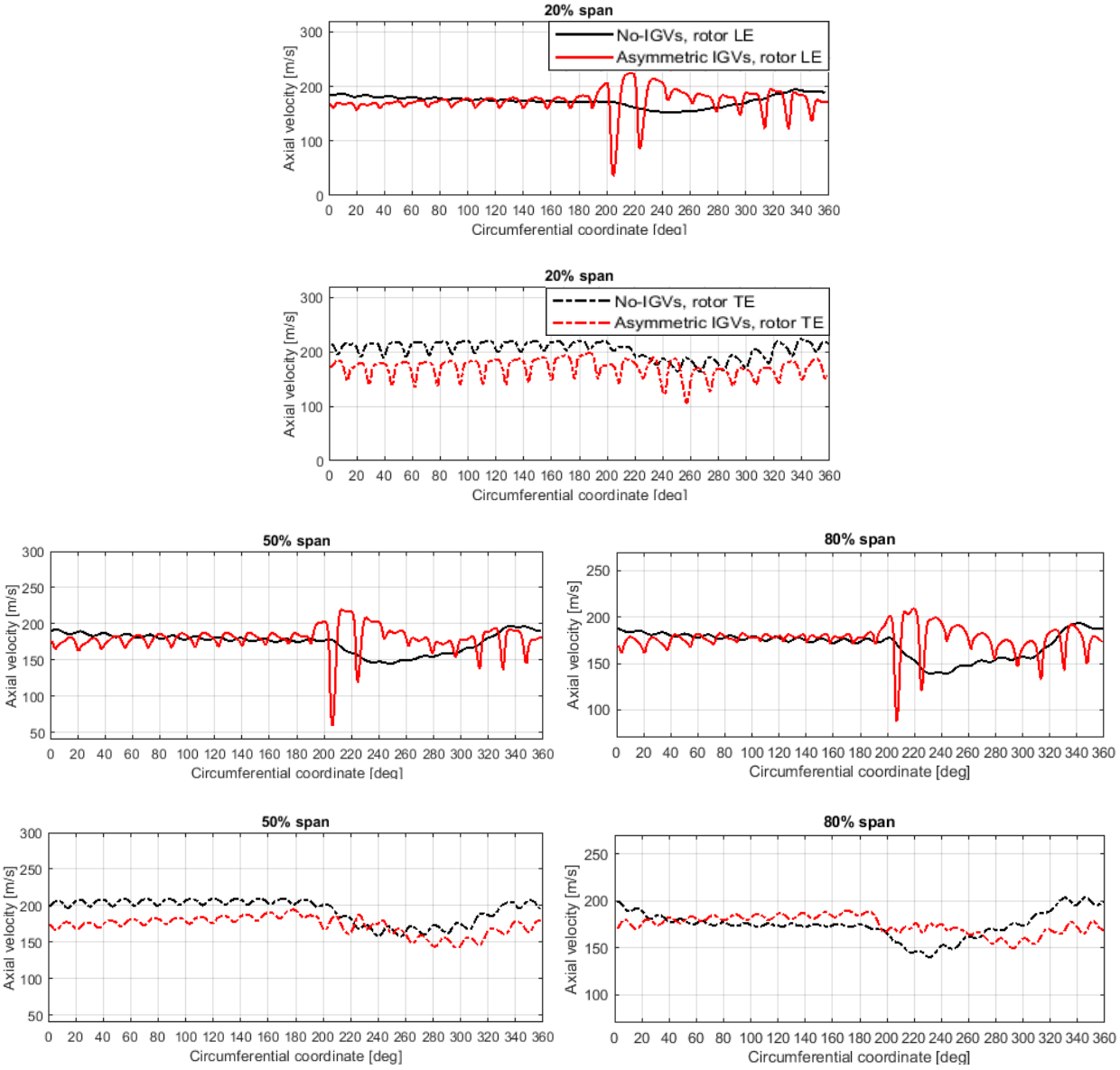

Figure C-3 Axial velocity at Rotor 67 LE and TE for 20%, 50% and 80% spans

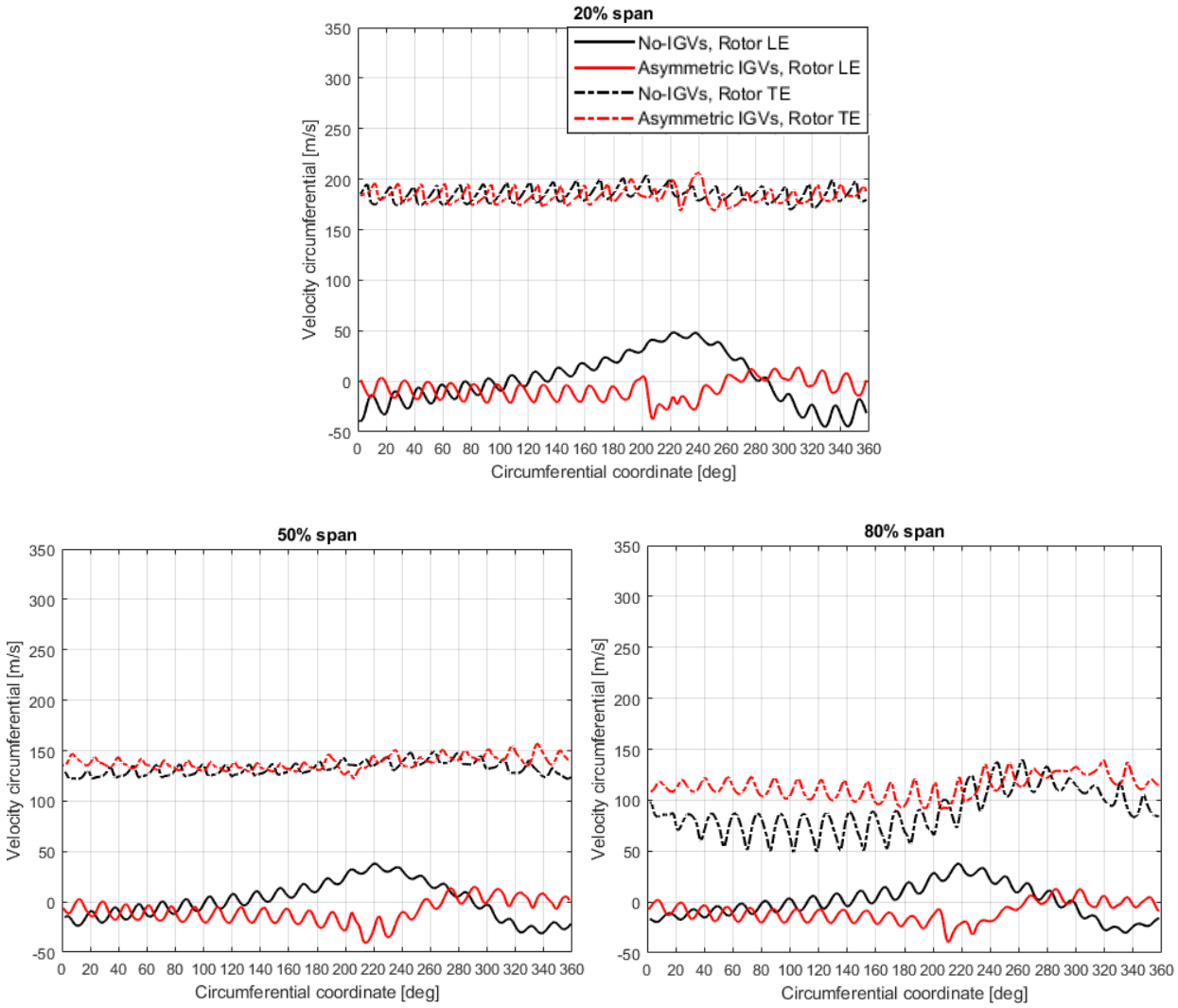

Figure C-4 Circumferential velocity in stationary frame at Rotor 67 LE and TE for 20%, 50% and 80% spans

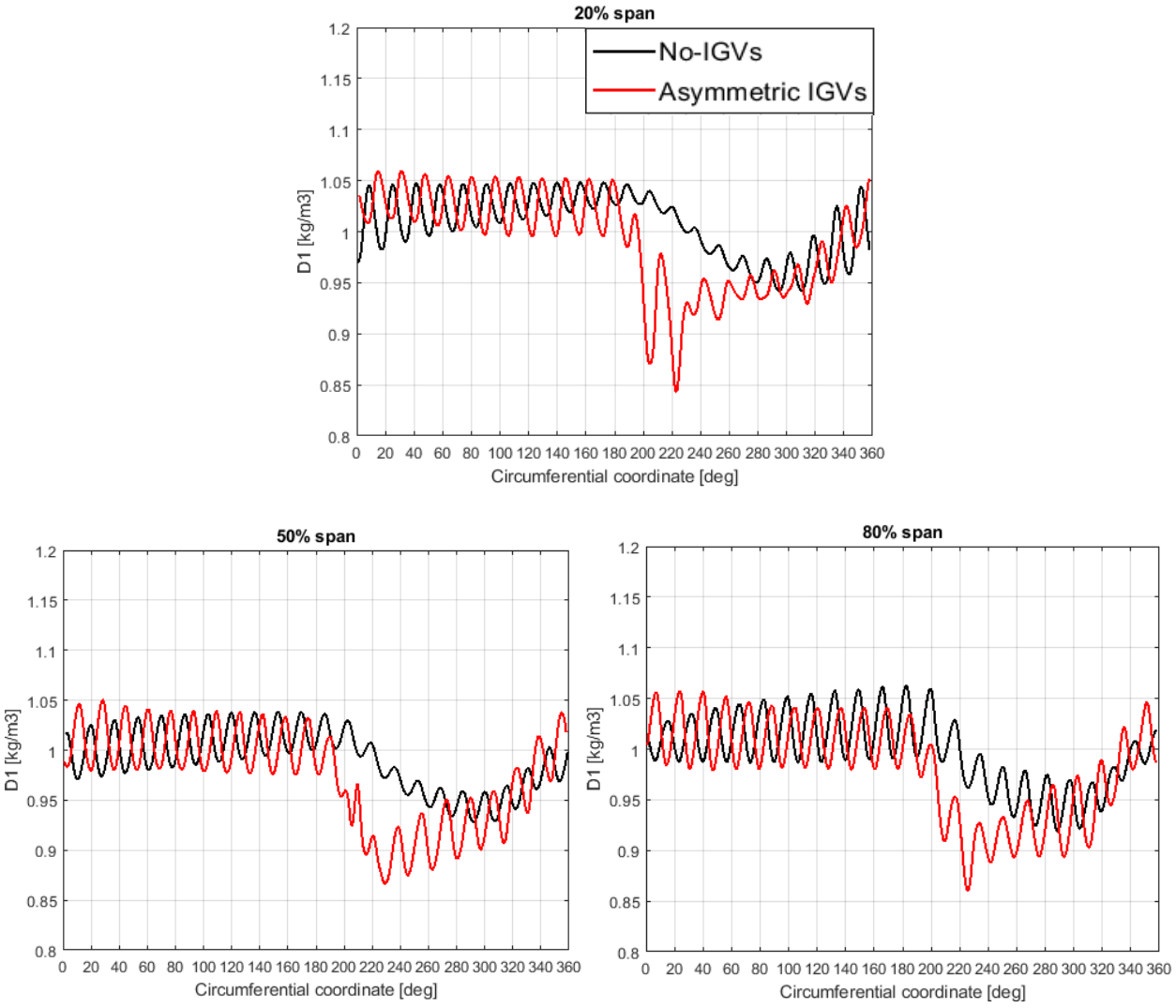

Figure C-5 Density at Rotor 67 LE for 20%, 50% and 80% spans

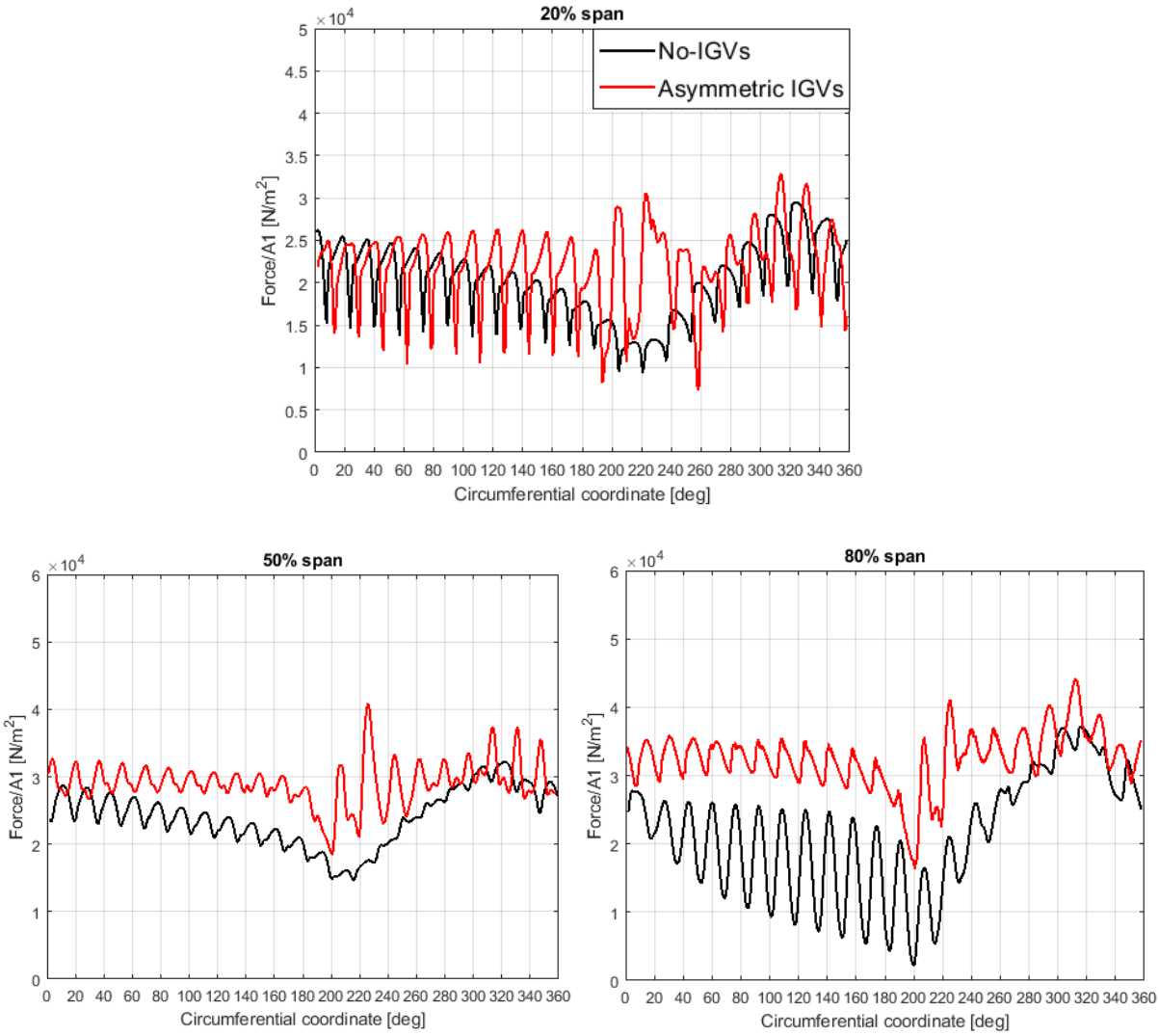

Figure C-6 Axial blade force per square meter in upstream direction for 20%, 50% and 80% spans

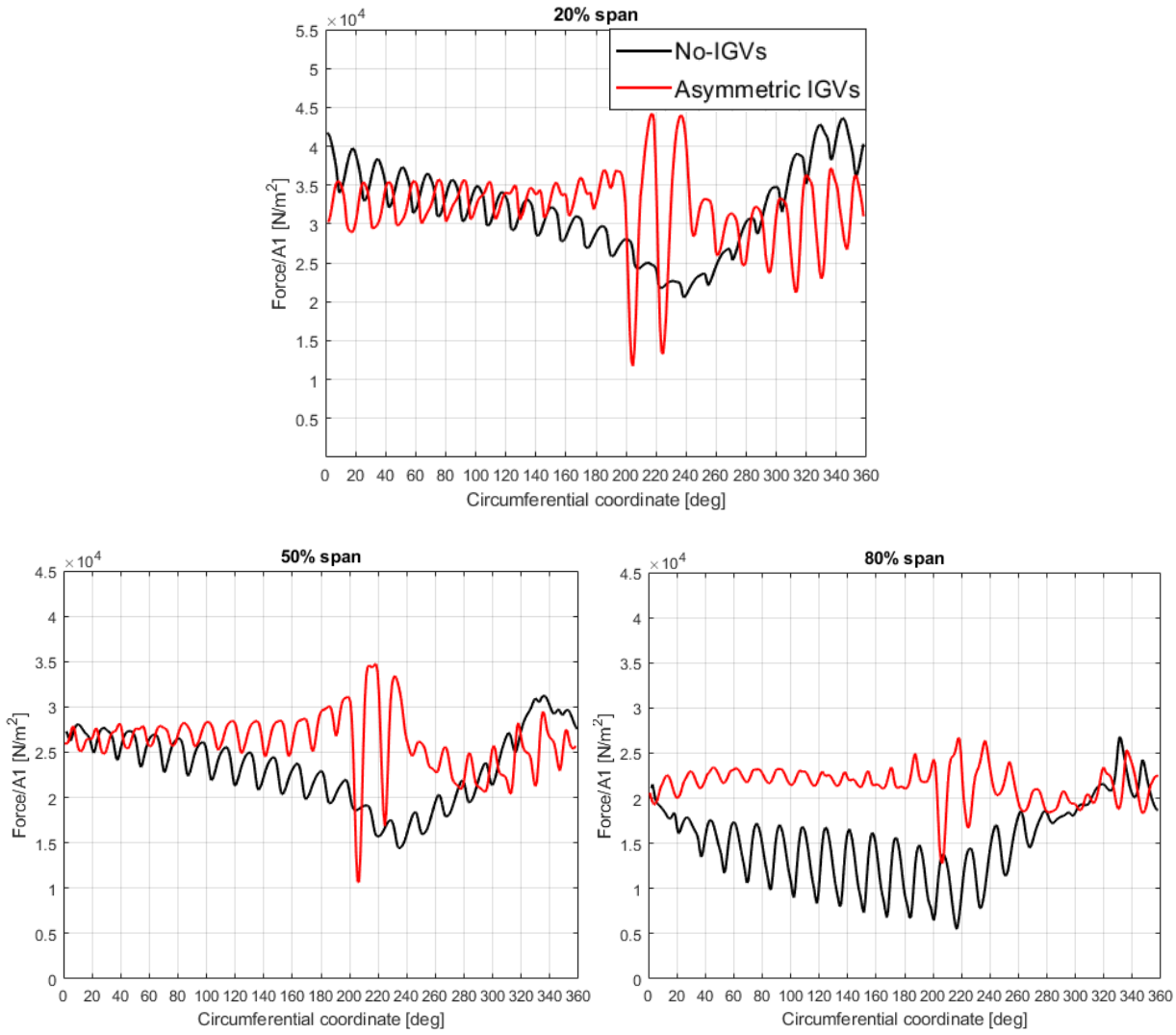

Figure C-17 Circumferential blade force per square meter opposite rotation direction at 20%, 50% and 80% spans

C.4 ESTIMATE OF FAN PERFORMANCE WITH VISCOUS IGV

A steady single-blade-passage simulation is carried out with IGVs trailing edge angle of 21 deg. and $\dot{m}_{outlet} = 1.4647\ kg/s$ to estimate the loss of the fan, as shown in Figure C-9. The result in Table C-2 shows that viscous loss of the IGVs affects fan performance slightly.

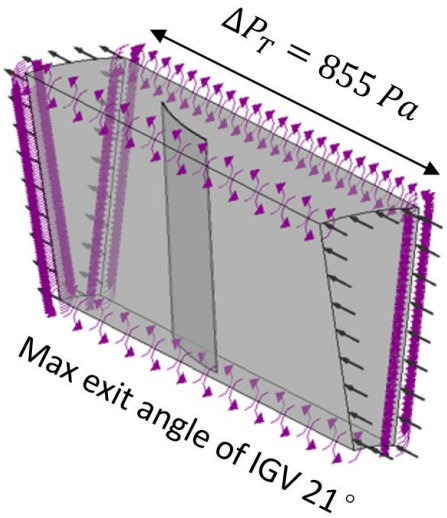

Figure C-9 Computational domain of the single-blade-passage

Table C-2 Effect on fan performance

	NO DISTORTION	DISTORTION WITHOUT IGV	DISTORTION WITH INVISCID IGV	DISTORTION WITH VISCOUS IGV
TOTAL PRESSURE RATIO	1.5254	1.3680	1.4590	1.4506

C.5 EFFECTIVENESS OF STRAIGHT IGVS

Figure C-11 presents the contours of absolute flow angle at the high-speed rotor LE with and without straight IGVs. The result indicates that the straight IGVs signficantly reduce local flow redistribution at the edge of the distortion region. However, Figure C-10 shows that the straight IGVs are much less effective than the asymmetric IGVs in attenuating the variation in blade force due to inlet distortion.

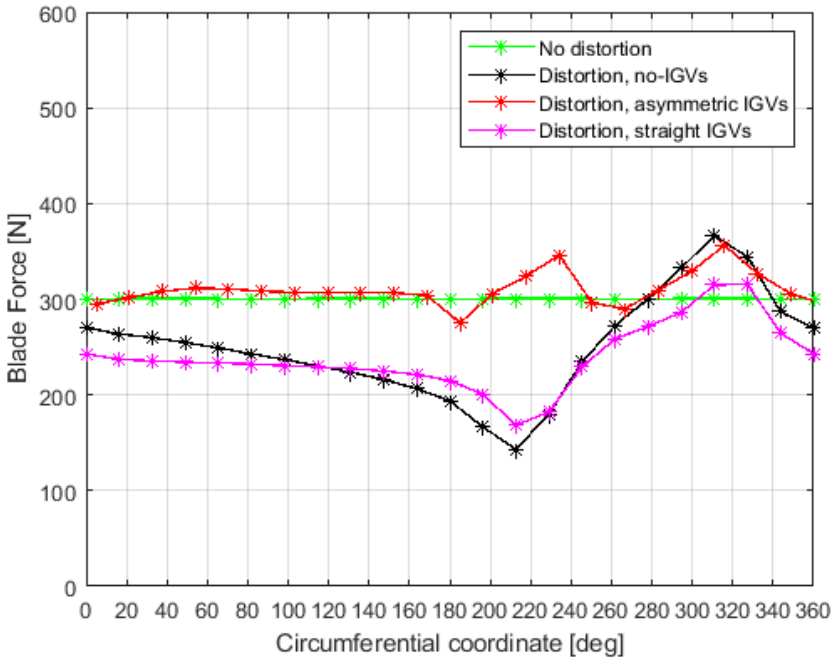

Figure C-10 Effect of IGVs on high-speed fan rotor aerodynamic blade force variation

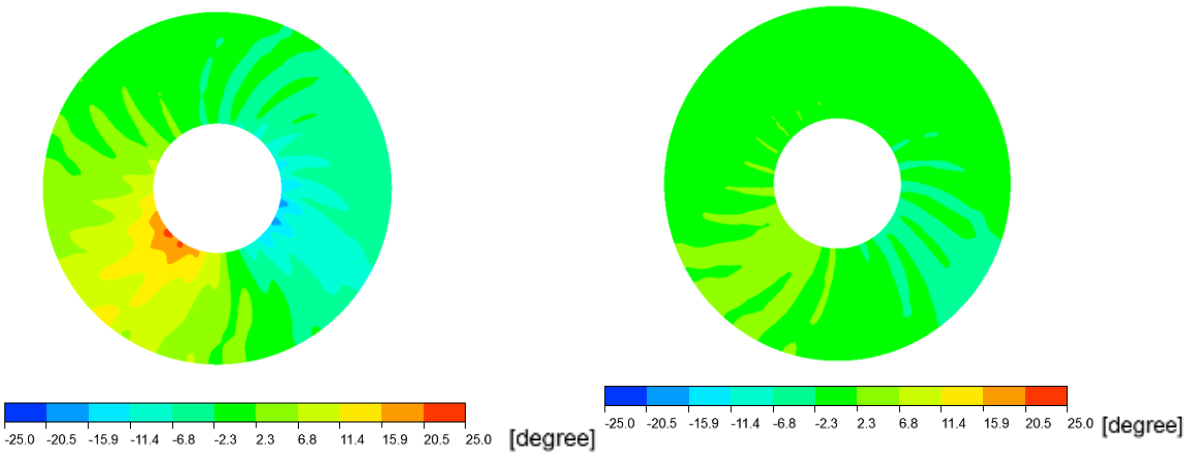

No-IGVs With straight IGVs

Figure C-11 Absolute whirl angle at high-speed rotor LE

APPENDIX D LOW-SPEED TEST FAN STAGE

D.1 ASYMMETRIC IGVS DESIGN ITERATIONS

Table D-1 lists the exit blade angles for the four asymmetric IGVs design iterations for the test fan stage. The blade circumferential coordinates represents the position of the blade in Figure 6.11, starting from the 3 o'clock position and going counterclockwise.

Table D-1 Asymmetric IGVs design iterations of the test fan stage

Circumferential	coordinates	0	25.71	51.43	77.14	102.9	128.6	154.3	180	192.9	205.7	218.6	231.4	244.3	257.1	270	282.9	295.7	308.6	321.6	334.3	347.1
Iteration 1	Exit angle [deg]	30	13	8	6	3	5	15	6	N/A	0	N/A	-20	N/A	-40	N/A	-40	N/A	0	N/A	9	N/A
Iteration 2	Exit angle [deg]	30	13	8	6	3	5	15	6	N/A	0	-10	-20	-30	-40	-40	-40	-20	0	N/A	9	N/A
Iteration 3	Exit angle [deg]	40	20	0	0	0	0	0	10	15	0	-10	-20	-30	-40	-40	-43	-40	-40	0	15	30
Iteration 4	Exit angle [deg]	10	5	5	5	5	5	25	40	N/A	-20	-40	-40	-40	-43	-40	-40	-30	-10	-10	0	15

D.2 TIME STEP STUDY

In Figure D-1 shows the result of the time step study for the test fan stage. It indicates that a setting of 20 time steps per rotor blade passing is adequate.

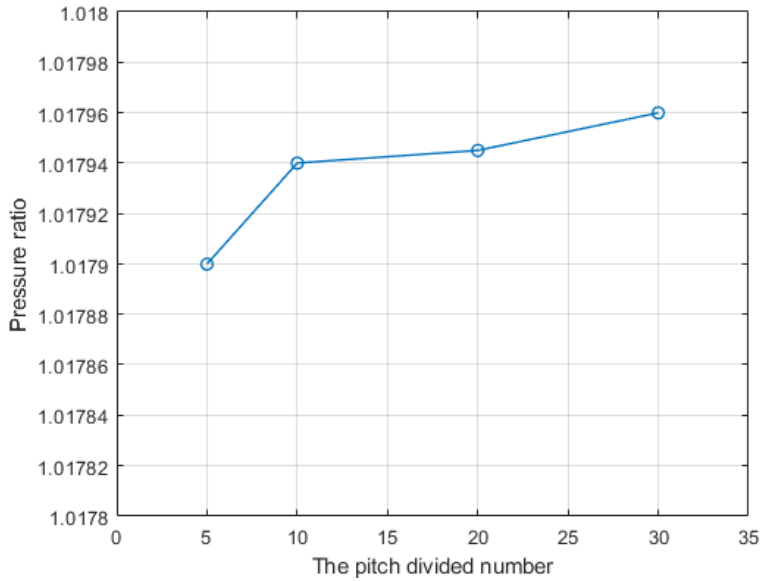

Figure D-1 Total pressure ratio versus number of time step per blade passing for test fan stage

D.3 CONTROL VOLUME ANALYSIS

This section presents the input and detailed output of the control volume analysis as detailed in appendix A (section A.2) for the test fan stage rotor. The black and red lines in the figures represent the fan parameters with straight IGVs and with asymmetric IGVs, respectively. The solid and dotted lines represent parameters at the rotor LE and rotor TE, respectively. Figures D-2 through D-5 show the input to the analysis, namely the circumferential distributions of static pressure, axial velocity, circumferential velocity and density at different span as extracted from the CFD predictions. In Figure D-3, on notices backflow between 280º to 340º at 20% span. Figures D-6 and D-7 plot the resulting axial and circumferential blade loading from the control volume analysis. Their combination according to equation (A.18) gives the total blade loading distributions in Figure 6.13.

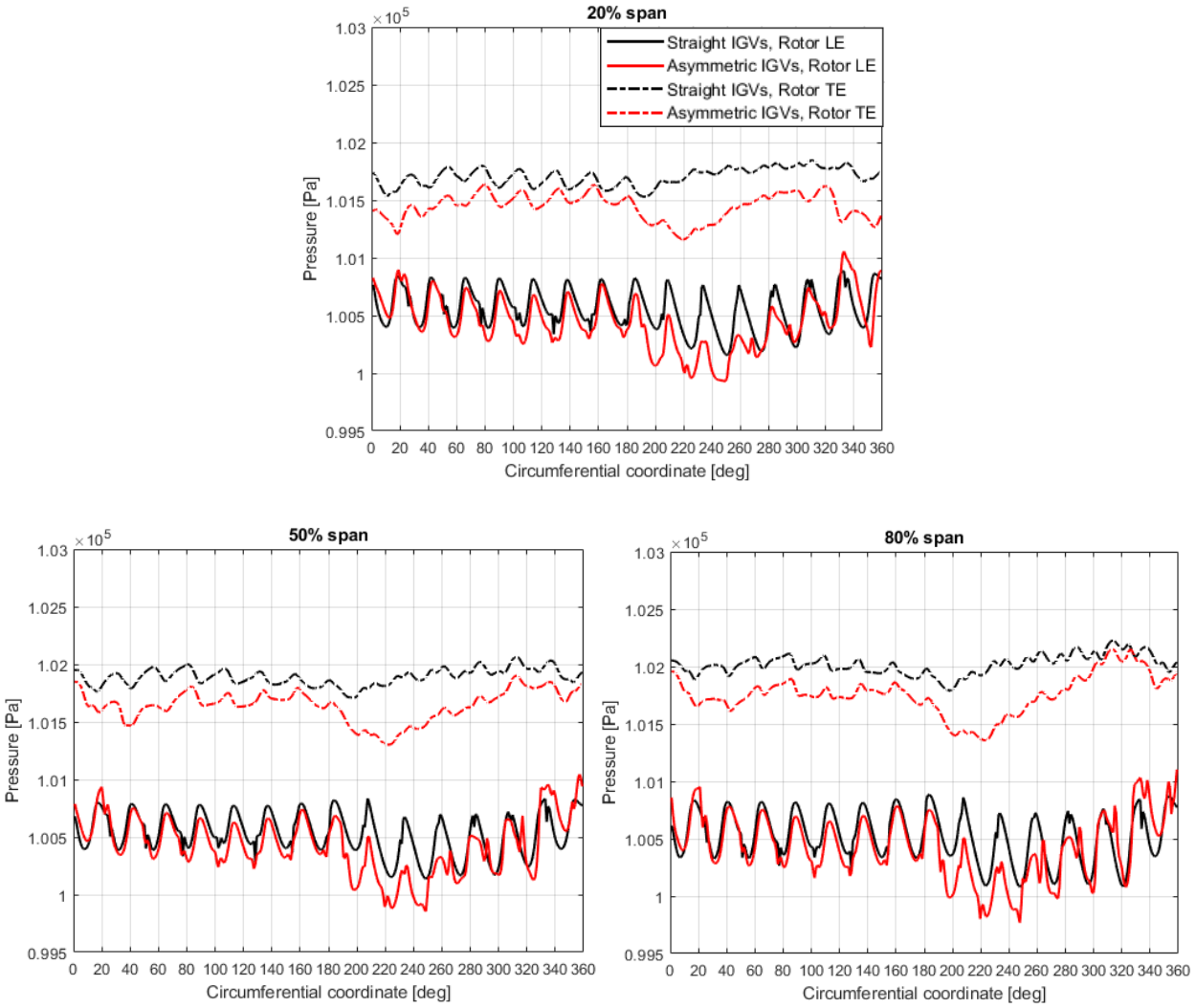

Figure D-2 Static pressure at rotor LE and TE for 20%, 50% and 80% spans

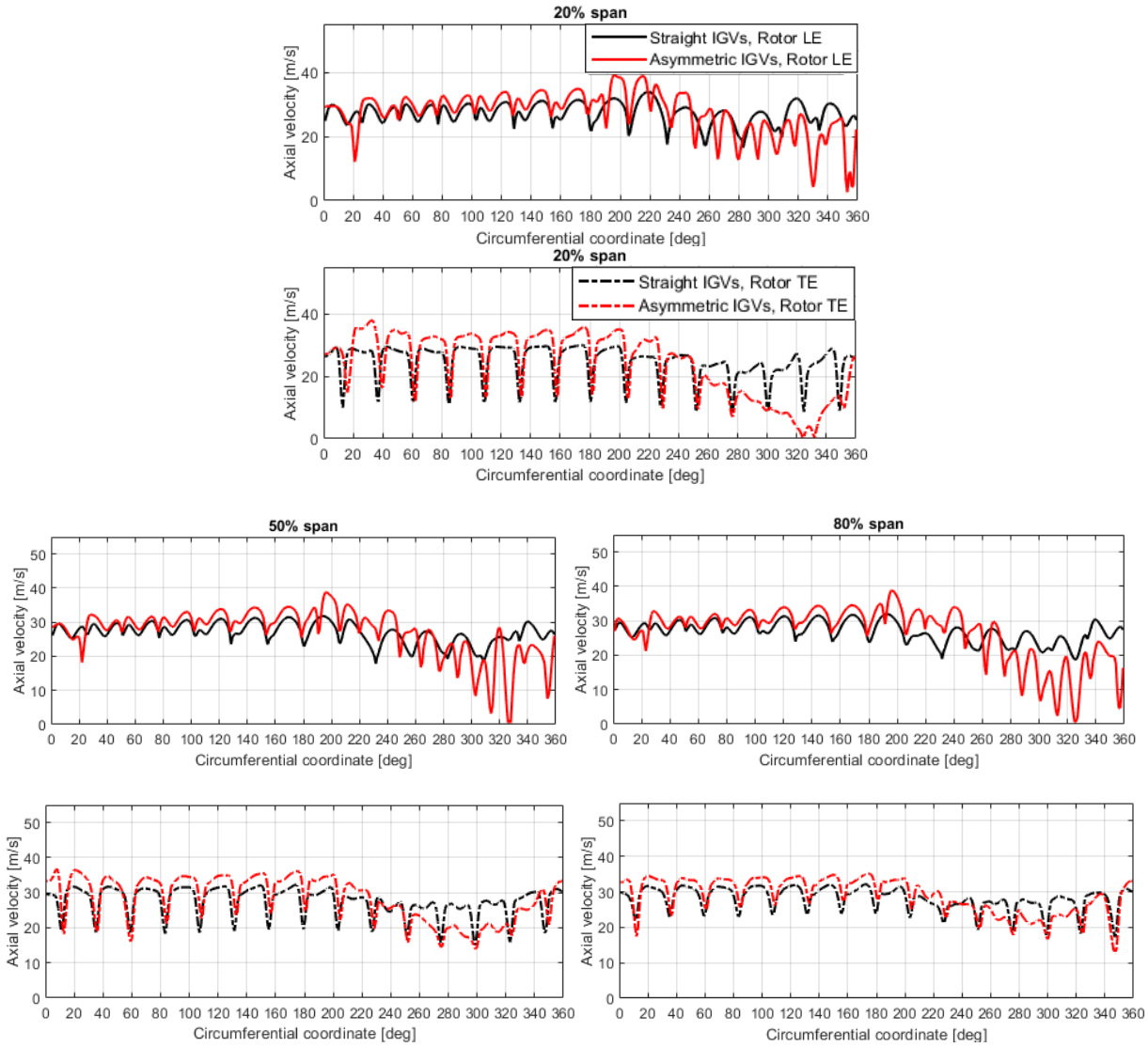

Figure D-3 Axial velocity at rotor LE and TE for 20%, 50% and 80% spans

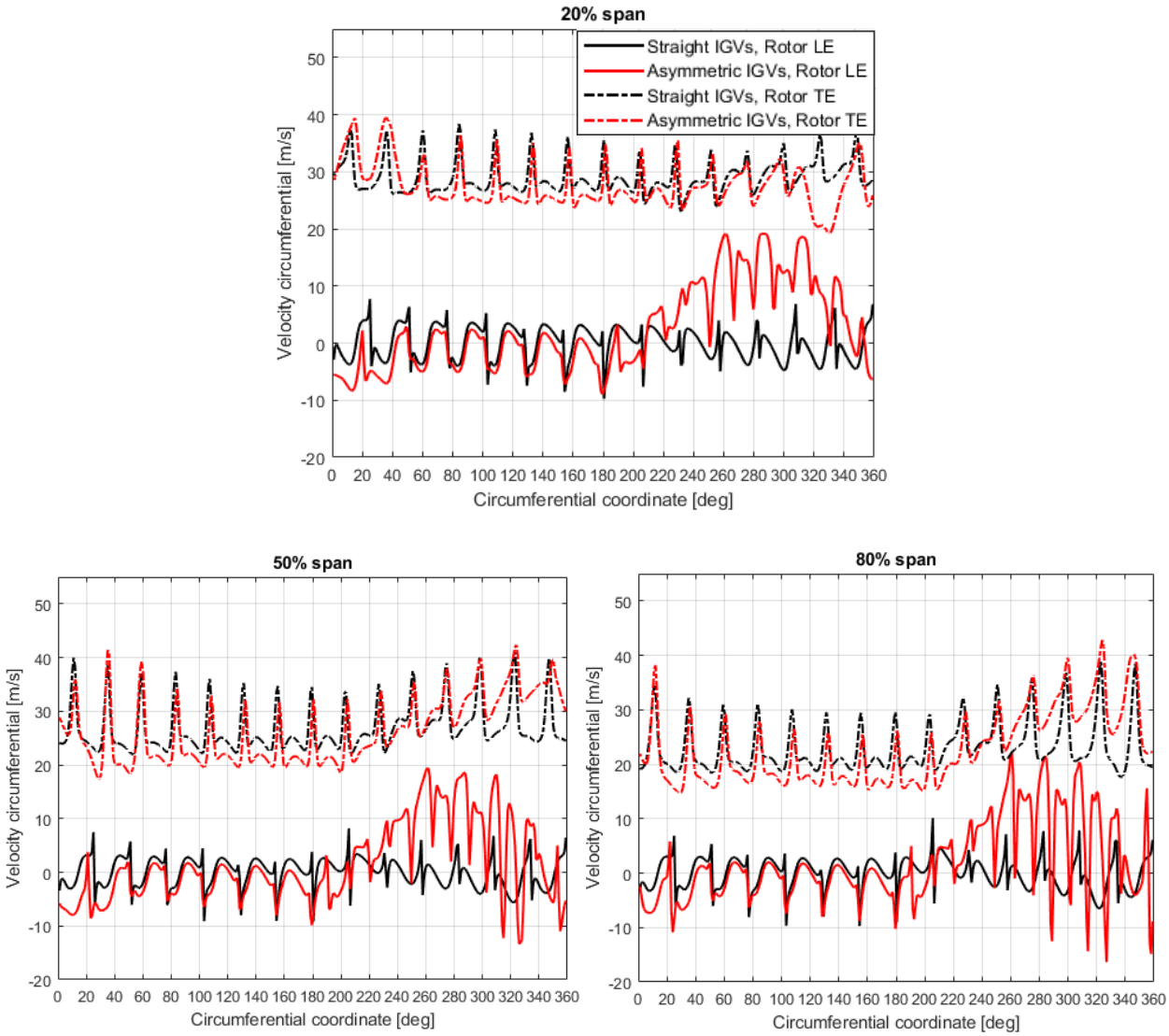

Figure D-4 Circumferential velocity in stationary frame at rotor LE and TE for 20%, 50% and 80% spans

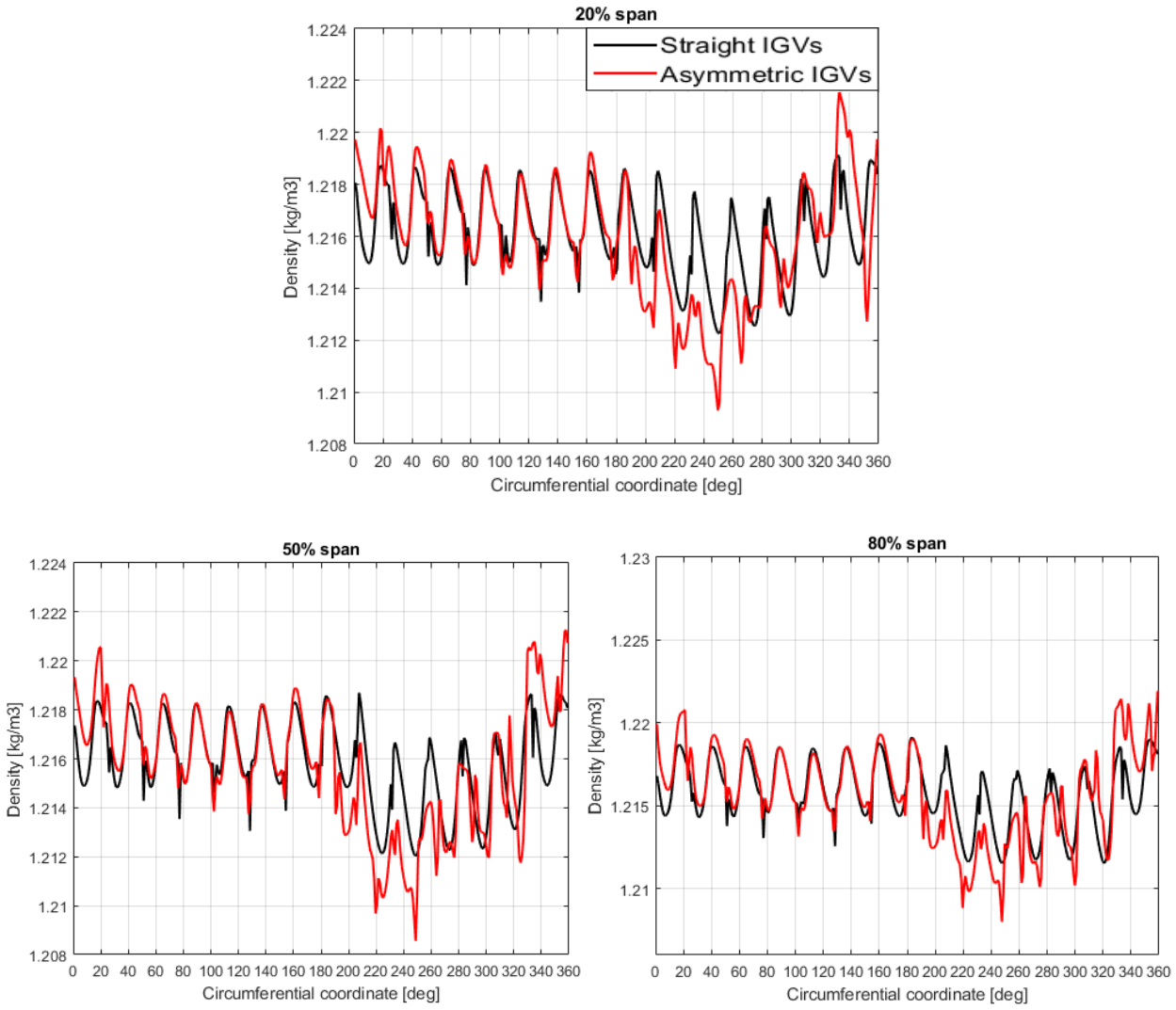

Figure D-5 Density at rotor LE for 20%, 50% and 80% spans

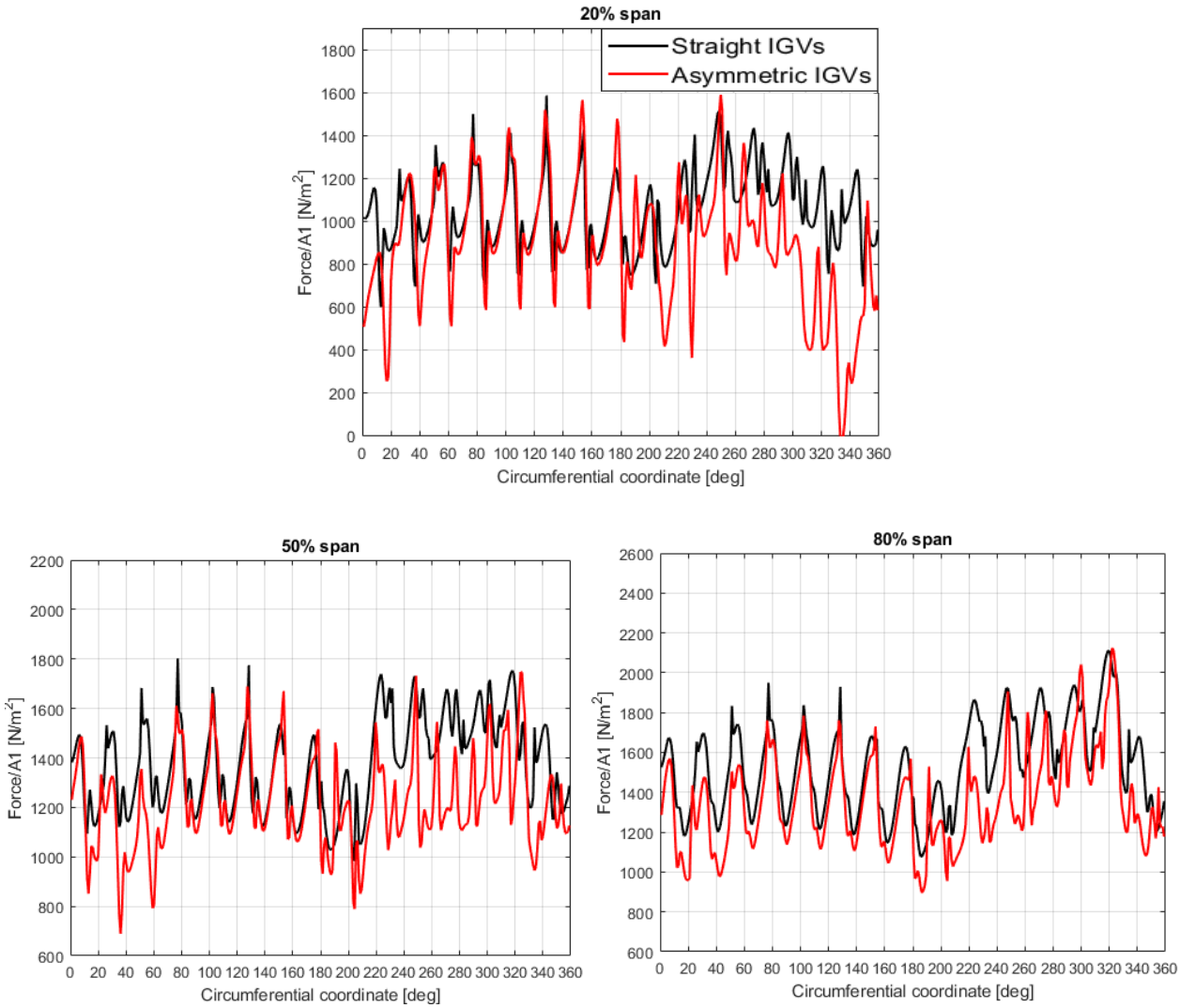

Figure D-6 Axial blade force per square meter in upstream direction at 20%, 50% and 80% spans

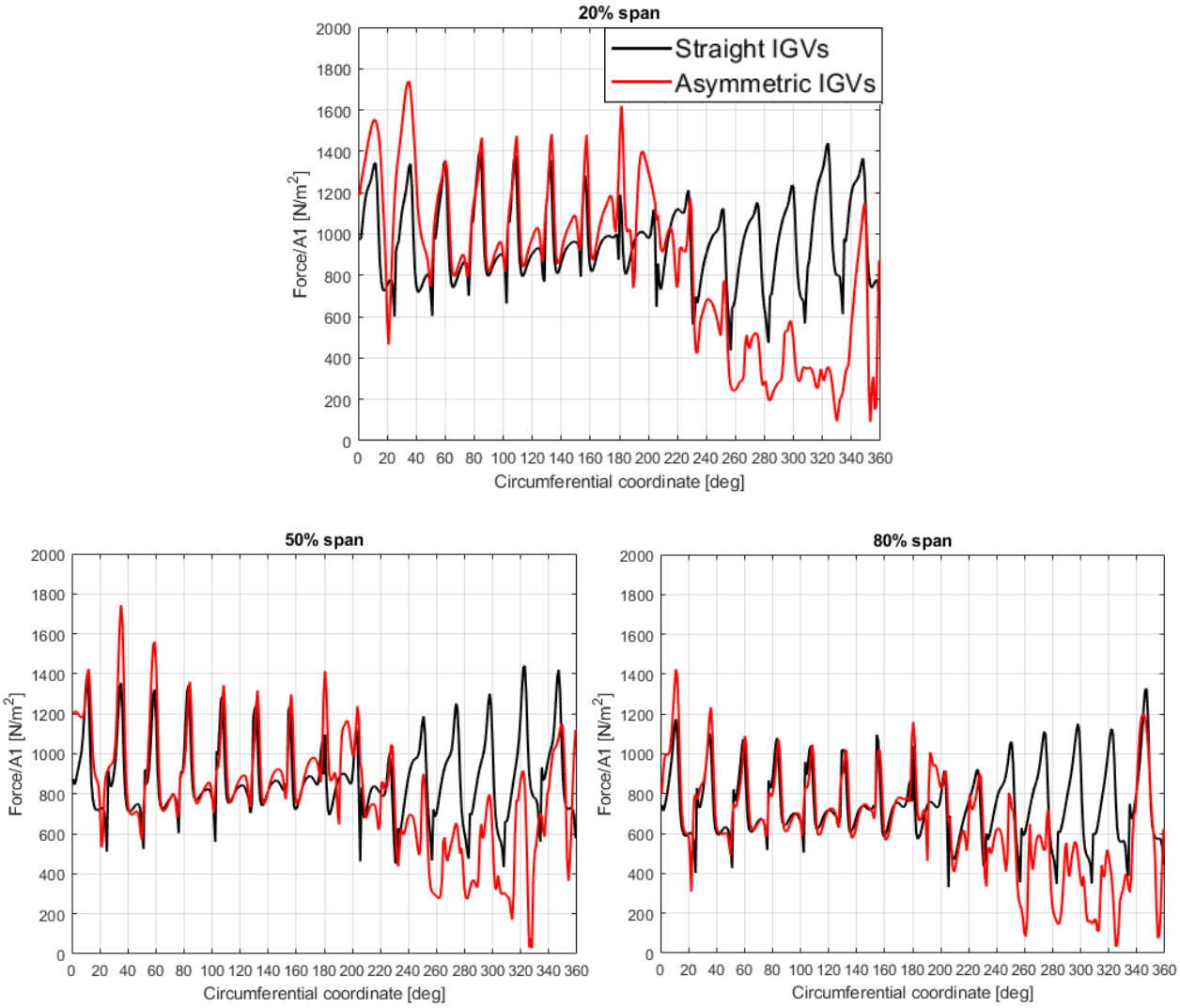

Figure D-7 Circumferential blade force per square meter opposite rotation direction at 20%, 50% and 80% spans